Dynamic Response Analysis of Wall Retaining Granular Fills with *PZT* Patches

A THESIS SUBMITTED IN THE FULFILMENT OF THE REQUIREMENT FOR THE AWARD

OF THE DEGREE OF

DOCTOR OF PHILOSOPHY

In

CIVIL ENGINEERING

By

NISHA KUMARI

Under the Supervision

of

Prof. A. Trivedi

Professor of Civil Engineering

Delhi Technological University, Delhi-110042

DEPARTMENT OF CIVIL ENGINEERING DELHI TECHNOLOGICAL UNIVERSITY

DELHI- 110042, INDIA

November 2023

Dedicated

To my Father,

Mother,

Brothers,

Teachers in my life

and Friends

For their support and guidance

DELHI TECHNOLOGICAL UNIVERSITY

(Formerly Delhi College of Engineering, Since 1941)

Shahbad Daulatpur, bawana road, Deelhi-110042

DECLARATION

I hearby declare that the research work presented in this thesis entitled "**Dynamic Response Analysis of Wall Retaining Granular Fills with *PZT* patches**" is original and carried out by me under the supervision of Prof. Ashutosh Trivedi, Professor, Department of Civil Engineering, Delhi Technological University, Delhi, and being submitted for the award of Ph.D. degree to Delhi Technological University, Delhi, India. The content of this thesis has not been submitted either in part or whole to any other university or institute for awarding any degree or diploma.

New Delhi

Nov, 2023

Nisha Kumari

Roll No. -2K16/PhD/CE/02

DELHI TECHNOLOGICAL UNIVERSITY

(Formerly Delhi College of Engineering, Since 1941)

Shahbad Daulatpur, bawana road, Deelhi-110042

CERTIFICATE

This is to certify that the thesis titled "**Dynamic Response Analysis of Wall Retaining Granular Fills with *PZT* patches**" which is being submitted by **Ms. Nisha Kumari** for the fulfilment of the requirements for the award of the degree of Doctor of Philosophy, is a record of the student's own work carried out at the **Delhi Technological University (DTU) Delhi** under my supervision and guidance. The matter embodied in this thesis has not been submitted elsewhere for the award of any other degree or diploma.

Prof. Ashutosh Trivedi,

Professor

Department of Civil Engineering

Delhi Technological University (DTU) Delhi

New Delhi

Nov, 2023

ACKNOWLEDGMENT

I would like to express deep sense of gratitude to several persons for their support in accomplishing the research work. It is a pleasant aspect that I have now the opportunity to express my gratitude to all of them.

Firstly, I would like to express my profound gratitude to my supervisor and motivator Prof. Ashutosh Trivedi, Civil Engineering Department, Delhi Technological University for his invaluable suggestions, co-operation and help in providing necessary facilities and resources during my research work. I thank him for encouraging me to stay in the laboratory and field for long hours. His wide knowledge and logical thinking have helped me complete my research work. He always made himself available for discussions despite his busy schedule and acquiring knowledge from his research expertise.

I express my gratitude to Prof. Narendra Dev and Prof. V. K. Minocha for their continued morale-boosting efforts and support towards completing my research work.

I am grateful to Delhi Technological University for providing the funding for instrumental conducting laboratory tests on the campus and help during the ex.

I express special thanks to Ma'am Mrs. Chhaya Trivedi for her support, care and encouragement throughout the research work. Also, my heartiest thanks go to my friend Prachi Lingwal whose proximity, love & affection made it possible to complete this research work. I would like to express my thanks to my colleagues, my juniors and all those who supported me directly or indirectly.

Lastly, I feel privileged and grateful to my parents, Mrs. Rajani Soni and Mr. Ashok Soni and my brothers Gourav Soni and Manish Soni, for everything in my life and the fact that I have reached here today. Everything I have achieved is because of their blessings, encouragement and support.

Above all, I wish to remember and pay my obeisance and reverence to "The Almighty" for his graciousness. Thanks for everything!

Nisha Kumari

Author

Abstract

This thesis focuses on the dynamic response analysis of confined granular fill with *PZT* (Lead Zirconate Titanate) patches embedded in various geo-structures. The geo-structures consist of machine foundations, pavement, subgrade, bridge abutment, railway track, retaining wall, and contact geo-material. These structures are subjected to ambient mechanical vibration due to dynamic loads. In this study, dynamic loading refers to the input excitations frequency on the confined granular fill with *PZT* patch. The dynamic response refers to stress and strain in the *PZT* patch and the wall retaining granular fill due to varied excitation frequencies. The voltage across the *PZT* patch is produced in response to the dynamic loading.

The electromechanical coupling of piezoelectric material is the key factor for the voltage and power output. The coupling techniques of structures and *PZT* patches are significantly affected by the variables namely fundamental frequency, contact pressure of loading, structure geometry, *PZT* patch placement, and contact material. The potential of power generation from the mechanical vibration of geo-structures has been classified for a range of power outputs. The coupling parameters improved the efficacy of power generation from the ambient vibration of geo-structures.

The study of charge density, voltage output, and power from the *PZT* patches is affected by alignment of *PZT* patches, thickness ratio, material properties of the confined granular fill and retaining structure. As a result the voltage output can be obtained directly from the stress-strain response, position of the *PZT* patch and the engineering properties of the confined granular fill.

The modulus ratio of the material, alignment of *PZT* patches, and gradation of infill material significantly affect the voltage generation. The maximum voltage output was obtained in the range of 0.001–0.5 V for the thickness ratio of 0.2–0.6 for the horizontally and vertically embedded *PZT*

patches. The observed voltage output is found appropriate for wide-ranging implements. A relationship between voltage and power output has been proposed for engineering applications. The power output may be up-scaled using multiple patches embedded throughout the confined granular fill and pavements subjected to continuous dynamic loads.

Experiments are carried out to capture the dynamic response of confined granular fill in terms of the voltage output from embedded *PZT* patches. The dynamic response of the system is analysed using the fast Fourier transformation (*FFT).* A digital static cone penetrometer (DSCP) test is conducted on a granular fill compacted at various excitation frequencies. The cone resistance of compacted granular fill indicates that voltage output (0.8-2.4 V) increased proportionally with varied excitation frequencies.

The damping loss factor and natural frequency are determined using the peak pick method. The depth of embedment, excitation frequency, location, and engineering properties of the confined granular fill influences the experimental voltage output from the *PZT* patch. The peak voltage output at the same embedment depth is observed at 10-50 Hz excitation frequencies in the vertical and transverse directions. The experimental observations show the output voltage in the range of 1.5-3.0 V in the vertical and transverse directions. The results show that the voltage and energy output gradually decay at higher frequencies for increasing the embedment depth of *PZT* patches.

The strain sensitivity of the *PZT* patch can be maximized at higher excitation frequencies and embedding the patch in a deeper granular fill. At deeper depths for various excitation frequencies, the energy output is obtained in the range of 0.10-1.78 nJ, and power output is obtained in the range of 0.5-14 watts.

Thus, the mechanical vibration of the structures can be utilized for power generation using the electromechanical conversion characteristics of the piezoelectric material. This research can lead to

an increase in the energy output and can thus improve the overall efficiency of the *PZT* patch embedded in confined granular fills. The findings of this research contribute to advancing the knowledge and understanding of dynamic response analysis in confined granular fill with *PZT* patches. The results offer valuable insights into the behavior of *PZT* patches under different excitation frequencies, facilitating the design and optimization of these systems in a wide range of geo-structures. Future research can build upon these findings to further refine the dynamic response analysis techniques and enhance the performance of *PZT* patches in various applications.

TABLE OF CONTENTS

DECLARATION ***ii***

CERTIFICATE ***iii***

ACKNOWLEDGMENT ***iv***

ABSTRACT ***v***

LIST OF FIGURES ***xii***

LIST OF TABLES ***xvi***

LIST OF SYMBOLS ***xvii***

CHAPTER :

1 Introduction 1

1.1 General Introduction 1

1.2 Dynamic Response of Walls Retaining Granular Fill 2

1.3 Mathematical Description for Stress-Strain and Voltage Output of *PZT* Patch 3

1.4 Dynamic Response of *PZT* Patch 4

1.5 Gaps in Literature 7

1.6 Scope and Objectives of the Research 7

1.7 Publications Based on the Present Work 8

1.8 Structure and Organization of the Thesis 9

1.9 Benefits to Practitioners, Researchers and Industry 9

2 Literature Review 11

2.1 Introduction 11

2.2 Structural Elements and Modelling 15

2.3 Numerical Techniques 20

2.3.1 Piezoelectric Finite Element Method 20

2.3.2 Dynamic Stiffness Method 22

2.4 Power Generation from Mechanical Vibration 23

2.4.1 Mechanical Vibration of Pavement and Subgrade 23

2.4.2 Mechanical Vibration of Railway Tracks, Bridges, and Retaining Structures 27

2.5 Composition of *PZT* and Construction Material 30

3 Semi-active Strategy for Strain Response of Wall Retaining Granular Fill 33

3.1 Introduction 33

3.2 Semi-active Method 34

3.3 Stress-strain in *PZT* Patches 35

3.3.1 Stress-strain in Horizontal *PZT* Patch for Vertical Dynamic Loading 35

3.3.2 Stress-strain in Wall Retaining Granular Fill for Vertical Dynamic Loading 37

3.3.3 Stress-strain in Vertical *PZT* Patch for Horizontal Vibrations 38

3.4 Dynamic Response of Horizontal and Vertical Vibration using *PZT* Patches 40

3.5 Soil- wall System with *PZT* Patches 41

3.6 Dynamic Response of the Soil-wall System 42

3.6.1 Horizontal Displacement 42

3.6.2 Vertical Displacement 43

4 Factors Influencing Piezoelectric Response of Embedded *PZT* Patch 44

4.1 Introduction 44

4.2 Engineering Properties of *PZT* Patches 46

4.3 Stress-strain Behaviour of *PZT* Patches 47

4.4 Evaluation of Charge Density 49

4.4.1 Horizontally and Vertically Embedded *PZT* Patch 49

4.5 Charge Density for Vertically Embedded *PZT* Patch 51

4.6 Voltage Output from Horizontally and Vertically Embedded *PZT* Patch 53

4.7 Discussion on Factors Influencing Piezoelectric Response of Embedded *PZT* Patch 54

4.7.1 Effect of Stiffness of Confined Granular Fill and *PZT* Patches 55

4.7.2 Charge Density on Hard, Semi-hard, and Soft *PZT* Patches 57

4.7.3 Comparative Analysis of Voltage Output 64

4.7.4 Effect of External Resistance on Power Output of the *PZT* Patch 67

5 Effect of Confined Granular Fill on Efficiency of *PZT* Patches 70

5.1 Introduction 70

5.2 Properties of Granular Fill and *PZT* Patches 71

5.3 Experimental Set-up for Voltage Output from *PZT* Patches 73

5.3.1 Model Set-up 73

5.3.2 Electrodynamic Exciter and Instrumentation 75

5.3.3 Digital Static Cone Penetrometer (DSCP) 75

5.3.4 Model Parameter Estimation 77

5.4 Discussion on DSCP Results and Voltage Output of *PZT* Patches Using *FFT* 78

5.4.1 Natural Frequency Analysis 78

5.4.2 Cone Resistance of Confined Granular Fill 80

5.4.3 Analysis of Output Voltage 82

6 Investigation of Strain Sensitivity and Energy Output of *PZT* Patches 86

6.1 Introduction 86

6.2 Material Properties 87

6.3 Experimental Set-up 87

6.4 Result and Discussion 88

6.4.1 Effect of Excitation Frequency on Strain Sensitivity 88

6.4.2 Effect of Embeddment Depth on Strain Sensitivity 89

6.4.3 Effect of Excitation Frequency on Power and Energy Output 91

6.4.4 Effect of Embedment Depth on Power and Energy Output 92

7 Conclusions and Future Recommendations 97

7.1 Conclusions 97

7.2 Future Recommendations 100

References 103

List of Figures

Fig. 1.1 Piezoelectric d-33 model 5

Fig.1.2 Piezoelectric d-31 model 5

Fig. 2.1 Piezoelectric applications in structures utilizing mechanical vibrations 12

Fig. 2.2 Flow chart for power generation from mechanical vibration of the geo-structure 14

Fig. 2.3 The piezoelectric elemental structures (a) Unimorph piezoelectric cantilever beam (b) Bimorph piezoelectric cantilever beam with tip mass (c) The design of cymbal transducer made of PZT material (d) The geometry of piezoelectric stack for structure. 19

Fig. 3.1 Flow chart of semi-active control of dynamically loaded retaining granular fill 34

Fig. 3.2 The average strain in the *PZT* layer at various thickness ratios 36

Fig. 3.3 The average stress in the *PZT* layer at various thickness ratios 36

Fig. 3.4 The average strain in wall retaining granular fill at various thickness ratios 37

Fig. 3.5 The average stress in wall retaining granular fill at various thickness ratios 37

Fig. 3.6 Variation of average strain with modulus ratio (n) in *PZT* layer for horizontal dynamic loading 40

Fig. 3.7 Variation of average strain with modulus ratio (n) for backfill layer for horizontal dynamic loading 40

Fig. 3.8 Displacement profile represented in the form of the spring-mass system 42

Fig. 4.1 Flow chart for electromechanical energy output from mechanical vibrations 45

Fig. 4.2 Flow chart for the generation of electric charge due to mechanical vibrations 46

Fig. 4.3 Stress variation with modulus ratio for horizontally embedded *PZT* patch 56

Fig. 4.4 Stress variation with modulus ratio for vertically embedded *PZT* patch 56

Fig. 4.5 Charge density computed for retaining structure of the top surface of the horizontally and vertically embedded hard *PZT* patch in the confined granular fill 58

Fig. 4.6 Charge density computed for retaining structure of unit width, piezoelectric strain, modulus ratio, and thickness ratio on the bottom surface of the horizontally and vertically embedded hard *PZT* patch in the confined granular fill 59

Fig. 4.7 Charge density computed for retaining structure of unit width, piezoelectric strain, modulus ratio and thickness ratio on the top surface of the horizontally embedded and from vertically embedded hard *PZT* patch in the confined granular fill 59

Fig. 4.8 Charge density computed for retaining structure of unit width, piezoelectric strain, modulus ratio, and thickness ratio on the bottom surface of the horizontally and vertically embedded hard *PZT* patch in the confined granular fill 60

Fig. 4.9 Charge density computed for retaining structure of unit width, piezoelectric strain, modulus ratio, and thickness ratio on the top surface of the horizontally and vertically embedded soft *PZT* patch in the confined granular fill 60

Fig. 4.10 Charge density computed for retaining structure of unit width, piezoelectric strain, modulus ratio, and thickness ratio on the bottom surface of the horizontally and vertically embedded soft *PZT* patch in the confined granular fill 61

Fig. 4.11 Charge density computed for retaining structure of unit width, piezoelectric strain, modulus ratio, and thickness ratio on the top surface of the horizontally and vertically embedded soft *PZT* patch in the confined granular fill 61

Fig. 4.12 Charge density computed for retaining structure of unit width, piezoelectric strain, modulus ratio, and thickness ratio on the bottom surface of the horizontally and vertically embedded soft *PZT* patch in the confined granular fill 62

Fig. 4.13 Charge density computed for retaining structure of unit width, piezoelectric strain, modulus ratio, and thickness ratio on the top surface of the horizontally and vertically embedded semi-hard *PZT* patch in the confined granular fill 62

Fig. 4.14 Charge density computed for retaining structure of unit width, piezoelectric strain, modulus ratio, and thickness ratio on the top surface of the horizontally and vertically embedded semi-hard *PZT* patch in the confined granular fill 63

Fig. 4.15 Charge density computed for retaining structure of unit width, piezoelectric strain, modulus ratio, and thickness ratio on the top surface of the horizontally and vertically embedded semi-hard *PZT* patch in the confined granular fill 63

Fig. 4.16 Charge density computed for retaining structure of unit width, piezoelectric strain, modulus ratio, and thickness ratio on the bottom surface of the horizontally and vertically embedded semi-hard *PZT* patch in the confined granular fill 64

Fig. 4.17 Voltage output computed for the retaining structure, piezoelectric strain constant, polarization ratio (0.112, 0.087 and 0.114) and thickness ratio of horizontally embedded hard, semi-hard and soft *PZT* patch in the confined granular fill 66

Fig. 4.18 Voltage output computed for the retaining structure, piezoelectric strain constant, polarization ratio (0.112, 0.087 and 0.114) and thickness ratio of vertically embedded hard, semi-hard and soft *PZT* patch in the confined granular fill 66

Fig. 4.19 The output voltage for different external resistance for high, medium and low resistance applications 68

Fig. 4.20 Power output for different external resistance for high, medium and low resistance applications 68

Fig. 5.1 Particle size distribution of granular material used in the present study 71

Fig. 5.2 Laboratory experimental set-up for dynamic response and voltage measurement 74

Fig. 5.3 (a) Layout of the *PZT* patch embedded into the confined granular fill for the vertical and transverse vibrations (b) The optical image of the embedded *PZT* patches in pavement 74

Fig. 5.4 Layout of the test section measurement and testing location of the DSCP test 77

Fig. 5.5 Influence of depth of granular fill (20-40cm) on the displacement spectrum at an excitation frequency of (A) 10Hz (B) 20Hz (C) 30Hz (D) 40Hz (E) 50Hz 80

Fig. 5.6 Cone resistance obtained from digital SCP data for confined granular fill with and without excitation frequency of (A) 10-30 Hz (B) 40-50 Hz 82

Fig. 5.7 Output voltage for *PZT* patches embedded at varying depths in the vertical direction 84

Fig. 5.8 Output voltage for *PZT* patches embedded at varying depths in the transverse direction .. 85

Fig. 6.1 The strain in embedded *PZT* patch at varied excitation frequencies with different depth ratios (h_r)..... 88

Fig. 6.2 The strain with depth ratio at excitation frequencies ranging from 10 to 30 Hz 90

Fig. 6.3 The strain with depth ratio at excitation frequencies ranging from 50 to 80 Hz 90

Fig. 6.4 The power output from *PZT* patch at varied excitation frequencies with different depth ratios (h_r)..... 91

Fig. 6.5 The energy output from *PZT* patch at varied excitation frequencies with different depth ratios 92

Fig. 6.6 The energy output variation with depth ratio at excitation frequency ranging from 10 to 30 Hz..... 93

Fig. 6.7 The energy output with depth ratio at excitation frequencies ranging from 50 to 80 Hz ... 94

Fig. 6.8 The power output with depth ratio at excitation frequencies ranging from 10 to 30 Hz 94

Fig. 6.9 The power output with depth ratio at excitation frequencies ranging from 50 to 80 Hz 95

List of Tables

Table 1.1 Material properties and chemical formula of *PZT* patch 5

Table 2.1 Comparison of output potential difference as per harvesting technologies for substructures 24

Table 2.2 The analytical techniques for the conversion of mechanical vibrations to electrical energy from structures namely pavements, subgrade, and retaining structures 25

Table 2.3 Analytical techniques used for power generation applicable to geo-structures..... 28

Table 2.4 The power output from mechanical vibrations of traffic loads 29

Table 2.5 Composites of *PZT* and construction material for power generation 31

Table 4.1 Engineering properties of piezoelectric patches 47

Table 4.2 Charge density for confined granular fill with *PZT* patches..... 57

Table 4.3 Voltage output for various *PZT* patches 65

Table 4.4 Classification of *PZT* applications for output voltage and resistance..... 69

Table 5.1 Index properties of the confined granular materials 71

Table 5.2 Properties of the *PZT* patch 72

Table 5.3 Damping loss factor and natural frequency of the confined granular fill 80

Table 5.4 Fitting parameters α and β for the confined granular fill at varying excitation frequency 81

Table 5.5 Voltage output efficiency of *PZT*-patch embedded in poorly graded soil for various excitation frequencies 83

Table 6.1 Fitting parameters α, β and γ for strain, energy and power output at varying depth ratios. 96

List of symbols

Symbol	Description
$\tilde{K}$	added stiffness induced by the applied preloading conditions
$\dot{q}(t)$	the current output of piezoelectric materials
Θ	electromechanical coupling matrix
D	hysteretic damping ratio
C	coefficient of viscous damping
EI	flexural stiffness of the beam
$w(x, t)$	transverse deflection of the pavement
$\overline{w}(\overline{x},t)$	transverse deflection of the bridge
m_a, m_b	masses of asphalt mixtures
δ	Dirac delta function
t_d	time required to load pass the bridge
k_2	elastic coefficient of the stack
C_2	equivalent capacitance of the stack
N_s	electromechanical conversion coefficient of the stack
$y(x,t)$	displacement of the bridge at position x and time t
n	the ratio of modulus *PZT* over modulus backfill
μ	the ratio of thickness *PZT* over thickness backfill
a	the ratio of thickness retaining wall over thickness *PZT*
b	the ratio of modulus retaining wall over modulus *PZT*

Symbol	Description
u_x	horizontal displacement of retaining wall-*PZT* system
u_z	vertical displacement of retaining wall-*PZT* system
$w_{rel}(x,t)$	transverse displacement of the beam
$w_b(x,t)$	transverse displacement of the base
C_a	viscous air-damping
$V(t)$	steady-state voltage
R	external resistance
C_c	the capacitance of the piezoelectric material
ϑ	coefficient of background coupling terms
K_s	stiffness of compression spring
nd_{33}	the effective piezoelectric constant of the stack
nk_{33}^{σ}	the effective dielectric constant of the stack
E_z	electric field
ε_i	the linear strain of deformation
k_i^o	the curvature of the plate at the midplane
$\hat{z}$	thickness matrix
B_u	strain-displacement matrix
N_u	displacement shape function
u^e	discrete element nodal displacement vector
P_3	piezoelectric polarization in 3-D

Symbol	Description
T_i	stress tensor
g_{3i}	piezoelectric voltage constant of *PZT*
ε_{33}^{T}	relative dielectric constant in 3-D
U_E	harvested electric energy from a *PZT* disk
I	the second moment of the area around the neutral axis
C_a	viscous damping coefficient
D	dynamic stiffness matrix
C_p	cost of *PZT* per unit
C_i	cost installation of *PZT* per unit
w_p	energy generated from each *PZT* per vehicle
N	number of vehicles passing per day
Y	the service life of the *PZT*
FEA	finite element analysis
PZT	Lead Zirconate Titanate
ε_{HE}	strain in horizontally embedded PZT patch
σ_{PZT}	the stress in the PZT patch
σ_{HE}	stress in horizontally embedded PZT patch
ε_{VE}	strain in vertically embedded PZT patch
σ_{VE}	stress in vertically embedded PZT patch

Symbol	Description
ρ_{Top} , ρ_{Bottom}	charge density at the top and bottom surface of the PZT patch, respectively.
ρ_{THE} , ρ_{BHE}	charge density at the top and bottom surface of the horizontally embedded PZT patch, respectively.
Q_{Top} , Q_{Bottom}	charge quantity at the top and bottom surface of the PZT patch, respectively.
Q_{THE} , Q_{BHE}	charge quantity at the top and bottom surface of the horizontally embedded PZT patch, respectively.
ρ_{TVE} , ρ_{BVE}	charge density function at the top and bottom surface of the vertically embedded PZT patch, respectively.
Q_{TVE} , Q_{BVE}	charge quantity at the top and bottom surface of the vertically embedded PZT patch, respectively
h_w	thickness of the wall
μ	thickness ratio of PZT patch and backfill
a	thickness ratio of the retaining wall and PZT patch
b	modulus ratio of retaining wall and PZT patch)
D_3	electric displacement
$\frac{\varepsilon_{33}^T}{\varepsilon_o}$	relative permittivity
ε_0	absolute permittivity of the vacuum
ε_{33}^T	permittivity of the material in direction-33 under constant stress
$\varepsilon_{33}^{T=0}$	free permittivity of the material in direction-33 under no stress
d_{31}	Piezoelectric strain constant in the mode 31

Symbol	Description
d_{33}	piezoelectric strain constant in the mode 33
d	depth of embedment of PZT patch
z	thickness direction coordinate from the neutral plane
e	distance between the neutral axis and lower surface of the PZT patch
E	equivalent electric field intensity
K	constant of proportionality
VE	subscript for vertically embedded patch
HE	subscript for horizontally embedded patch
E_P	modulus of the PZT patch
E_W	modulus of the retaining wall
H	height of the retaining structure
L	length of the retaining structure
h_P	thickness of the PZT patch
h_R	thickness of the granular backfill
n	modulus ratio of PZT patch and backfill
V_{HE}	voltage output for horizontally embedded PZT patch
V_{VE}	voltage output for vertically embedded PZT patch
PEH	piezoelectric energy harvesters

Chapter 1

Introduction

This chapter explains the objectives of this research and includes the need for a sustainable solution to the problem considered in this thesis. This is followed by the scope and an explanation of how this thesis has been structured for easy understanding and convenience of the reader.

1.1 General Introduction

The wall retaining granular fills are a foundation substructure and geo-structures for offshore platforms, high-rise buildings, bridges, railway embankments, and traffic embankment structures. These complex structures experience axial, lateral, and torsional vibrations. Conventionally, the retaining walls are analyzed for displacement due to axial and lateral loads. These structures are often subjected to vibrations due to dynamic loads. Their displacement sensitivity to dynamic loads may be captured using *PZT* sensors.

The dynamic response of walls retaining granular fill is essential to analyze the displacement produced due to induced vibrations. The determination of acceleration, natural frequency, and energy plays a vital role in analyzing the dynamic response of wall retaining granular fill. Several researchers (Bathurst et al., 1998, Jamshidi et al., 2010, Xiao et al., 2021) have developed various methods to determine the acceleration and frequency of dynamically loaded confined granular fill. The conversion of the vibrational response of wall retaining granular fill to electrical energy can be one of the utilitarian outputs from existing geostructures. It can be achieved without impacting the operational performance of the retained granular fill. Hence, analysis of the dynamic response of wall retaining granular fill and conversion of mechanical vibration to electrical energy using piezoelectric material is an important milestone for energy harvesting from geostructures. The present study focuses to investigate the response of wall

retaining granular fill and to capture the energy transmittance due to dynamic loads on confined granular fill using *PZT* patches. This mechanical energy can be converted into electrical energy. The basic transduction mechanisms for energy conversion using piezoelectric implements are considered in the following sections.

1.2 Dynamic Response of Walls Retaining Granular Fill

The purpose of the dynamic response analysis is designing structural and mechanical systems to function accurately. Additionaly, effectively optimize system parameters such as geometry, material properties, and damping mechanisms to minimize energy losses.

The current understanding of the dynamic response of walls retaining granular fill has come from model tests and numerical analysis. The dynamic response depends on the wall movements and pressure of the soil. Most model tests and analyses have involved gravity walls with translation and rotation. The mode of wall movements influences the magnitude and distribution of dynamic wall pressures. Thus, for dynamic response analysis of retaining walls various assumptions about structure, input motion and soil were used.

In the present study, *PZT* patches are used to determine the dynamic response of the wall retaining granular fill theoretically and experimentally. According to the piezoelectric effect, the dynamic load will charge the strain in the *PZT* patch and generate charge density on the surface of the *PZT* patch. An attempt has been made to interpret this charge or voltage data in acceleration, strain, and displacement without digitally or electrically separating or integrating the signal. An effort has been undertaken to record the voltage output associated with different frequencies and the cone resistance. As a result, the *PZT* patch data has been used in dynamic response analysis, and the interpreted data can also be used in energy harvesting from mechanical vibrations.

In this approach, the following steps are involved;

(a) Identify the various vibration modes from the frequency response of the system. The amplitude varies with the excitation frequency of dynamic loads due to moving vehicles. Therefore, we have monitored these modes for various load intensities using the frequency response. After identifying the modes, the modal parameters such as displacement amplitude, damping, and frequency are monitored.

(b) For various excitation frequencies, the most influential strain is normal strains identified for monitoring purposes. Therefore directional *PZT* patches are correlated to observe strains. For this purpose, *PZT* thin film can be embedded at various depths into a confined granular fill.

(c) The thin *PZT* patch may be correlated to output engineering parameters (acceleration and displacement) so that the measured voltage output can be interpreted for dynamic response analysis. It is potentially beneficial for energy harvesting and structural health monitoring.

(d) Dynamic parameters such as frequency, amplitude, and damping can be obtained from the measured dynamic strain using an *FFT* (Fast Fourier Transformation) analyzer.

1.3 Mathematical Description for Stress-Strain and Voltage Output of *PZT* Patch

When piezoelectric materials are subjected to mechanical stress, electrical energy generated in proportion to that stress is known as the direct piezoelectric effect. The direct effect occurs through the compression of piezoelectric material. Piezoelectricity is the term used to describe the intertwined relationship between electric and elastic mechanical behavior exhibited by specific materials. The linear electrical behaviour of the *PZT* material is expressed as,

$$D_i = \varepsilon_{ij} E_j \qquad (1.1)$$

Hooke's law for elastic materials is expressed as,

$$S_{ij} = s_{ijkl} T_{kl} \qquad (1.2)$$

where, *D* electric charge density displacement. ε is electric permittivity. *E* is the electric field. *T* is the stress component. *S* is strain componentss is compliance coefficient. *s* is compliance coefficient. These relations can be combined into the coupled equation, expressed as the following constitutive piezoelectric equations in the function of various piezoelectric coefficients. The piezoelectric energy is captured as charge density and voltage generation on the surface of *PZT* patches due to mechanical vibrations. The relation between strain-charge (*S*-*D*), stress-charge (*T*-*D*), strain-voltage (*S*-*E*) and stress-voltage (*T*-*E*) is expressed as the following relations,

$$S = s_E.T + d^t.E \quad (1.3)$$

$$D = d.T + \varepsilon_T.E \quad (1.4)$$

$$T = c_E.S - e^t.E \quad (1.5)$$

$$D = e.S + \varepsilon_s.E \quad (1.6)$$

$$S = s_D.T + g^t.D \quad (1.7)$$

$$E = -g.T + \varepsilon_T^{-1}.D \quad (1.8)$$

$$T = c_D.S - q^t.D \quad (1.9)$$

$$E = -q.S + \varepsilon_s^{-1}.D \quad (1.10)$$

Where, *c* is stiffness coefficient. ε is electric permittivity. *d* is piezoelectric coupling coefficient for strain change form. *e* is piezoelectric coupling coefficient for stress change form. *g* is the piezoelectric coefficient for strain-voltage, and *q* is piezoelectric coupling coefficient for stress voltage.

1.4 Dynamic Response of *PZT* Patch

The word 'piezo' means pressure, while 'electric' refers to electricity. An electric field is generated when a piezoelectric material is stressed. Piezoelectric materials can produce electric

voltage when deformed due to vibrations (direct effect), and on the other hand, they deform when subjected to an externally applied electric voltage (converse effect).

Table 1.1 Material properties and chemical formula of *PZT* patch

PZT description	Chemical formula	Material properties
Lead Zirconate Titanate	$P_b[Zr_\xi Ti_{(\xi-1)}]O_3 : 0 \leq \xi \leq 1$	Density (7600-7800 kg/m^3) Elastic stiffness coefficient (1.0-1.1x10^{11}N/m^2) Extremely high mechanical quality factor, good temperature and time consistency, suitable for high power acoustic applications and resonance mode

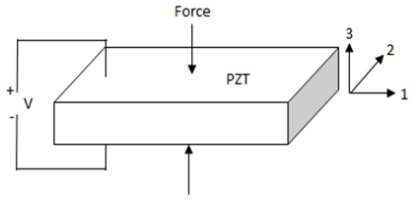

Fig. 1.1 Piezoelectric d-33 model

The energy harvesting mechanism is the direct piezoelectric effect that allows the material to absorb mechanical vibration energy from its host structure or surroundings and convert it into electrical energy, thus forming the basis of the field of vibration-based piezoelectric energy harvesting.

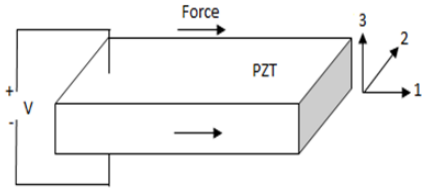

Fig.1.2 Piezoelectric d-31 model

The capability of piezoelectric material to transform mechanical energy into electrical energy also depends on the piezoelectric coupling mode used in the energy harvesting system. Two

practical piezoelectric coupling modes of operation exist, the −31 mode and the −33 mode, as shown in Fig. 1.1 and 1.2. In the −31 mode, force is applied perpendicular to the poling direction, whereas in the −33 mode, the force is applied along the poling direction.

The electromechanical behaviour of the cantilever energy harvester (DuToit and Wardle, 2007) can be expressed as,

$$m\ddot{z} + c\dot{z} + kz - \theta V = -m\ddot{y} \qquad (1.11)$$

$$\theta\dot{z} + C_p\dot{V} + \frac{1}{R}V = 0 \qquad (1.12)$$

Where *m, c* and *k* are mass, damping, and stiffness of the energy harvester, respectively. *z* is relative displacement, and *y* is a base acceleration from the host structure. The electromechanical coefficient is given as θ, V is the voltage and C_p and R are the capacitance and load resistance, respectively.

Piezoelectric energy harvesters generate electrical energy by converting fluctuations in the strain to the active piezoelectric material within the devices. The electromechanical behaviour (IEEE 1988) can be expressed through the fundamental linear equations consisting of piezoelectric strain and electric displacement represented by,

$$S_p = S_p^E T_q + d_p E_k \qquad (1.13)$$

$$D_i = d_{ip} T_q + \varepsilon_{ik}^T E_k \qquad (1.14)$$

where, S_p represents the mechanical strain tensor; D_i denotes the electric displacement; T_q is stress tensor; d_{ip} is strain coefficient matrix; E_k is applied external electric field vector; S_p^E is elastic compliance coefficient at the constant electrical field; and ε_{ik}^T dielectric permittivity at constant stress.

1.5 Gaps in Literature

The following gaps are identified from the review as follows:

i. Limited studies on the factors influencing the efficiency of the voltage output from piezoelectric material on geo-structures.
ii. There are insignificant studies on the effect of confined granular fill on the efficiency of *PZT* voltage output.
iii. Limited studies have been proposed for piezoelectric energy output from geo-structures due to dynamic loading.
iv. Applications of piezoelectric material for energy harvesting from the ambient vibrations of geo-structures need to be further investigated.

1.6 Scope and Objectives of Research

The main aim of this research is to evaluate the dynamic response analysis of confined granular fill with *PZT* patches. The research scope includes theoretical and experimental studies for the performance evaluation of *PZT* patches embedded in confined granular fill. Based upon the literature review and the gap in studies, the objectives of this research are identified as,

i. To understand and analyze the dynamic response of wall retaining granular fill.
ii. To examine the frequency-time characteristics of vibrations in wall retaining granular fill.
iii. To perform parametric studies considering (a) displacement, (b) acceleration, (c) stress-strain and (d) damping characteristics of confined granular fill using *PZT* sensors.
iv. To capture the voltage output due to dynamic loads on confined granular fill using *PZT* patches.
v. To evaluate the application of *PZT* patches for energy output due to dynamic loads on wall retaining granular fill.

1.7 Publications Based on Present Research

Throughout the research process, efforts were made to format the thesis as research papers that could be submitted to peer-reviewed international journals and conference proceedings for publication consideration. The details of the published or prepared papers are as follows:

i. Kumari, N., & Trivedi, A. (2022). Factors Influencing Piezoelectric Response of Horizontally and Vertically Embedded *PZT* Patch in Confined Granular Fills. Advances in Materials Science and Engineering, 2022. https://doi.org/10.1155/2022/7860273 (SCIE Indexed).

ii. Kumari, N., & Trivedi, A. (2022). The Effect of Confined Granular Soil on Embedded *PZT* Patches Using FFT and Digital Static Cone Penetrometer (DSCP). Applied Sciences, 12, 9711. https://doi.org/10.3390/app12199711 (SCIE Indexed)

iii. Kumari, N., & Trivedi, A. (2022). A Review on Modelling and Techniques Used for Piezoelectric Power Generation from Vibration of Geo-Structures. e- Prime- Advances in Electrical Engineering, Electronics and Energy, 100076. https://doi.org/10.1016/j.prime.2022.100076 (Elsevier)

iv. Kumari, N., & Trivedi, A. (2018). Application of semi-active control strategy for the wall retaining granular fills. In Proceedings of China-Europe Conference on Geotechnical Engineering, 978-982. Springer, Cham. https://doi.org/10.1007/978-3-319-97115-5_20 (SCOPUS)

v. Kumari, N., & Trivedi, A. (2020). Vibration Control of Flexible Retention Systems. In Advances in Computer Methods and Geomechanics, 529-539. Springer, Singapore. https://doi.org/10.1007/978-981-15-0890-5_44 (SCOPUS)

vi. Kumari, N., & Trivedi, A. (2020). Semi-active Control Strategy for Horizontal Dynamic Loading on Wall Retaining Granular Fills. In Sustainable Civil Engineering

Practices, 71-79. Springer, Singapore. https://doi.org/10.1007/978-981-15-3677-9_8 (SCOPUS)

vii. Kumari, N., & Trivedi, A. (2019). The application of *PZT* patch as energy harvester in dynamically loaded retaining structures, Int. In Symposium on Testing and Technology for Bearing Capacity of Deep Foundation, Delhi, 21-22. ISBN: 978-93-5391-519-3

1.8 Structure and Organization of Thesis

This thesis is organised into seven chapters: a general introduction, literature review, seven research articles and summary of conclusions and recommendations for future research.

Chapter 1 presents a brief introduction of the dynamic response of confined granular and *PZT* patches. And also presents the highlights on the contribution of embedded *PZT* patches in civil engineering.

Chapter 2 discusses the detailed summary of the literature of the previous studies pertinent to this research. Experimental, theoretical, and field studies on application of the *PZT* patch in geo-structures are presented. And the limitations that can be linked to research to achieve the goal of the current study are also analysed.

Chapter 3 describes the theoretical analysis of the average stress and strain for vertical and horizontal dynamic loading on wall retaining granular fill using a *PZT* patch. The influence of the width and modulus of the material has also been numerically evaluated by considering the granular sand as a backfill.

Chapter 4 presents a parametric investigation of the factors influencing the piezoelectric voltage generation considering the installation position of the *PZT* patch, geometric and mechanical properties of the embedded *PZT* patch in confined granular fill.

Chapter 5 is devoted to experimental investigation on confined granular fill with *PZT* patches with the potential use of the FFT analyzer, oscilloscope and dynamic cone penetrometer.

Chapter 6 deals with the experimental and theoretical investigation of the strain sensitivity, power and energy output of embedded *PZT* patches in confined granular fill.

Chapter 7 Outlines the findings of the current investigation, emphasises the significant advances made in understanding, and proposes possible directions for further investigation.

1.9 Benefits to Practitioners, Researchers and Industry

This section unveils the benefits to practitioners, researchers and industry as follows,

Pioneering Structural Health Monitoring: This study empowers practitioners to enhance structural health monitoring by integrating PZT patches into geo-structure, enabling early issue detection and cost savings in maintenance.

Empowering Smart Cities: This research aligns with the mission of smart cities, providing tools to harness mechanical energy from urban vibrations for sustainable energy solutions and greener cities to benefit of society and industry.

Environmental Sensing and Informed Decision-Making: The investigation contributes to environmental sensing, providing valuable data for environmental agencies and industries to inform decision-making and improve urban environments.

Geo-structural Optimization: This research advances geo-structural engineering, enhancing the design and performance of retaining walls and granular fills in dynamic environments, addressing real-world structural challenges and promoting safety and efficiency.

Chapter 2

Literature Review

This chapter contains passages from pertinent literature compiled to reflect current and emerging practices in the relevant research domain. It is based on the article published in e- Prime- Advances in Electrical Engineering, Electronics and Energy, Elsevier as listed in section 1.8.

2.1 Introduction

Vibration-based energy harvesting has been used for piezoelectric transduction from civil infra-structure system applications with moving loads and surface strain fluctuations (Erturk 2011). Two approaches were used for power generation from moving loads. The first one is based on using a bimorph cantilever located on a simply supported slender bridge. The cantilever energy harvester was obtained to couple with the generalized electromechanical equations for transient excitation. The second approach considered using a thin piezoceramic patch covering a region on the bridge. Analytical expressions of the electrical power output are presented for generalized, harmonic and two-dimensional strain fluctuations. The study concluded that piezoceramic patches offer a unique option for energy harvesting directly from the surface strain fluctuations of various civil structures.

The mechanical energy of vibrations of roads, bridges, and retaining structures can be converted by utilizing electromechanical conversion (Tian and Deng, 2014; Lv et al., 2015). The conversion of mechanical energy depends upon the energy stored in the material using an implement consisting of *PZT*. Few researchers analyzed the feasibility of power generation from vehicle-induced vibration on bridges and pavement (Ashebo et al., 2008; Moure et al., 2016). The power output of mechanical energy has been significantly influenced by the

parameters of material properties, frequency of the vibration, and stress-strain characteristics of the material. A piezoelectric generator could generate 100mW power from railway track vibrations (Tianchen et al., 2014).

In the last decade, a considerable number of attempt has been made to generate significant power from civil structures. Structural elements and numerical methods are developed to convert wasted mechanical energy into electrical energy. The parameters, namely geometric design, orientation, moving loads, frequency, and dynamic response of the system considered (Ashebo et al., 2008; Karimi et al., 2016; Lv et al., 2015; Varadha and Rajakumar, 2018). Piezoelectric materials have been used for vibration control (Kumari and Trivedi, 2020), structural health monitoring (Galchev et al., 2011; Shanker, Bhalla et al., 2011), and smart construction materials (Li et al., 2007). The vibration power generation technique also reduces the noise in a delicate timber building (Wei and Jing, 2017). The application of piezoelectric power harvesting in civil engineering is broadly explained in Fig 2.1. The power output can be utilized for wireless devices, structural health monitoring sensors (Elvin et al., 2006; Gu et al., 2006; Soh et al., 2000), hybrid electric vehicles, and traffic lights (Jung et al., 2011).

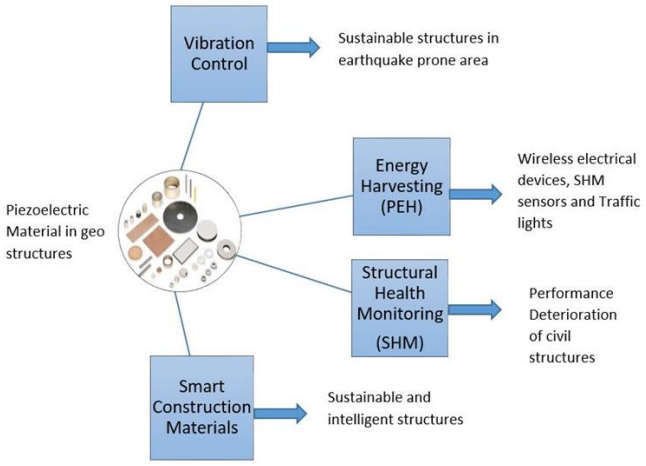

Fig. 2.1 Piezoelectric applications in structures utilizing mechanical vibrations

The piezoelectric energy harvesting from the vibrations of a functional grade beam was found to be induced by multi-moving forces and masses (Amini et al. 2017). The finite element

method was used to analyze the electromechanical behaviour of a piezoelectric harvester in a unimorph configuration. For the transient analysis, Newmark's explicit integration technique was adopted. It was assumed that the material properties of the beam and piezoelectric patch vary continuously in the thickness direction according to the power-law form. The effects of different material distributions and velocities of moving loads were discussed. The study concluded that remarkable electrical power could be generated from the vibration of a beam subjected to moving loads and masses.

This section provides a comprehensive survey of the recent advances in modelling and numerical techniques for utilising mechanical vibration of geo-structures for piezoelectric power generation. The detailed research methodology of the review is shown in Fig. 2.2. The modelling of various *PEH*s used in the basements, retaining walls, pavements, bridges and railway tracks are discussed. The working principles and numerical techniques, namely, the finite element method and dynamic stiffness method are demonstrated for power generation from mechanical vibration of structures. This study focuses on several important aspects of using *PEH*s in civil engineering, including structural geo-materials, geometric design and numerical methods. Different *PEH*s are compared in terms of power output from the granular subcases, pavements, bridges and railway tracks. The advantages and limitations of piezoelectric power generation modelling and techniques are presented. The future research recommendations of piezoelectric power generation from ambient vibration of geo-structures are discussed.

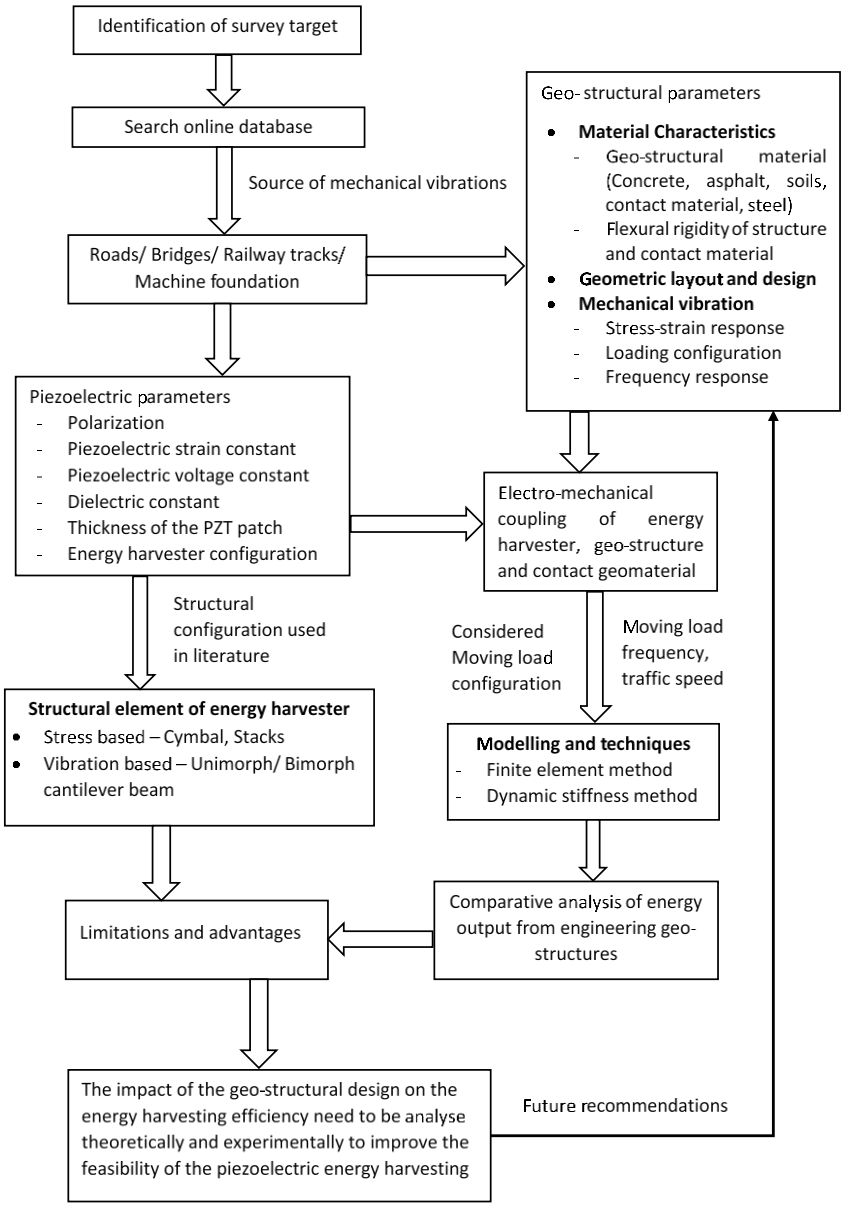

Fig. 2.2 Flow chart for power generation from mechanical vibration of the geo-structure

The literature review indicates that the application of piezoelectric material in civil structures is an abundant energy source. The existing experimental and numerical analysis usually focuses on the methods of piezoelectric energy from various structural elements, namely beams, bridges, roads, and rail tracks. In contrast, no significant studies exist on the stress response of confined granular fill on power generation due to vibrations. The *PZT* patches embedded in the pavement undergo a reversal in the voltage polarity for both horizontal and vertical faces (Yang et al., 2020). Therefore, the piezoelectric power output is not necessarily higher for the stronger

vibrations. The power output depends on the magnitude of strain generation due to vertical and horizontal vibrations. From previous analytical studies (Chen et al., 2016; Yang et al., 2020), the resultant vertical and horizontal stresses are affected by the placement of the *PZT* patch on the retaining face compared to the horizontal pavement structure. Similar observations were made (Zhao et al., 2012) for the increasing depth of embedment of the *PZT* patch. The analytical study helps us to identify the set of design parameters that can improve the efficiency of the piezoelectric energy output. The efficiency of charge output depends upon the magnitude of the force excitation, the material characteristics, and the electromechanical coupling of the piezoelectric material structure (Ren, 2004; Singh et al., 2013). The piezoelectric response of the *PZT* patch can be optimized by changing the mechanical properties through variation in the modulus (Petroff et al., 2019).

2.2 Structural Elements and Modelling

This section describes the advancement of the structural elements and modelling the energy harvesters for utilising the mechanical vibrations from structures. Many researchers proposed the different structural elements of the harvester for the conversion of mechanical vibration of structures namely, bridges (Ali et al., 2011; Jung et al., 2011; Peigney and Siegert, 2013; Soh et al., 2000) and pavements (Duarte et al., 2018; Lv et al., 2015; Xu et al., 2018; Zhang et al., 2016; Zhao et al., 2012), retaining walls (Kumari and Trivedi, 2018; Kumari and Trivedi, 2020). The structural element modelling was designed based on the stress-strain response of the structures.

The selection of the structural element for the energy harvester has been made based on the frequency of the mechanical vibrations. To harvest the energy from the low-frequency vibrations stress-based harvesters are used as shown in Fig 3. The stacks and cymbal structure elements are most widely used in converting low-frequency vibration from structures (Kim et

al., 2004). The piezoelectric cymbal transducer provides a potential power generation under environmental dynamic loads such as moving loads on roadways pavements. Due to stiffness consistency and energy conversion efficiency, the cymbal and bridge transducer design has been recommended. The Cymbal piezoelectric transducers can generate power (1.2mW) at a 20Hz frequency for each passing vehicle and the electrical voltage generated around 97.33 V (0.06J) per vehicle from asphalt pavement. The deformation of the pavement due to mechanical vibration changes the coupling of cymbal transducers and affects voltage generation (Zhao et al., 2012; Zhao et al., 2010). The maximum 65MWh power could be produced from a 100 m roadway with around 30,000 piezoelectric transducers in a year (Moure et al., 2016).

In a piezoelectric cymbal transducer-based energy harvester, the direct piezoelectric effect is considered, and polarization occurs on the vertical surface of the *PZT* material. The mathematical relation between piezoelectric polarization of the cymbal transducer and stress due to mechanical vibration (Zhao et al., 2010) is expressed as,

$$P_3 = \sum_{i=1}^{i=6} d_{3i} T_i \qquad (2.1)$$

where P_3 is the piezoelectric polarisation in the 3rd principal direction, d_{3i} is the piezoelectric strain constant, and T_i is the stress tensor.

The initial electric field generated in *PZT* can express as,

$$E_3 = \frac{P_3}{\varepsilon_{33}^T} \; or \; E_3 = \sum_{i=1}^{i=6} g_{3i} T_i \qquad (2.2)$$

The *PZT* patch polarization generates the voltage that can be calculated from the following equation,

$$V_3 = \int E_3 dt_p = \sum_{i=1}^{i=6} g_{31} T_i dt_p \qquad (2.3)$$

where g_{3i} is the piezoelectric voltage constant of the $PZT\left(g_{3i} = \frac{d_{3i}}{\varepsilon_{33}^T} \right)$, t_p is the thickness of the PZT and ε_{33}^T is the relative dielectric constant in the third principal direction. The power output of the piezoelectric cymbal transducer-based energy harvester is expressed as,

$$U_E = \frac{1}{2} P_3 E_3 A t_p = \frac{1}{2} V^2 \frac{\varepsilon_{33}^T \varepsilon_o A}{t_p} \qquad (2.4)$$

where, U_E is the harvested electric energy, and A is the surface area of the PZT patch.

The mechanical and electrical behaviour of piezoelectric stack embedded in asphalt pavement found excellent power sources using the finite element method (Lv et al., 2015). The stack piezoelectric devices installed on the railway track could harvest energy up to 1000mJ when the stiffness increased significantly (MN/m) (Wang et al., 2015). The piezoelectric stack transducer consists of a displacement sensor, a compression spring, a piezoelectric stack, and force transmission units. The inertial force in the transducer is neglected for simplification. Mathematical modelling has been proposed to analyze the voltage output (Zhao and Erturk, 2014). The vertical stress due to moving loads is expressed as,

$$\sigma_Z = q(t) = \frac{K_s \omega}{A} \qquad (2.5)$$

where K_s is the stiffness of the compression spring, ω is the excitation frequency, and A is the contact area of loading. The stack-type harvesters consist of multiple no. of piezoelectric patches. Thus the constitutive equation of the piezoelectric layers is expressed as,

$$D_Z = nd_{33}\sigma_z + n\varepsilon_{33}^{\sigma}E_z \qquad (2.6)$$

where nd_{33} and nk_{33}^{σ} are the effective piezoelectric strain and dielectric constants of the stack, which depend upon stresses due to the mechanical vibrations, respectively. D_z is the electrical displacement in the vertical direction. The voltage across the resistance is expressed as,

$$\frac{d}{dt}\left(\int_A D_z dA\right) = \frac{V(t)}{R} \qquad (2.7)$$

where *A* is the area of the piezoelectric element. For the harmonic vibrations [$q(t) = q_o e^{j\omega t}$], the complex voltage is expressed as,

$$V_o = \frac{j\omega n d_{33} A q_o}{j\omega C_p + (1/R)} \qquad (2.8)$$

The capacitance (C_P) is the component of the electrical circuit. The steady-state voltage is calculated using $V(t) = V_o e^{j\omega t}$.

The vibration-based energy harvesters convert the vibration from the bridge, and railway tracks into electrical energy. The vibration-based energy harvesters consist of a layer of piezoelectric material with a flexible cantilever beam with tip mass as shown in Fig. 3 (b). The change in the thickness of the *PZT* patch, tip mass and loading conditions influence the power output from the mechanical vibrations (Negi et al., 2019; Z. Zhang et al., 2019). The 0.53mW of power was generated from one harvester at a load resistance of 60KΩ from bridge vibrations(Zhang et al., 2018).

There are several models proposed for a piezoelectric cantilever-based harvester. For the piezoelectric dynamic system (Erturk and Inman, 2008; Erturk and Inman, 2009). The electromechanical coupling effect of the cantilever energy harvester is based on the Euler-Bernoulli beam theory and Gaussian law. The governing equation of motion and voltage output

for the cantilever-based bimorph energy harvester for the transverse forced vibrations for the external damping is expressed as,

$$EI\frac{\partial^4 w_{rel}(x,t)}{\partial x^4}+C_S I\frac{\partial^5 w_{rel}(x,t)}{\partial x^4\partial t}+C_a\frac{\partial w_{rel}(x,t)}{\partial t}+m\frac{\partial^2 w_{rel}(x,t)}{\partial t^2}+\vartheta V(t)\left[\frac{d\delta(x)}{dx}-\frac{d\delta(x-L)}{dx}\right]$$
$$=\left[-m+M_t\delta(X-L)\right]\frac{\partial^2 w_b(x,t)}{\partial t^2}-C_a\frac{\partial w_b(x,t)}{\partial t} \qquad (2.9)$$

$$\frac{V(t)}{R}+C\frac{dV(t)}{dt}+\vartheta\int_0^L\frac{\partial^3 w_{rel}(x,t)}{\partial x^2\partial t}dx=0 \qquad (2.10)$$

where, the bending stiffness is *EI*, $w_{rel}(x,t)$ and $w_b(x,t)$ are the transverse displacement of beam and base, respectively, C_a is the viscous air-damping coefficient, m is the mass per unit length and C_S is the strain-rate damping coefficient. $V(t)$ is the voltage in the circle, C is the internal capacitance of the piezoelectric layer, R is the external resistance, M_t is the participating mass, and ϑ is the coefficient of the background coupling terms.

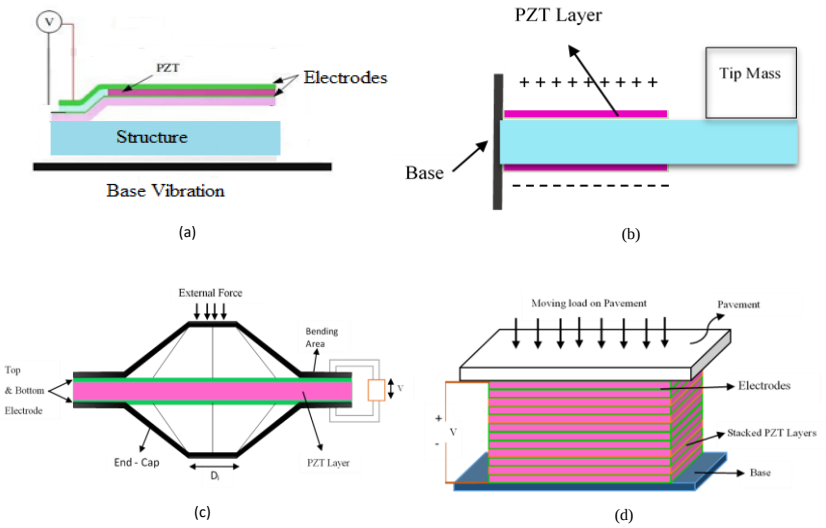

Fig. 2.3 The piezoelectric elemental structures (a) Unimorph piezoelectric cantilever beam (b) Bimorph piezoelectric cantilever beam with tip mass (c) The design of cymbal transducer made of PZT material (d) The geometry of piezoelectric stack for structure.

The unimorph energy harvester could generate about 13.8V under cyclic loading of 10kN (Kim et al., 2011). The moving vehicle modelling and surface conditions change the coupling effect of the piezoelectric cantilever energy harvester significantly (Zhang et al., 2014). A Bimorph Cantilever beam with a thin PZT patch could produce 1mW of power at 25Hz (Erturk, 2011).

2.3 Numerical Techniques

Past research showed that ambient vibrations are a good power source (50 -250μW/cm^3) due to their easy accessibility in structural fields (Lv et al., 2015; Paradiso and Starner, 2005; Roundy et al., 2003). Various methods have been used to understand the feasibility of piezoelectric power generation from the mechanical vibration of the structure and its ability to produce significant power. The two types of methods finite element method and dynamic stiffness method are presented to analyse the dynamic response of the piezoelectric structure and geo-structures.

2.3.1 Piezoelectric Finite Element Method

The structure analysis of embedded or bonded piezoelectric sensors requires the precise electromechanical modelling of mechanical and electrical responses. The finite element model for piezoelectric power generation has been utilized to discretize the electromechanical phenomenon. The finite element method of piezoelectric material is widely used for power generation from dynamic loads (Tianchen et al., 2014). The structure is divided into finite numbers of non-overlapping elements in the finite element analysis to calculate the unknowns at different nodes. The mechanical displacement (u), applied force (f) and electrical potential are evaluated using nodal values of mechanical displacement $\{u(x_i, y_i)\}$ and the electric potential $\{\phi(x_i, y_i)\}$. The corresponding displacement nodal shape function can be defined as a potential nodal shape function $[N_\phi(x_i, y_i)]$. For the n no. of nodes, the mechanical displacement function has been evaluated using the following equations:

$$\{u(x,y\} = [N_u(x_i, y_i)]\{u(x_i, y_i\} \quad (2.11)$$

$$\{\phi(x,y\} = [N_\phi(x_i, y_i)]\{\phi(x_i, y_i\} \quad (2.12)$$

Therefore, using the constitutive equation of piezoelectric material the strain $\{\varepsilon\}$ and electric field $\{E\}$ is defined as,

$$\{\varepsilon\} = [B_u]\{u(x_i, y_i\} \quad (2.13)$$

$$\{E\} = -[B_\phi]\{\phi(x_i, y_i\} \quad (2.14)$$

Substituting the strain–displacement and electric potential in the equation of motion, the couple electromechanical has been obtained for the finite piezoelectric model as,

$$\{M\}\{\ddot{u}_i\} + [K_{uu}]\{u_i\} + [K_{u\phi}]\{\phi_i\} = \{F(x_i, y_i)\} \quad (2.15)$$

$$[K_{\phi u}]\{u_i\} + [K_{\phi\phi}]\{\phi_i\} = \{Q_i\} \quad (2.16)$$

where, $\{M\}$ is the dynamically consistent mass matrix, $[K_{uu}]$ is stiffness matrix, $[K_{u\phi}]$ is piezoelectric stiffness matrix, and $[K_{\phi\phi}]$ is dielectric stiffness matrix.

The finite element model provides the power output efficiency of the *PEH* (Guo and Lu, 2017; Song, 2019a). The finite element method is used to analyse the deformation, dynamic load response, and structural parameters of the structures namely, pavement, bridge and railway tracks (Amini et al., 2017; Jing et al., 2007; Patzák, 2012; Qi et al., 2015; C. Sun et al., 2013). The displacement profile of the system is significantly affected by the stiffness matrix. For the advancement in the modelling of dynamically loaded structures, the material stiffness of the different layers of the system is requisite. For geo-structures, the stiffness matrix can be evaluated from the equivalent stiffness of the different layers of the system. By implementing this concept, Eq. (2.15) can be modified as follows,

$$\{M\}\{\ddot{u}_i\} + [K_{eq(uu)}]\{u_i\} + [K_{u\phi}]\{\phi_i\} = \{F(x_i, y_i)\} \quad (2.17)$$

$[K_{eq(uu)}]$ is the equivalent stiffness matrix for the displacement in multiple layers of the geo-structure.

2.3.2 Dynamic Stiffness Method

The dynamic stiffness method is based on the exact solution of the wave equation. The finite element method is more complex than the dynamic stiffness method. It works on the concept of frequency response functions. The dynamic stiffness method is utilized to model beams with arbitrary boundary conditions. A dynamic stiffness method was proposed for modelling power generation beams based on the exact solution of the wave equation of motion (Bonello and Rafique, 2011). The equation of motion bimorph piezoelectric harvester is expressed as,

$$B\frac{\partial^4 u}{\partial x^4} + A\frac{\partial^5 u}{\partial x^4 \partial t} + C_a\frac{\partial u}{\partial t} + m\frac{\partial^2 u}{\partial t^2} = 0 \qquad (2.18)$$

$$B = Y_p I_p + Y_{sh} I_{sh} \; ; \; A = c_p I_p + c_{sh} I_{sh} \qquad (2.19)$$

where C_a is the viscous damping coefficient, *u* is the displacement, *m* is the mass per unit length, *B* is the bending stiffness of the bimorph energy harvester, and *A* is the structural damping. The dynamic stiffness method assumed harmonic excitation. The harmonic excitation of the system can be expressed as,

$$u(x,t) = \mathrm{Re}\{\bar{u}(x)e^{iwt}\} \qquad (2.20)$$

The dynamic stiffness matrix *D* of the beam with tip mass is expressed as,

$$f = Du \qquad (2.21)$$

where, $f = \begin{bmatrix} \bar{F}_o & \bar{\Gamma}_0 & \bar{F}_l & \bar{\Gamma}_l \end{bmatrix}^T$ and $u = \begin{bmatrix} \bar{u}_o & \bar{\theta}_0 & \bar{u}_l & \bar{\theta}_l \end{bmatrix}^T$

The dynamic stiffness D_e of the beam without tip mass is expressed as,

$$f_e = D_e u \qquad (2.22)$$

where $f_e = \left[\bar{F}_o \quad \bar{\Gamma}_0 \quad \bar{F}_{le} \quad \bar{\Gamma}_{le} \right]^T$ and $\bar{u}$ and $\bar{\theta}$ are the complex amplitude of displacement and rotation of the cantilever beam energy harvester, f and u are vectors of the complex amplitude and displacement, respectively. The dynamic stiffness method allows structures embedded with piezoelectric patches to respond in arbitrary high-frequency frequencies (Khiem et al., 2020).

2.4 Power Generation from Mechanical Vibration

2.4.1 Mechanical Vibration of Pavement and Subgrade

This section provides the application of different energy harvesters to generate electrical energy from the mechanical vibration of the pavement due to dynamic load. The coupling of the *PEH* and the pavements significantly affects the power output. The polarization of the piezoelectric material is directly proportional to the mechanical stress of the pavement and subgrade due to moving loads (Eq. 2.1). Table 2.1 summarises the comparative voltage generation from the applied force of moving vehicles on the structures. The electrical potential is sensitive to the vertical load on the pavement, frequency and no. of the piezoelectric disk (Roshani et al., 2016). The moving loads due to heavy vehicles are considered to increase the power generation efficiency from the pavement and subgrade due to higher stress (Kumari and Trivedi, 2018; Kumari and Trivedi, 2020). The Cymbal piezoelectric transducers can generate power (1.2mW) at a 20Hz frequency for each passing vehicle and the electrical voltage generated around 97.33 V (0.06J) per vehicle (Zhao et al., 2012; Zhao et al., 2010). The cymbal piezoelectric harvester generates 16μW power for the passage of each heavy vehicle from asphalt pavements (Moure et al., 2016). The piezoelectric stacks suit high loading conditions, low frequency, and pavement compatibility (Lv et al., 2015).

Moreover, the bridge transducer for power generation and produced a significant electrical potential (556V) for 0.7 MPa applied stress (Jasim et al., 2017). The increased number of

piezoelectric elements in the power generation pavement system enhances the power output. Approximately 65MWh power could be produced from a 100 m roadway with around 30,000 piezoelectric transducers in a year (Moure et al., 2016). The output power and power conversion efficiency of a piezoelectric transducer are determined by the geometric design and the placement in the pavement and subgrade. The embedment depth affects the magnitude of stress on the energy harvester, which vitally affects the power output from airfield pavements (Jasim et al., 2019; Zhao and Wang, 2020). The effect of geo-structure and PEH stiffness on the electromechanical coupling can be analysed using the varied analytical techniques shown in Table 2.2.

Table 2.1 Comparison of output potential difference as per harvesting technologies for substructures

Type of Piezoelectric harvester	Stress (MPa)	Potential difference (V)	Power output (mW)
Bridge transducer [a]	0.7	556	28.7
Static loading prototype containing four *PZT* disks [b]	5	650	-
Composite piezoelectric transducer [c]	0.21, 0.35, 0.71	22, 36, 70	-
Ball-type protective pad with transducers [d]	0.7, 0.2	-	50.41, 2.92
Cymbal piezoelectric transducer [e]	0.7	-	1.2

[a] Jasim et al. (2017), [b] Roshani et al. (2016), [c] Xu et al. (2018), [d] Wang et al. (2018), [e] Zhao et al. (2010)

Table 2.2 The analytical techniques for the conversion of mechanical vibrations to electrical energy from structures namely pavements, subgrade, and retaining structures

Technique	Input	Output
Vibration control of flexible retention systems [a]	The generalized equation of the spring-mass system $m\ddot{u} + k_{hp}u + k_{hs}u = F\sin(\omega t + \beta)$	Horizontal and vertical displacement amplitude and effect of the stiffness of the structure
The deformation of pavement system subjected to moving [b]	The response of the pavement system $w(x,t) = \frac{P}{2\pi}\int_{-\infty}^{\infty}\frac{\sin(r_0\xi)}{r_0\xi} \times \frac{e^{i\xi(x-vt)}}{EI\xi^4 + k(1+2iD) - \rho(v\xi)^2}$	Parametric study to understand the effect of damping and velocity of vehicles on the power output
Cymbal piezoelectric harvester embedded in asphalt pavement [c]	The electric energy stored in the Cymbal $U_E = \frac{1}{2}P_3E_3At_P = \frac{1}{2}V^2\frac{\varepsilon_r^T\varepsilon_0 A}{t_P}$ The displacement difference percent $pd = \frac{d_{wo} - d_w}{dw_o}\times 100$	The efficiency and coupling effects with a pavement of Cymbal with various sizes

Technique	Input	Output
The transformation of asphalt layers into a *PEH* using the 3-D electromechanical model and Cymbal *PZT* [d]	The equation of three-degree of freedom electromechanical model $m_a\ddot{x}_a + k_a(x_a - x_p - x_b) + c_a(\dot{x}_a - \dot{x}_p - \dot{x}_b) = Q_0\,\mathrm{Cos}(wt)$ $m_p\ddot{x}_p + nk_p(x_p - x_b) + nPV_p = Q_0\,\mathrm{Cos}(wt) - m_a\ddot{x}_a$ $nk_p(x_p - x_b) + nPV_p = m_b\ddot{x}_b + c_b\dot{x}_b + k_b x_b$ $-nP\dot{x}_p + nC_pV_p + \frac{V_p}{R} = 0$	The voltage outputs are analysed for different material properties, stiffness, shear modulus, piezoelectric layer design, and external dynamic loading conditions
Roadway energy harvester contains piezoelectric multilayer stacks [e]	The constitutive equations of the piezoelectric stack $\begin{bmatrix} F_p \\ Q \end{bmatrix} = \begin{bmatrix} k_2 & -N \\ N & C_2 \end{bmatrix} \begin{bmatrix} x_2 \\ V_p \end{bmatrix}$	The harvester can generate sufficient energy for driving the equipment used in transportation infrastructure. K_2 represents the elastic coefficient

[a] Kumari and Trivedi (2020), [b] Xiang et al. (2013), [c] Zhao et al. (2010), [d] Guo and Lu (2017), [e] Jiang et al. (2014)

2.4.2 Mechanical Vibration of Railway Tracks, Bridges, and Retaining Structures

Railway tracks, bridges, and railway tracks are the ambient vibration sources in civil structures. To harvest the piezoelectric energy, the analysis of the displacement due to moving loads of the railway tracks, bridge, and retaining structures (Kumari and Trivedi, 2020; Kumari and Trivedi, 2022). Various piezoelectric structural elements have been utilized to enhance the power output from the mechanical vibration of the bridge. The vibration-based cantilever energy harvesters are most suitable due to the electromechanical coupling effect. The cantilever beam creates a higher strain in the harvester for low-intensity ambient vibrations. A bimorph cantilever beam with a thin *PZT* patch could produce 1mW of power at 25Hz (Erturk, 2011). The unimorph energy harvester could generate about 13.8V under cyclic loading of 10kN from a steel-beam slab bridge (Kim et al., 2011). To generate a high electric effect, load amplitude, loading frequency and the resultant strain should be considered and its piezoelectric effect can be assessed based on the generated electric effect per unit strain based on the coupling coefficient.

The enhanced frequency of non-linear energy harvesters improves power generation efficiency (Cveticanin et al., 2017; Gammaitoni et al., 2009; Mann and Owens, 2010). The dynamic non-linear response of low-frequency vibrations is based on mechanical and electrical energy coupling (Green et al., 2013). To obtain the maximum power from bridge vibration, the resonant frequency must match the resonant frequency of the harvester (Cahill et al., 2018; Erturk, 2011). The multi-impact energy harvesters with a natural frequency of fewer than 10 Hz are used for the low-frequency vibrations of the bridge (Galchev et al., 2011; Zhang et al., 2014). The high-frequency piezoelectric cantilever harvester showed better results than low-frequency vibrations.

Table 2.3 Analytical techniques used for power generation applicable to geo-structures

Technique	Input	Output
Piezoelectric cantilever beam harvester [a]	$EI\frac{\partial^4 w_{rel}(x,t)}{\partial x^4}+C_S I\frac{\partial^5 w_{rel}(x,t)}{\partial x^4 \partial t}+C_a\frac{\partial w_{rel}(x,t)}{\partial t}$ $+m\frac{\partial^2 w_{rel}(x,t)}{\partial t^2}+\vartheta V(t)\left[\frac{d\delta(x)}{dx}-\frac{d\delta(x-L)}{dx}\right]$ $=\left[-m+M_t\delta(X-L)\right]\frac{\partial^2 w_b(x,t)}{\partial t^2}-C_a\frac{\partial w_b(x,t)}{\partial t}$	Parametric study of cantilever *PEH*
A bimorph *PEH* subjected to permanent axial loading [b]	The generalized equation of the system $M_T\ddot{r}(t)+C\dot{r}(t)+(K_T+\tilde{K})r(t)-\Theta\upsilon(t)=0$ $\Theta^T\dot{r}(t)+C_P\dot{\upsilon}(t)=\dot{q}(t)$	The effect of the pre-stress parameters on the power generation
Bridge vibrations due to moving load, moving mass and moving oscillator [c]	Moving load model, the load on the bridge $p(\bar{x},t)=\begin{cases}p\delta(\bar{x}-\upsilon t), & 0\le t\le t_d\\ 0, & t\ge t_d\end{cases}$ Moving mass model, the load on the bridge $p(\bar{x},t)=\begin{cases}M\left\{g-\left[\ddot{\bar{w}}(\bar{x},t)+\ddot{\eta}(\upsilon t)\right]\right\}\delta(\bar{x}-\upsilon t), & 0\le t\le t_d\\ 0, & t\ge t_d\end{cases}$	More power can be generated with consideration of the unevenness of the surface. The unevenness effect does not apply to the moving load model
Power generation from a highway bridge vibration from a moving point load [d]	The dynamic response of the bridge with a point load, *P* and velocity, *u* $m\frac{\partial^2 y(x,t)}{\partial t^2}+c\frac{\partial y(x,t)}{\delta t}+EI\frac{\partial^4 y(x,t)}{\partial x^4}=\delta(x-ut)P$	Parametric study to obtain the power output and design the energy management system

[a] Erturk and Inman (2009), [b] Rhimi and Lajnef (2012), [c] Zhang et al.(2019), [d] Ali et al. (2011)

Table 2.3 shows the power generated from the various piezoelectric harvester: cantilever energy harvester, Cymbal piezoelectric transducer, stack transducer, and finite element model.

It is observed that using the cantilever energy harvester highest power can be generated compared to others. The ambient vibrations from railway tracks and tunnels are used for sensors embedded to monitor structural health (Wischke et al., 2011). The railway track vibrations at maximum load can be converted into a voltage of 50-70V and power of 100mW for wireless sensors (Tianchen et al., 2014). Passenger trains produced more power output (0.59mW) than freight trains 0.03mW (Cahill et al., 2014).

Table 2.4 The power output from mechanical vibrations of traffic loads

Type of Model	Piezoelectric properties				
	Elastic stiffness of *PZT*, (GPa) *Ep*	Piezoelectric strain constant (C/m^2) d_{31}	Piezoelectric strain constant (C/m^2) d_{33}	Density of *PZT* (Kg/m^3)	Power (mW)
Cantilever *PEH* (Bridge) [a]	56	10.4	-	7450	400
Piezoelectric stack transducer (Railway Track) [b]	62.22	-186	700	7450	0.15
Finite element *PZT* model (Train-Bridge) [c]	71	-274	-	7450	0.4

[a] Zhang et al. (2019), [b] Wang et al. (2015), [c] Cahill et al. (2014)

The geometric layout of the structure and installation position significantly affects the power output efficiency of the energy harvester (Song, 2019b). Each piezoelectric patch in a stack at the bottom of a steel rail could harvest energy up to 1000mJ when the stiffness increased significantly (Wang et al., 2015). It is observed from the literature that dynamic response parameters, namely acceleration, frequency, and damping of moving loads, significantly affect the piezoelectricity and power output.

2.5 Composition of *PZT* and Construction Material

This section analyses the potential application of piezoelectric material in health monitoring and vibration control. The property of *PZT* material allows possibilities for implementing sustainability through vibration control, structural health monitoring and smart construction materials (Li et al., 2007; Shen et al., 2006). The cement-*PZT* composites moderately produce the electrical current with the application of compressive force (Rong and Zhifei, 2011; Sun et al., 2004). The electromechanical impedance technique is used for monitoring the cement compositions using piezoelectric materials, which is the function of the density and stiffness of the material (Amini et al., 2017; Ghafari et al., 2018; Shen et al., 2006; Tawie and Lee, 2010). The geo-structural characteristics significantly affect the stress-strain behaviour (Kumari and Trivedi, 2018), which directly changes the impedance of the piezoelectric materials. The impedance of the *PZT* was analysed by changing the properties of the composite materials (Bhalla and Soh, 2004). The electromechanical effect of the *PZT* material is influenced by the piezoelectric coefficient (d_{33}), which depends on factors namely polarization, temperature, and fabrication (Gong et al., 2009). The researchers focused on the damage detection of concrete structures, steel structures and bridges using piezoelectric-based sensors (Ai et al., 2014; Soh et al., 2000; Yang et al., 2013). The mechanical behaviour of the *PZT*-cement composite is significantly affected by the material properties namely porosity and Young's modulus, participating mass, Poisson's ratio and energy transfer function (Dwivedi et al., 2020; Yu et al., 2016; Zhao and Wang, 2020). The polarization and electric admittance of the *PZT* material affect the potential of its application in structures (Dong and Li, 2005; Gong et al., 2011; Li et al., 2002; Shi and Wang, 2013; Wen and Chung, 2002).

The geo-structure sustainability can be improved by vibration control due to the dynamic loads. According to the concept of structure vibration control by adjusting the stiffness and mass parameter control of the dynamic variables such as displacement, velocity, and acceleration

(Yao, 1972). Consistent with it, a solution is developed to control the vibration of the retaining structure using the semi-active control strategy, considering the stress-strain response of the *PZT* patch (Kumari and Trivedi, 2018).

Table 2.5 Composites of *PZT* and construction material for power generation

Material composition	Piezoelectric property d_{33} (pC/N)	Polarization Voltage (kV/mm)
Cement-*PZT*- composite [a,b,c,d]	29-71	1.5
	20-80	1
	110-215	6
PZT-PVDF-cement composite [e]	15-25	1
Silica fume –cement –*PZT* composite [f]	18-20	2
Carbon black-cement –*PZT* composite [g]	2-30	4
Aluminium-cement –*PZT* composite [h,i]	0.5-7	0.6-1
Asphalt – *PZT* composite [j]	287	4-7.6
Geo-structures (granular fill and *PZT* composite) [k]	310-500	-

[a] Gong and Zhang (2009), [b] Wang et al. (2012) [c] Chaipanich and Jaitanong (2008), [d] Lam and Chan (2005), [e] Jaitanong et al. (2014), [f] Chainpanich (2007), [g] Gong et al. (2009), [h] Banerjee and Chennault (2014), [i] Rianyoi et al., (2016), [j] Guo and Lu (2017), [k] Kumari and Trivedi (2018)

Table 2.5 shows the composition of piezoelectric materials with construction materials like concrete, cement, and asphalt. The composite material concept promotes piezoelectricity and enhances the power generation capacity of the material.

It has been observed that power output is significantly affected by the parameters namely, contact geomaterial friction of the surface subjected to moving loads, vehicle types, vehicle speed, traffic volume, amplitude, and frequency of induced vibrations. Multilayer stack *PEH* in pavements with heavy traffic volume and speed of more than 30m/s can generate a maximum

power of 2kW (Jiang et al., 2014). The proper alignment position of *PEH* near the surface increases the contact pressure of moving vehicles on the structural elements. The impact pressure of moving vehicles increases the power output from the pavements (Zhao et al., 2010). The multilayer stacks and cymbal *PEH* are relevantly capable of improving the current and voltage for low-frequency stress conditions. To generate the maximum energy from the mechanical vibrations, the natural frequency of the *PEH* should be resonant with the natural frequency of the structures.

Chapter 3

Semi-active Strategy for Strain Response of Wall Retaining Granular Fill

This chapter is based on the two book chapters published in Proceedings of China-Europe Conference on Geotechnical Engineering, Springer and one conference paper in Advances in Computer Methods and Geomechanics, Springer as listed in section 1.8. The details are presented here with some changes in the layout to maintain consistency in the presentation throughout the thesis.

3.1 Introduction

The dynamic response of the geo-structure can be captured in two ways: (a) using smart materials such as *PZT* patches and (b) using strain gauges and sensors. The efficiency of the piezoelectric material depends on the intensity of vibration generated due to dynamic loads. It is analyzed in terms of acceleration and the natural frequency of vibrations. Three types of strategies are frequently used in civil engineering: passive control, active, and semi-active (Kerboua 2014).

This section analysis the average stress and strain for vertical and horizontal dynamic loading on wall retaining granular fill using a *PZT* patch. The influence of the width and modulus of the material has also been numerically evaluated by considering the granular sand as a backfill. The effect of the modulus ratio on the stress and strain curve has been plotted to show the variation between the quantities.

3.2 Semi-active Method

In the semi-active strategy sketched in Fig. 3.1, the actuators do not directly add mechanical energy to the structure; hence, bounded input and output stability are guaranteed. In a semi-active strategy, *PZT* patches are embedded, which utilize the motion of the structure to develop the resisting forces. This magnitude can be determined in terms of the stress-strain response of the wall retaining granular fill.

Fig. 3.1 is a block diagram of a semi-active control system with structure. Sensors and piezoelectric devices are highly distributed and integrated to control the vibration and perform self-sensing, self-actuation and self-diagnosing functions. Piezoelectric patches are used to counteract or cancel the dynamic vibration. Ideally, the force generated by the piezoelectric actuator has the same amplitude as the vibration but in anti-phase.

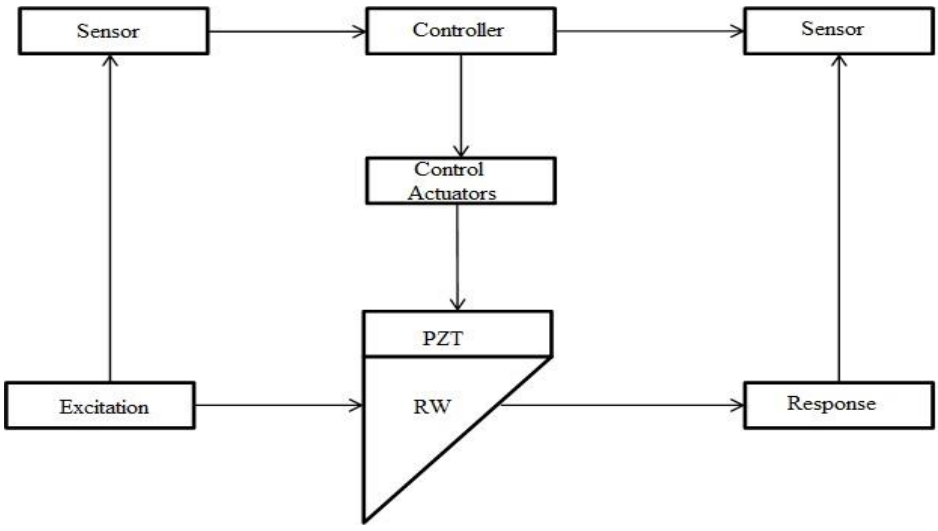

Fig. 3.1 Flow chart of semi-active control of dynamically loaded retaining granular fill

3.3 Stress-strain in *PZT* Patches

3.3.1 Stress-strain in Horizontal *PZT* Patch for Vertical Dynamic Loading

In Fig. 3.1 Cantilever wall retaining granular backfill bounded by a horizontal *PZT* layer on the outer surface of the backfill. The PZT layer and granular backfill are assumed to be firmly bound together. *PZT* and wall retaining granular backfill models are linear and elastic. The material properties of the *PZT* and backfill are homogeneous and isotropic. The stress of individual *PZT* and granular fill layers is the product of strain and modulus of the material of each layer.

In pure bending, the normal strain $\in_n$ and normal stress σ_n in the x-direction can be expressed as,

$$\in_n = \frac{Z}{R} \tag{3.1}$$

$$\sigma_n = E \in_n \tag{3.2}$$

where 1/R is the radius of curvature due to bending, E is the modulus, and Z is the direction on Z- coordinate from the neutral surface.

Normal strain along the x-direction can be calculated as,

$$\in_n = \frac{Z}{R} = \frac{MZ}{EI} \tag{3.3}$$

For the *PZT* layer, the strain in the mid surface of the *PZT* is expressed as,

$$(\in_{PZT})_{avg} = -\frac{M(z_p - \bar{z})}{E_R I_R + E_p I_p} = \frac{M(\bar{z} - z_p)}{E_R(I_R + nI_p)} \tag{3.4}$$

By solving the above equation, the average strain in the *PZT* layer is expressed as,

$$(\in_{PZT})_{avg} = \frac{M}{bE_R h_R^2}\left[\frac{36(1+\mu)(1+\mu n)}{3\mu^5 n^3 + 6\mu^4 n^2 + 5\mu^3 n + \mu^2 n^2 + \mu^2 + 4\mu n + 2}\right] \tag{3.5}$$

From Eq 3.1 and Eq 3.5, the average stress in the *PZT* layer is analyzed as,

$$(\sigma_{PZT})_{avg} = \frac{36M}{b\, h_R^2}\left[\frac{n(1+\mu)(1+\mu n)}{3\mu^5 n^3+6\mu^4 n^2+5\mu^3 n+\mu^2 n^2+\mu^2+4\mu n+2}\right] \qquad (3.6)$$

where, thickness ratio (μ) is the ratio of the thickness of the *PZT* over wall retaining granular fill, and a modulus ratio (n) is the ratio of the modulus of the *PZT* over wall retaining granular fill respectively, that is,

modulus ratio of PZT over wall retaining granular fill $(n) = \frac{E_P}{E_R}$

The thickness ratio of PZT over wall retaining granular fill $(\mu) = \frac{h_P}{h_R}$

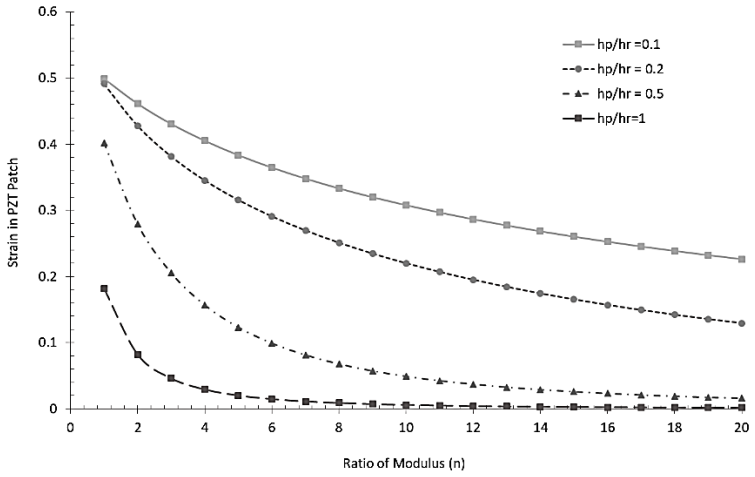

Fig. 3.2 The average strain in the *PZT* layer at various thickness ratios

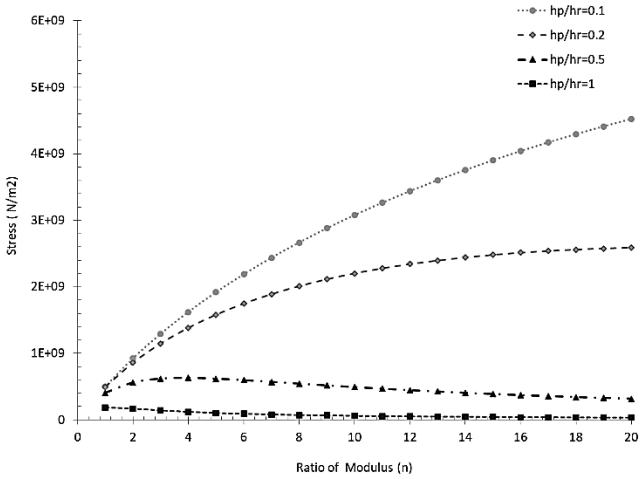

Fig. 3.3 The average stress in the *PZT* layer at various thickness ratios

These graphs indicate that the average strain in the *PZT* layer decreases when the ratio of modulus n increases. Average stress in the *PZT* layer increases when the ratio of modulus increases.

3.3.2 Stress-strain in Wall Retaining Granular Fill for Vertical Dynamic Loading

The stress-strain analysis of the confined granular fill is analyzed considering the effect of wall retaining granular fill on the backfill.

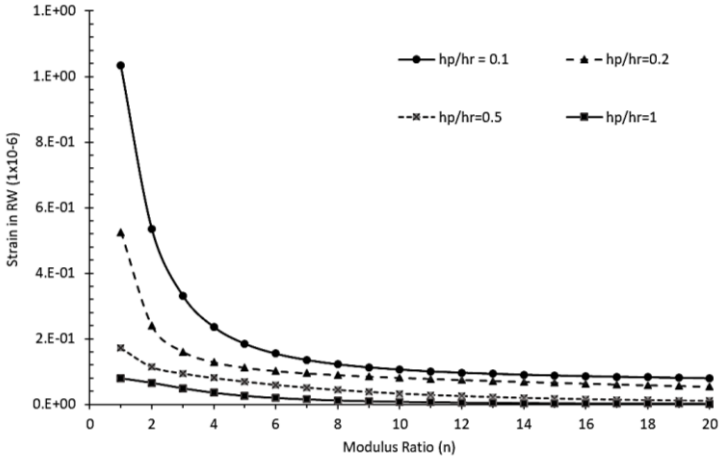

Fig. 3.4 The average strain in wall retaining granular fill at various thickness ratios

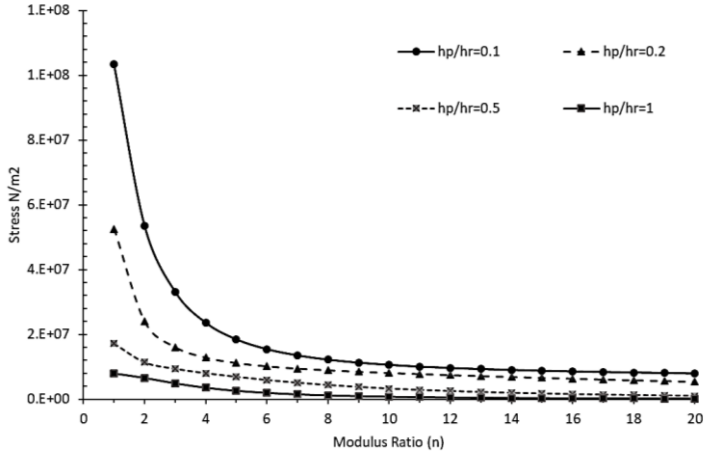

Fig. 3.5 The average stress in wall retaining granular fill at various thickness ratios

3.3.3 Stress-strain in Vertical *PZT* Patch for Horizontal Vibrations

A rigid retaining wall of height (h) has been considered. A *PZT* patch is provided between the retaining wall and granular backfill. Dynamic loading is applied in the horizontal direction normal to the *PZT* patch. The width of the retaining wall, *PZT* patch and backfill is b_R, b_P b_S respectively. It is assumed that the contact among the retaining wall, *PZT* patch and granular fill is perfect, and there is no shear moment or separation at the interface. The deformation of the retaining wall-*PZT* system is assumed to be elastic considering linear elasticity. Strain in the layer would depend on parameters such as frequency coefficient, elastic stiffness and location of the neutral surface of the retaining wall-*PZT* system.

Assume that the retaining wall-*PZT* system is under pure bending and zero displacement in the z-direction. The strain of the retaining wall composed of granular fill with *PZT* patch is expressed as,

$$(\varepsilon)_{avg} = \frac{M\left(\bar{X} - X\right)}{E_P I_P + E_R I_R + E_S I_S} \qquad (3.7)$$

where, $(\varepsilon)_{avg}$ represents the average strain. *M* is the bending moment of the retaining wall-*PZT* system. *X* is the distance from the neutral axis in the x-direction and $\bar{X}$ is the location of neutral surface of composite retaining wall. E_P, E_R and E_S is elastic modulus of the *PZT* patch, retaining wall and backfill, respectively. I_P, I_R and I_S is the moment of inertia about the centroid of the *PZT* patch, retaining wall and backfill, respectively.

For the composite structure with *PZT*, we define the ratio of the width of *PZT* and retaining wall (μ), ratio of width of retaining wall and *PZT* (a), ratio of modulus of *PZT* and modulus of backfill (n) and ratio of modulus of retaining wall and modulus of *PZT* (b).

$$\text{Modulus ratio of } PZT \text{ over backfill } (n) = \frac{E_P}{E_S}$$

$Width$ ratio of PZT over backfill $(\mu) = \frac{b_P}{b_S}$

Width ratio of retaining wall over PZT $(a) = \frac{b_R}{b_P}$

Modulus ratio of retaining wall over PZT $(b) = \frac{E_R}{E_P}$

The average strain for the vertically embedded *PZT* layer is expressed as,

$$(\varepsilon_p)_{avg} = \frac{36M}{E_s h b_s^2}\left[\frac{(3\mu+2-12a^2b\mu^2n)\left[24\mu n(a+b)+1\right]}{\left[3n\mu^3(1+ba^3)+1\right]\left[24\mu n(a+b)+1\right]^2+18\left(3\mu+2-12a^2b\mu^2n\right)\left[2\mu n(1+ab)+1\right]}\right] \quad (3.8)$$

The average strain for the backfill layer is expressed as,

$$(\varepsilon_s)_{avg} = \frac{-36M}{E_s h b_s^2}\left[\frac{\left[12\mu^2n(ab+1)\right]\left[\mu n(3ab-6a^2b-6ab)-2n(ab-1)\right]}{\left[3\mu^3n(1+ba^3)+1\right]\left[12\mu n(ab+1)\right]^2+18\mu^2\left[\mu n(3ab-6a^2b-6ab)-2n(ab-1)\right]^2\left[2\mu n(1+ab)+1\right]}\right] \quad (3.9)$$

The average stress for the horizontally embedded *PZT* layer is expressed as,

$$(\sigma_p)_{avg} = \frac{36nM}{h b_s^2}\left[\frac{(3\mu+2-12a^2b\mu^2n)\left[24\mu n(a+b)+1\right]}{\left[3n\mu^3(1+ba^3)+1\right]\left[24\mu n(a+b)+1\right]^2+18\left(3\mu+2-12a^2b\mu^2n\right)\left[2\mu n(1+ab)+1\right]}\right] \quad (3.10)$$

The average stress for the backfill layer is expressed as,

$$(\sigma_s)_{avg} = \frac{-36M}{h b_s^2}\left[\frac{\left[12\mu^2n(ab+1)\right]\left[\mu n(3ab-6a^2b-6ab)-2n(ab-1)\right]}{\left[3\mu^3n(1+ba^3)+1\right]\left[12\mu n(ab+1)\right]^2+18\mu^2\left[\mu n(3ab-6a^2b-6ab)-2n(ab-1)\right]^2\left[2\mu n(1+ab)+1\right]}\right] \quad (3.11)$$

The material used as backfill for analysis is well-graded dense sand. The elastic modulus of dense sand is taken as 250 MPa.

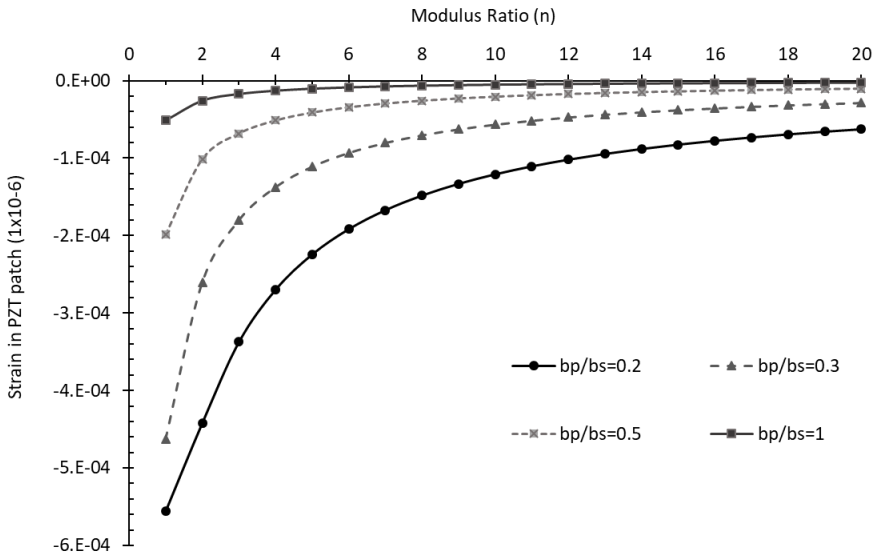

Fig. 3.6 Variation of average strain with modulus ratio (n) in *PZT* layer for horizontal dynamic loading

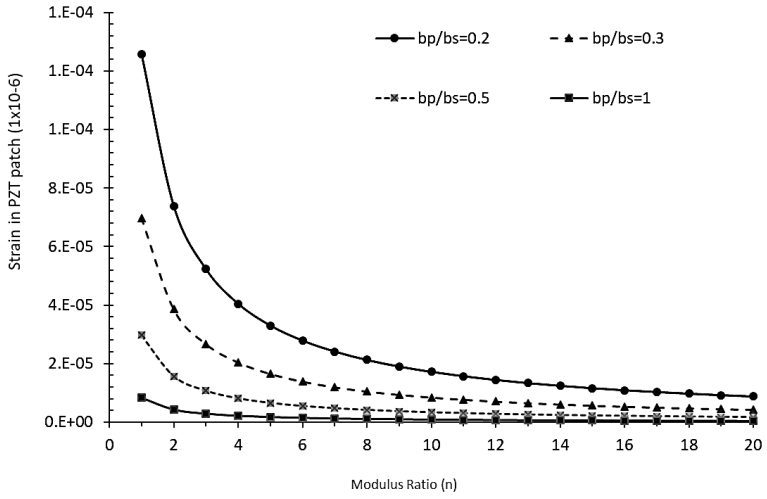

Fig. 3.7 Variation of average strain with modulus ratio (n) for backfill layer for horizontal dynamic loading

3.4 Dynamic Response of Horizontal and Vertical Vibration using *PZT* Patches

The structures are regarded as a dynamic system whose response variables such as displacement, velocity and acceleration are functions of time and in which some mechanical properties, typically stiffness ratio and the mass ratio may be adjusted to minimize the dynamic effects of loads under an acceptable level (Yao, 1972). Vibration analysis aims to determine

the mechanical energy induced by the dynamic load. The base motion was controlled utilizing an electrodynamics shaker, while a piezoelectric patch (*PZT*) actuator was bonded on the surface of a flexible beam to suppress residual arm vibration. This technique was also used to analyze the stress-strain behaviour of the composite beam (Kerboua et al., 2014) and retaining wall (Kumari and Trivedi, 2018) by considering the thickness of the *PZT* patch and elastic modulus of the material to control the vibration. The *PZT* patch is utilized to analyze the displacement in the retaining wall's horizontal and vertical directions for dynamic response analysis of structure.

In this chapter, a flexible wall retaining granular fill has been considered to have roller support at the bottom and bounded with the *PZT* patch on the outer surface of the backfill. The thickness of the backfill is h_b and length L, while the *PZT* patch possesses thickness and length h_P and L, respectively. The *PZT* patch and backfill are assumed to have the same width (b). It is assumed that *PZT* and granular material are in perfect contact and there is no shear movement or separation at the interface. The present model maintains the stress continuity of the soil-wall system. The soil overlaying with *PZT* and wall interaction is considered to examine the dynamic response of the wall.

3.5 Soil- wall System with *PZT* Patches

The soil-wall system is subjected to transverse excitation. The soil-wall system is overlain on a rigid base with a depth of H from the *PZT* surface. The wall of length L, thickness t_w, the thickness of *PZT* h_P from the top and thickness of granular fill H_S. Young's modulus of *PZT* and wall is E_P and E_R, respectively. The vibration induced in a soil-wall system due to transverse excitation is analyzed using the stiffness of the material. The stiffness tends to shift the resonance frequency of the structure beyond the frequency band of excitation. The natural

frequency of the excitation is also essential to the horizontal and vertical displacement of the flexible retaining system.

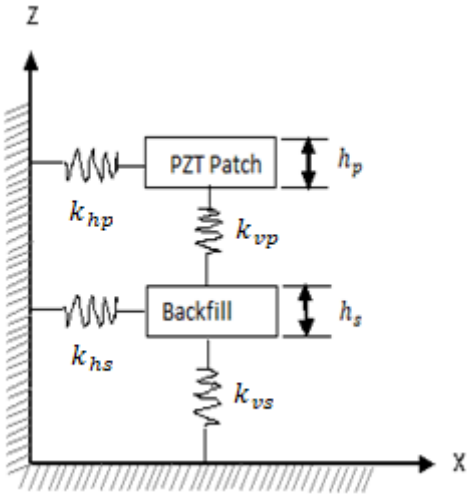

Fig. 3.8 Displacement profile represented in the form of the spring-mass system

3.6 Dynamic Response of the Soil-Wall System

3.6.1 Horizontal Displacement

The spring constant for *PZT* and granular fill is k_1 and k_2 respectively. This spring-mass system is subjected to a force *Fsin (ωt+β)* in the horizontal direction.

By solving the equation of motion of the soil-wall system and neglecting the terms of damping, and considering the force in the phase (i.e., β=0), the displacement in x- direction is represented as,

$$u_x = \frac{F/k_x}{1-\frac{\omega^2}{\omega_n^2}}\left(\sin\omega t - \frac{\omega}{\omega_n}\sin\omega_n t\right) \qquad (3.12)$$

where, $k_{hp} + k_{hs} = k_x$, and and $\omega_n = \sqrt{\frac{k_Z}{m}}$

Where, the total mass (m) is expressed as,

$$m = \frac{\gamma H^2}{2\tan\alpha} + \gamma B h_p \qquad (3.13)$$

3.6.2 Vertical Displacement

By solving the equation of motion of the soil-wall system and neglecting the terms of damping, and considering the force in the phase (i.e., β=0), the displacement in the z-direction is represented as,

$$u_Z = \frac{F/k_Z}{1-\frac{\omega^2}{\omega_n^2}}\left(\sin\omega t - \frac{\omega}{\omega_n}\sin\omega_n t\right) \qquad (3.14)$$

where, $k_Z = \dfrac{k_{vp}k_{vs}}{k_{vp}+k_{vs}}$

Chapter 4

Factors Influencing Piezoelectric Response of Embedded *PZT* Patch

This chapter is based on the article published in Advances in Materials Science and Engineering as listed in section 1.8. The details are presented here with some changes in the layout to maintain consistency in the presentation throughout the thesis.

4.1 Introduction

The dynamically loaded geo-structures mainly consisting of transportation infrastructures, find a unique application for energy harvesting. Due to sensor technology developments, *PZT* has found profound utility in structural health monitoring. This energy can be harvested using a suitable mechanism for various micro and macro engineering operations, including electrical devices and transportation as a renewable energy system (García-Olivares et al. 2018). The piezoelectric material provides higher energy density and flexibility integrated into a system than the electromagnetic and electrostatic units (Anton and Sodano 2007; Singh et al. 2022). Many researchers (Divsholi and Yang 2010; Xu et al. 2013; Xu et al. 2015) have analysed the effectiveness of embedded *PZT* (Lead Zirconate Titanate) patches for energy harvesting and structural health monitoring.

This study provides a parametric investigation of the factors influencing the piezoelectric voltage generation considering the installation position of the *PZT* patch, geometric and mechanical properties of the embedded *PZT* patch in confined granular fill. The confined granular fill is contained by the pavement and the retaining structure. The confined granular fill experiences vibrations due to dynamic loads. The strain patch absorbs the PZT fluctuation, which polarizes and induces a voltage. This deformation per unit length is analysed by the stress-strain response of the confined granular fill due to the ambient vibration. The deformation of the *PZT* patch is used to calculate the charge density and voltage output. The

model that consists of confined granular fill with embedded *PZT* patches is analysed theoretically. The electromechanical process is used to convert the mechanical energy into electrical energy. The charge density and voltage output from the *PZT* patch is discussed with a focus on the influence of the embedded position, piezoelectric properties, geometric properties of the *PZT* patch, and confined granular fill.

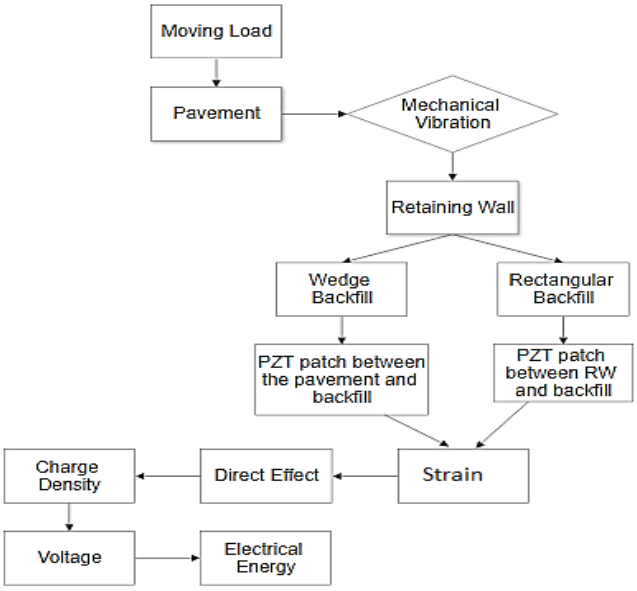

Fig. 4.1 Flow chart for electromechanical energy output from mechanical vibrations

It shows the parametric investigation of the factors influencing the piezoelectric voltage generation considering the installation position of the *PZT* patch and the geometric and mechanical properties of the embedded *PZT* patch in confined granular fill. The confined granular fill is contained by the pavement and the wall retaining granular fill. The confined granular fill experiences vibrations due to dynamic loads. The strain fluctuations are captured by the *PZT* patch, which is polarized to induce a voltage. This deformation per unit length is related to the stress-strain response of the confined granular fill due to the ambient vibration. The deformation of the *PZT* patch is used to calculate the charge density and voltage output.

4.2 Engineering Properties of *PZT* Patches

When piezoelectric materials are subjected to mechanical stress, electrical energy generated in proportion to that stress is known as the direct piezoelectric effect. The direct effect occurs through the compression of piezoelectric material, as shown in Fig. 13. D_3 is the electric displacement on the *PZT* patch, E_3 is the electric field in direction-3, d_{31} is the piezoelectric strain coefficient in mode -31, ε_{33}^{T} represents the permittivity of the material in the direction-33 under conditions of constant mechanical stress ($\varepsilon_{33}^{T=0}$ corresponds to free permittivity) and σ_{PZT} is stress in the *PZT* layer.

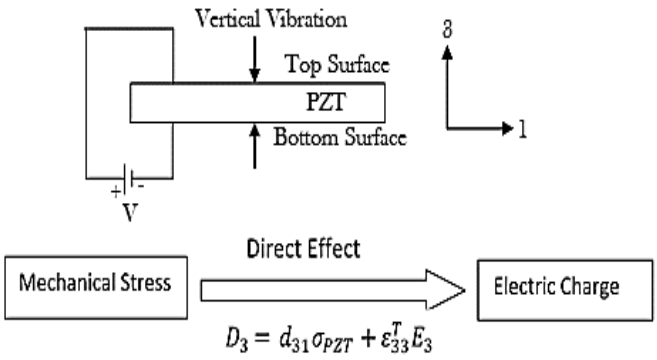

Fig. 4.2 Flow chart for the generation of electric charge due to mechanical vibrations

The parameters influencing the voltage output from the *PZT* patches are relative permittivity $\left(\varepsilon_{33}^{T}/\varepsilon_{o}\right)$ (here ε_0 refers to the absolute permittivity of the vacuum), piezoelectric strain constant (d), polarization ratio $\left(d_{31}/\varepsilon_{33}\right)$ and piezoelectric voltage coefficient (g). The charge density of the *PZT* patch is the most important consideration when choosing a piezoelectric material for energy harvesting. The product of the effective piezoelectric strain constant (d) and the effective piezoelectric voltage constant (g) determine the magnitude of the charge density (Islam and Priya, 2006).

Table 4.1 Engineering properties of piezoelectric patches

Engineering Properties	Symbol	Hard Patch; *PZT*-141	Semi-Hard; *PZT*-155	Soft Patch; *PZT*-151
Density (kg/m$^{3)}$	ρ	7800	7800	7800
Modulus of *PZT* Patch (GPa)	E_P	81	63	60
Relative Permittivity [a]	$\frac{\varepsilon_{33}^T}{\varepsilon_o}$	1250	1450	2400
Piezoelectric strain constant [a] (C/N)	d_{31} d_{33}	-140×10^{-12} 310×10^{-12}	-165×10^{-12} 360×10^{-12}	-210×10^{-12} 500×10^{-12}
Piezoelectric voltage coefficient [a] (Vm/N)	g_{31} g_{33}	-13.1×10^{-3} 29×10^{-3}	12.9×10^{-3} 27×10^{-3}	-11.5×10^{-3} 22×10^{-3}
Polarization ratio [b]	$\frac{d_{31}}{\varepsilon_{33}}$	0.112	0.114	0.087

[a] *Physik Instrumente GmbH (2011),* [b] *Present work*

The *PZT* material considerations are classified as hard, semi-hard, and soft *PZT* patches, as shown in Table 4.1. The piezoelectric material considerations for engineering applications include piezoelectric strain constant, piezoelectric voltage constant, and mechanical quality factor (*Q).* The relative permittivity of the selected *PZT* patches (Table 4.1) was 1250, 1450, and 2400, while the polarization ratio was 0.112, 0.114, and 0.087, respectively. The polarization ratio is the piezoelectric strain constant and relative permittivity ratio.

4.3 Stress-strain Behaviour of *PZT* Patches

The stress-strain behaviour of the *PZT* patch has been considered for horizontal and vertical alignments. A *PZT* patch is horizontally and vertically embedded in the confined granular fill. It has been assumed that the neutral plane of the *PZT* patch doesn't coincide with the geometrical centre of the fill. There is negligible shear movement or separation among the retaining structure, *PZT* patch, and granular fill. The wall retaining granular fill is considered

flexible and elastically constrained at the base. The shape of the useful part of the granular fill is considered a triangular wedge. The vibrating system consists of a wall of height *H*, length *L* (such that *L=1*), and backfill of thickness h_R. The thickness of the *PZT* patch is h_p. As a result of the vibration, the stresses are generated in the pavement, granular fill and *PZT* patch.

The deformation in the horizontally embedded *PZT* patch is a function of *PZT* material properties, bending moment, the width of backfill, modulus ratio, and thickness ratio. The strain in the horizontally embedded *PZT* patch is expressed as,

$$\varepsilon_{HE} = f(M, b_S, E_S, h_R, \mu, n) = \frac{36M}{b_S E_s h_R^2}\left[\frac{(1+\mu)(1+\mu n)}{3\mu^5 n^3 + 6\mu^4 n^2 + 5\mu^3 n + \mu^2 n^2 + \mu^2 + 4\mu n + 2}\right] \quad (4.1)$$

The stress in the horizontally embedded patch is a function of strain and modulus of the *PZT* and is expressed as,

$$\sigma_{HE} = \varepsilon_{HE} * E_P = \frac{36M}{b_S h_R^2}\left[\frac{n(1+\mu)(1+\mu n)}{3\mu^5 n^3 + 6\mu^4 n^2 + 5\mu^3 n + \mu^2 n^2 + \mu^2 + 4\mu n + 2}\right] \quad (4.2)$$

where, ε_{HE} and σ_{HE} are the strain and the stress in a horizontally embedded *PZT* patch. E_S and E_P are Young's modulus of backfill and *PZT* patch, respectively. μ is the ratio of the thickness of the *PZT* patch to the backfill ($\frac{h_P}{h_R}$), and *n* is the ratio of the modulus of the *PZT* patch to the backfill ($\frac{E_P}{E_R}$), M is the bending moment *PZT* patch.

The strain in the vertically embedded *PZT* patch is the function of bending moment, the height of the retaining structure, modulus ratio, height of the backfill, and thickness ratio and is expressed as,

Similarly, the stress for vertically embedded *PZT* patch between the granular fill and retaining wall is expressed as,

$$\varepsilon_{VE} = f(M,H,h_S,a,b,\mu,n) = \frac{36M}{E_s H h_s^2}\left[\frac{(3\mu+2-12a^2b\mu^2n)\left[24\mu n(a+b)+1\right]}{\left[3n\mu^3(1+ba^3)+1\right]\left[24\mu n(a+b)+1\right]^2+18\left(3\mu+2-12a^2b\mu^2n\right)\left[2\mu n(1+ab)+1\right]}\right] \quad (4.3)$$

$$\sigma_{VE} = \varepsilon_{VE} * E_P = \frac{36nM}{Hh_s^2}\left[\frac{(3\mu+2-12a^2b\mu^2n)\left[24\mu n(a+b)+1\right]}{\left[3n\mu^3(1+ba^3)+1\right]\left[24\mu n(a+b)+1\right]^2+18\left(3\mu+2-12a^2b\mu^2n\right)\left[2\mu n(1+ab)+1\right]}\right] \quad (4.4)$$

where, ε_{VE} and σ_{VE} are the strain and stress in vertically embedded *PZT* patch, *a* is the thickness ratio of retaining wall and *PZT* patch ($\frac{h_w}{h_P}$), and *b* is the modulus ratio of retaining wall and *PZT* patch ($\frac{E_w}{E_P}$).

4.4 Evaluation of Charge Density

4.4.1 Horizontally and Vertically Embedded *PZT* Patch

The charge density equations for the hard (H), semi-hard (SH), and soft (S) *PZT* patches embedded horizontally have been derived from the stress-strain relationship of the *PZT* patch subject to vibrations in the confined granular fill. A single layer of *PZT* patch, horizontally embedded between the pavement and the granular fill. The deflection induces curvature in the triangular wedge at an arbitrary point on the neutral axis due to bending. The power output and the dynamic response of the piezoelectric system entirely depend on the coupling mode of the *PZT* patch.

The charge density equations for the hard, semi-hard, and soft *PZT* patches embedded horizontally have been derived from the stress-strain relationship of the *PZT* patch subject to vibrations in the confined granular fill. A horizontal PZT patch layer is embedded between the pavement and the granular fill. The deflection induces curvature in the triangular wedge at an arbitrary point on the neutral axis due to bending. The power output and the dynamic response of the piezoelectric system entirely depend on the coupling mode of the *PZT* patch. The

researchers (Park, 2008; Mateu, 2005) have identified that the natural way of excitation of retaining structure is in d_{31} mode. Therefore, the d_{31} mode has been chosen in the present work for analysis. For the so-configured system, the tensorial representation of the piezoelectric constitutive equation (IEEE, 1988) gives the electric displacement as,

$$D_3 = d_{31}\sigma_{PZT} + \varepsilon_{33}^{T} E_3 \qquad (4.5)$$

The stress generated in the *PZT* patch due to the dynamic loads on the confined granular fill changes the polarization and the displacement on the upper and lower surface of the *PZT* patch. As there is no external electric source ($E_3 = 0$), the electric displacement in the *PZT* patch is expressed as,

$$D_3 = d_{31}\sigma_{PZT} \qquad (4.6)$$

The charge density function at the top and bottom surface of the horizontally embedded *PZT* patch is expressed as,

$$\rho_{THE} = D_3\left(Z, h_p + \frac{h_R}{3}\right) \qquad (4.7)$$

$$\rho_{BHE} = D_3\left(Z, h_P\right) \qquad (4.8)$$

where, ρ_{THE} and ρ_{BHE} are charge density functions at the top and bottom surface of the horizontally embedded *PZT* patch, respectively. D_3 is electric displacement according to the piezoelectric coupling constitutive equation. Z is the thickness direction coordinate from the neutral plane.

From Eq. 4.10 and 4.12, the charge density is expressed as,

The negative sign represents the opposite charge of the top surface, while Q_{THE} and Q_{BHE} are the charge density at the top and bottom surface of the horizontally embedded *PZT* patch, respectively.

$$Q_{THE} = d_{31} \int_0^{\left(h_p + \frac{h_R}{3}\right)} \sigma_B dz \qquad (4.9)$$

$$Q_{THE} = \frac{12 d_{31} M}{b h_R} \left[\frac{n(1+\mu)(1+\mu n)(3\mu+1)}{3\mu^5 n^3 + 6\mu^4 n^2 + 5\mu^3 n + \mu^2 n^2 + \mu^2 + 4\mu n + 2} \right] \qquad (4.10)$$

$$Q_{BHE} = -d_{31} \int_0^{(h_p)} \sigma_B dz \qquad (4.11)$$

$$Q_{BHE} = \frac{-12 d_{31} M}{b h_R} \left[\frac{n\mu(1+\mu)(1+\mu n)}{3\mu^5 n^3 + 6\mu^4 n^2 + 5\mu^3 n + \mu^2 n^2 + \mu^2 + 4\mu n + 2} \right] \qquad (4.12)$$

4.5 Charge Density for Vertically Embedded *PZT* Patch

The charge density determines the dipole mobility of the charges on the *PZT* surface and affects the efficiency of power generation. The charge density function at the top and bottom surface of the vertically embedded *PZT* patch is expressed as,

$$\rho_{TVE} = D_3\left(Z, h_p + e\right) \qquad (4.13)$$

where, *e* is the distance between the bottom surface of *PZT* and the centre of gravity of the granular backfill and is expressed as,

$$e = \frac{h_P \left[6a + 1 - 6a^2 \right]}{18a + 12} \qquad (4.14)$$

$$\rho_{BVE} = D_3\left(Z, h_p\right) \qquad (4.15)$$

ρ_{TVE} and ρ_{BVE} are the charge density function at the top and bottom surface of the vertically embedded *PZT* patch in the confined granular fill, h_p is the thickness of the *PZT* patch, *a* is the thickness ratio of the retaining wall and the *PZT* patch ($\frac{h_w}{h_P}$), D_3 is electric displacement according to the constitutive equation of the piezoelectric coupling, *Z* is the thickness direction coordinate from the neutral plane, *e* is the distance between the neutral plane and the bottom surface of the *PZT* patch as shown in Fig. 4.5(b).

The charge density (Eq. 16 and 17) is expressed as,

$$Q_{TVE} = d_{31} \int_{0}^{(h_p+e)} \sigma_E dz \tag{4.16}$$

$$Q_{TVE} = \frac{36 d_{31} nM}{hah_S} \left[\frac{(3\mu + 2 - 12a^2 b\mu^2 n)(24\mu n(a+b)+1)(6a+1-6a^2)}{(18a+12)[(3n\mu^3(1+ba^3)+1)(24\mu n(a+b)+1)^2 + 18(3\mu+2-12a^2 b\mu^2 n)(2\mu a} \right.$$

(4.17)

$$Q_{BVE} = -d_{31} \int_{0}^{(e)} \sigma_E dz \tag{4.18}$$

$$Q_{BVE} = \frac{-36 d_{31} nM}{hah_S} \left[\frac{(3\mu + 2 - 12a^2 b\mu^2 n)(24\mu n(a+b)+1)(6a^2+12a+11)}{(18a+12)[(3n\mu^3(1+ba^3)+1)(24\mu n(a+b)+1)^2 + 18(3\mu+2-12a^2 b\mu^2 n)(2\mu a(1} \right.$$

(4.19)

Q_{TVE}, and Q_{BVE} are the generated charge density at the top and bottom surface of the vertically embedded *PZT* patch, respectively.

The charge density function at the top and bottom surface of the horizontally embedded *PZT* patch is expressed as,

$$Q_{THE} = \frac{12 d_{31} M}{bh_R} \left[\frac{n(1+\mu)(1+\mu n)(3\mu+1)}{3\mu^5 n^3 + 6\mu^4 n^2 + 5\mu^3 n + \mu^2 n^2 + \mu^2 + 4\mu n + 2} \right] \tag{4.20}$$

$$Q_{BHE} = \frac{-12 d_{31} M}{bh_R} \left[\frac{n\mu(1+\mu)(1+\mu n)}{3\mu^5 n^3 + 6\mu^4 n^2 + 5\mu^3 n + \mu^2 n^2 + \mu^2 + 4\mu n + 2} \right] \tag{4.21}$$

The negative sign represents the opposite charge of the top surface, while Q_{THE} and Q_{BHE} are the charge density at the top and bottom surface of the horizontally embedded *PZT* patch, respectively.

The charge density at the top surface of the vertically embedded *PZT* patch is expressed as,

$$Q_{TVE} = \frac{36 d_{31} nM}{hah_s} \left[\frac{(3\mu + 2 - 12a^2 b\mu^2 n)(24\mu n(a+b)+1)(6a+1-6a^2)}{(18a+12)\left[(3n\mu^2(1+ba^3)+1)(24\mu n(a+b)+1)^2 + 18(3\mu+2-12a^2 b\mu^2 n)(2\mu a(1+ab)+1)\right]} \right]$$

(4.22)

The charge density at the bottom surface of the vertically embedded *PZT* patch is expressed as,

$$Q_{BVE} = \frac{-36d_{31}nM}{hah_s}\left[\frac{(3\mu+2-12a^2b\mu^2n)(24\mu n(a+b)+1)(6a^2+12a+11)}{(18a+12)\left[(3n\mu^2(1+ba^3)+1)(24\mu n(a+b)+1)^2+18(3\mu+2-12a^2b\mu^2n)(2\mu a(1+ab)+1)\right]}\right]$$

(4.23)

Q_{TVE}, and Q_{BVE} are the generated charge density at the top and bottom surfaces of the vertically embedded *PZT* patch, respectively.

4.6 Voltage Output from Horizontally and Vertically Embedded *PZT* Patch

Due to the phase difference, the charge developed at the opposite side of the *PZT* patch is collected by a separate electrode to prevent charge cancellation due to the phase difference in the electric displacement.

Since the charge quantity of the top and bottom surfaces are not the same, the voltage between the two poles is expressed as,

$$V = \int_e^{(h_P+e)} E(x,z)dz \qquad (4.24)$$

$$E = \frac{d_{31}\sigma_P}{\varepsilon_{33}} \qquad (4.25)$$

where, *V* is the voltage between the top and bottom surface of the *PZT* patch due to vibration of the system, *E* is the equivalent electric field intensity, σ_P is stress in the *PZT* patch, $\frac{\varepsilon_{33}^T}{\varepsilon_o}$ is relative permittivity. For horizontally embedded *PZT* patch, the voltage output between the top and bottom surface of the *PZT* patch is expressed as,

$$V_{HE} = \frac{h_R^2 d_{31} E_P \mu(3\mu+2)}{12\varepsilon_{33}\rho} \qquad (4.26)$$

$$V_{HE} = \frac{3Md_{31}}{b\varepsilon_{33}}\left[\frac{n\mu(1+\mu)(1+\mu n)(2+3\mu)}{3\mu^5n^3+6\mu^4n^2+5\mu^3n+\mu^2n^2+\mu^2+4\mu n+2}\right] \qquad (4.27)$$

where, V_{HE} is the voltage output for a horizontally embedded *PZT* patch in confined granular fill. d_{31} is the piezoelectric strain constant for 31 mode. E_P is the elastic modulus of the *PZT*

patch. Similarly, for vertically embedded *PZT* patch, the voltage output between the top and bottom surface of the *PZT* patch is expressed as,

$$V_{VE} = \frac{h_P^2 d_{31} \varepsilon_o E_P \mu^2 (-6a^2 + 15a + 13)}{2\varepsilon_{33} \rho (18a + 12)} \qquad (4.28)$$

$$V_{VE} = \frac{18n\varepsilon_o M d_{31}}{H\varepsilon_{33}} \left[\frac{\mu^2 (3\mu + 2 - 12a^2 b\mu^2 n)(24\mu n(a+b) + 1)(-6a^2 + 15a + 13)}{18a + 12\left[(3n\mu^3 (1 + ba^3) + 1)(24\mu n(a+b) + 1)^2 + 18(3\mu + 2 - 12a^2 b\mu^2 n)(2\mu n(1+ab) + 1) \right]} \right] \qquad (4.29)$$

where, V_{VE} is the voltage output of a vertically embedded *PZT* patch. *H* is the height of the retaining structure. *a* and *b* denote the thickness ratio of retaining wall with *PZT* patch and the modulus ratio of retaining wall with *PZT* patch, respectively.

Due to the phase difference, the charge developed at the opposite side of the *PZT* patch is collected by a separate electrode to prevent charge cancellation due to the phase difference in the electric displacement.

4.7 Discussion on Factors Influencing Piezoelectric Response of Embedded *PZT* Patch

This section provides the stress response results on power generation from ambient vibration in retaining the structure of height *(H)* with horizontally and vertically embedded *PZT* patches. The charge density and voltage output are obtained, which are significantly affected by the stress state of the *PZT* patch. The stress-strain response of horizontally and vertically embedded *PZT* patches is analysed using Eq. 4.1-4.4. The effects of stiffness, polarization per unit permittivity and geometric properties of the *PZT* patch have been obtained by Eq. 4.5-4.29. It is considered difficult to embed the *PZT* on the upper surface of the pavement (environmental, abrasion, and iteration effects). Therefore, it is recommended to embed the *PZT* at depth (d). Accordingly, the stiffness of the base course layer has been considered as 1-4 *GPa* (Zhao et al., 2012). The resilient modulus of hardened concrete is reported in the range of 10-30 *GPa*

while that of aggregate is between 45-85 GPa. Hence, the range of values (1-5 *GPa*), which are well below the hardened concrete is used in this study.

The strain on the *PZT* patch is evaluated for varying thicknesses of the granular backfill. The comparative analysis is shown for varied piezoelectric materials, namely hard *(H),* semi-hard *(SH),* and soft *(S)* patches. The most commonly used parameters of the *PZT* patches namely the relative permittivity ($\frac{\varepsilon_{33}^{T}}{\varepsilon_{o}}$), piezoelectric strain constant (*d*), piezoelectric voltage coefficient (*g*), and polarization ratio are considered as mentioned in Table 4.1. The modulus of the *PZT* material varies with the temperature and thickness of the material. The researchers (Amini et al., 2017; Chopra, 2002) suggested that piezoelectric material has a stiffness range of 50-90 GPa. Therefore, to analyse the effect of the modulus ratio, the modulus of the hard, semi-hard and soft *PZT* patch has been taken as 81, 63 and 60 GPa, respectively. The charge density and voltage output have been analysed for hard, semi-hard, and soft *PZT* patches.

4.7.1 Effect of Stiffness of Confined Granular Fill and *PZT* Patches

The stress response for the vertically embedded *PZT* patch for thickness ratio is in the range of $0.01 \leq \mu \leq 0.20$. The negative values show the change in the nature of the stress. The change in sign indicates the compression and tension response of the stress. When a thin *PZT* patch is embedded vertically, the stress shows an opposite trend. It shows that the thickness of the surrounded granular fill affects the average stress in the *PZT* patch. The trend is due to the distance change between the centroid of the *PZT* patch and the neutral surface. When the thickness ratio is reduced to 0.01, it has been observed that the thickness and material of the wall also affect the strain and stress behaviour of the confined granular fill.

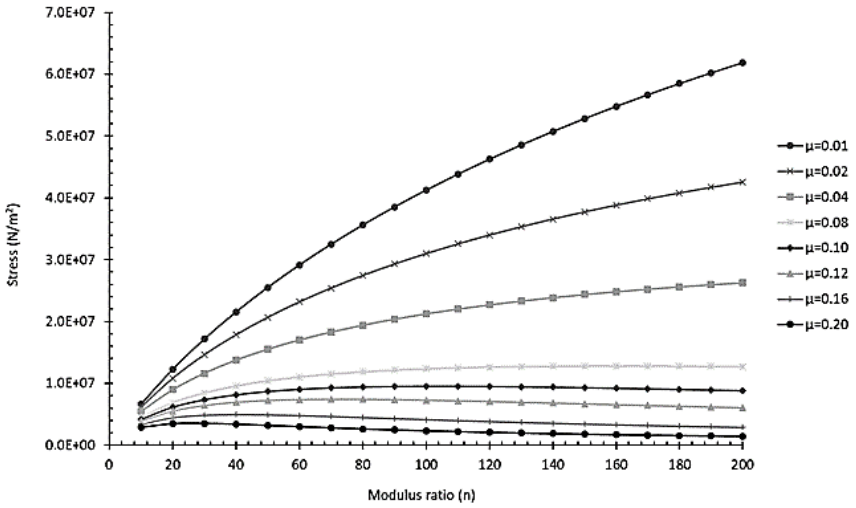

Fig. 4.3 Stress variation with modulus ratio for horizontally embedded *PZT* patch

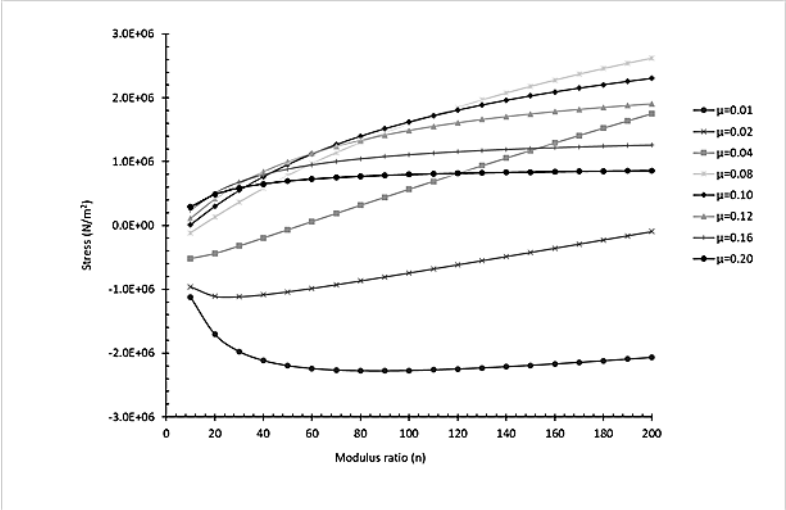

Fig. 4.4 Stress variation with modulus ratio for vertically embedded *PZT* patch

From Eq. 4.16, it is observed that charge density is directly proportional to the stress. Thus, the phenomenon indicates that the thickness of the retaining structure is a vital parameter for voltage output. Similarly, Fig. 4.4 shows the stress response for the vertically embedded *PZT* patch for a thickness ratio of $0.01 \leq \mu \leq 0.20$. The negative values show the change in the nature of the stress. The change in sign indicates the compression and tension response of the stress. When a thin *PZT* patch is embedded vertically, the stress shows the opposite trend. It shows that the thickness of the surrounded granular fill affects the average stress in the *PZT* patch. This curve trend owes to the change in the distance between the centroid of the *PZT* patch and

the neutral surface. Suppose the thickness ratio is reduced to 0.01. In that case, the maximum stress in the horizontally embedded *PZT* patch is more than five times higher than the vertically embedded *PZT* patch. It has been observed that the thickness and material of the wall also affect the strain and stress behaviour of the confined granular fill (Eq. 4.4).

4.7.2 Charge Density on Hard, Semi-hard, and Soft *PZT* Patches

A comparative study is presented for the hard (*H*), semi-hard (*SH*), and soft (*S*) *PZT* patches to capture the effect of geometric and mechanical parameters on the charge density on the *PZT* patch. The dominant parameters for the analysis are the installation position of the *PZT* patch, the thickness, and the modulus of the backfill material. The engineering properties of the *PZT* patch are shown in Table 4.1. As a result of the embedment of the *PZT* patch between the pavement and the granular material, the charge is induced on the top and bottom surfaces of the *PZT* patch. The difference between the positive and negative charges is proportional to the energy produced. The vibration in the backfill material deforms the horizontal embedded *PZT* patch. The piezoelectric phenomenon generates charge density on the surface of the *PZT* patch. Figs. 4.5-4.16 shows the charge density variation for the thickness ratios (μ) in the range of 0.10-0.20.

Table 4.2 Charge density for confined granular fill with *PZT* patches

Alignment of *PZT* patch	Maximum charge density at the top surface (Coulombs/m^2)						Maximum charge density at the bottom surface (Coulombs/m^2)					
	H	SH	S	H	SH	S	H	SH	S	H	SH	S
	$0.10 \leq \mu \leq 0.20$			$0.01 \leq \mu \leq 0.08$			$0.10 \leq \mu \leq 0.20$			$0.01 \leq \mu \leq 0.08$		
Horizontal	-26	-256	-5	-12	-15	-20	0	0	0	0	0	0
PZT	0	0	0	0	0	0	+1080	+1300	+1680	+1200	+1480	+1700
Vertical	-3	-30	-40	-104	-125	-166	0	0	0	+280	-100	+480
PZT	0	0	0	+25	+30	+38	+100	+150	+200	-100	+360	-160

Due to a small polarization ratio (0.114), the lowest charge is generated on the hard *PZT* patch. The maximum charge is generated on the semi-hard (SH) patch. Therefore a semi-hard *PZT* patch is recommended as an effective piezoelectric material. The results also indicate that the energy efficiency of the output voltage is low for the loose granular fills.

For the vertically embedded *PZT* patch, the maximum charge is generated on the soft *PZT* patch. For the thickness ratio (μ) in the range of 0.10-0.20, the results show that the total charge induced on the horizontally embedded *PZT* patch is higher than the vertically embedded patch. It indicates that the geometric parameters, modulus of granular fill and wall significantly affect the charge density on the top and the bottom surface of the *PZT* patch.

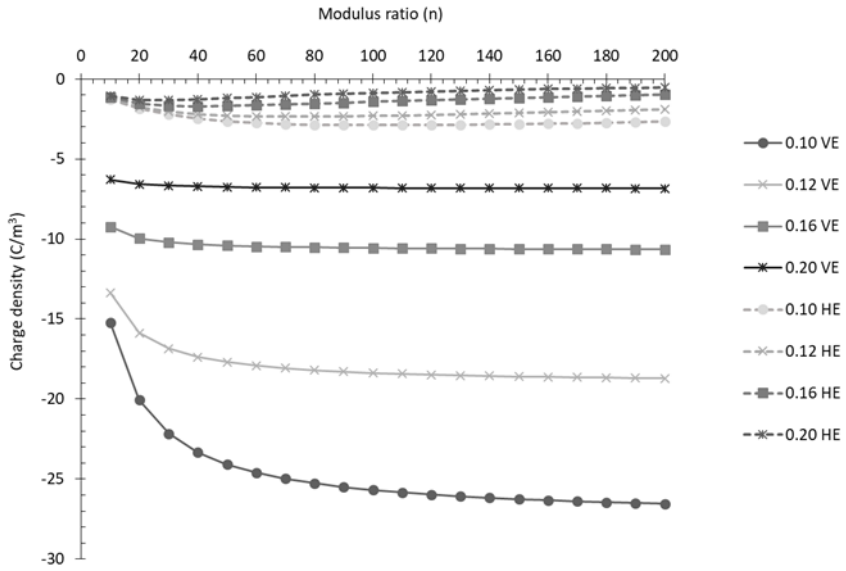

Fig. 4.5 Charge density computed for retaining structure of the top surface of the horizontally and vertically embedded hard *PZT* patch in the confined granular fill

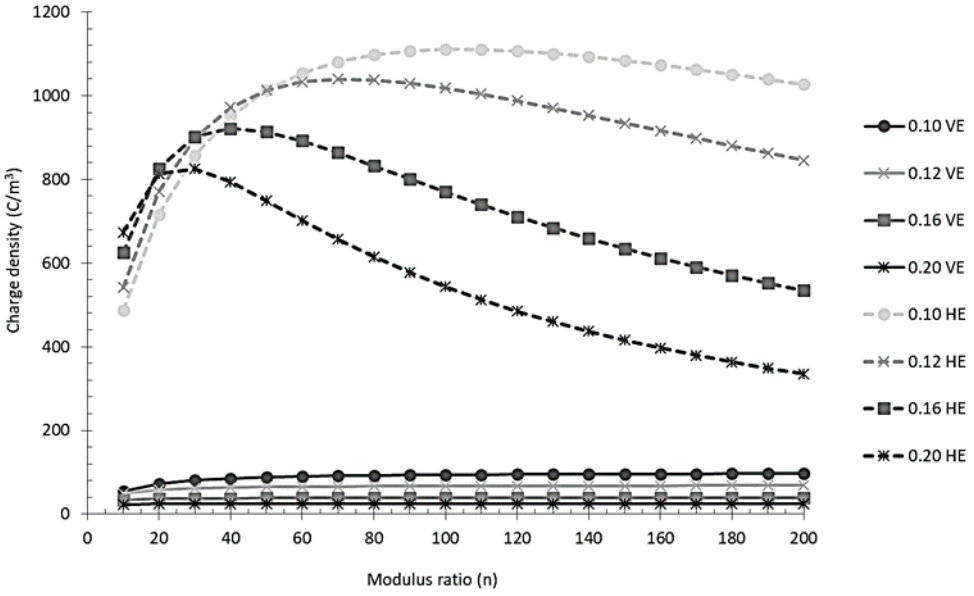

Fig. 4.6 Charge density computed for retaining structure of unit width, piezoelectric strain, modulus ratio, and thickness ratio on the bottom surface of the horizontally and vertically embedded hard *PZT* patch in the confined granular fill

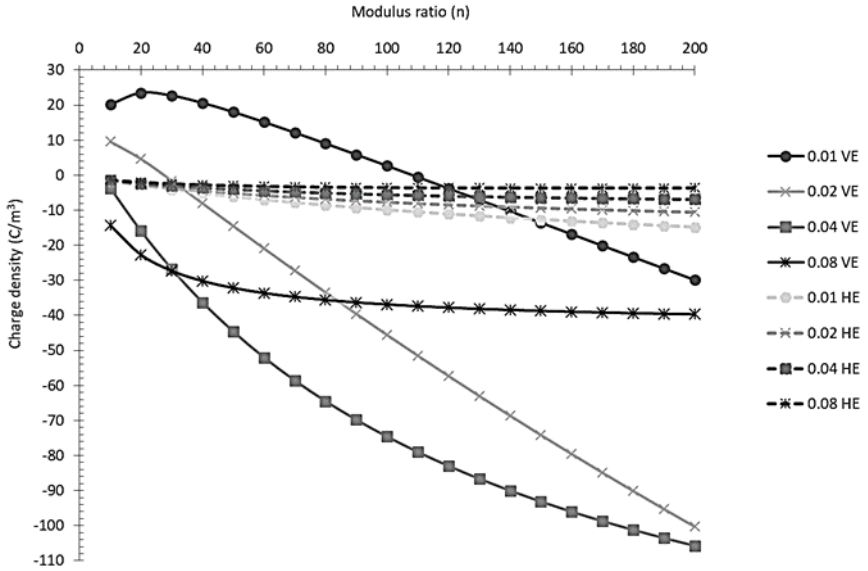

Fig. 4.7 Charge density computed for retaining structure of unit width, piezoelectric strain, modulus ratio and thickness ratio on the top surface of the horizontally embedded and from vertically embedded hard *PZT* patch in the confined granular fill

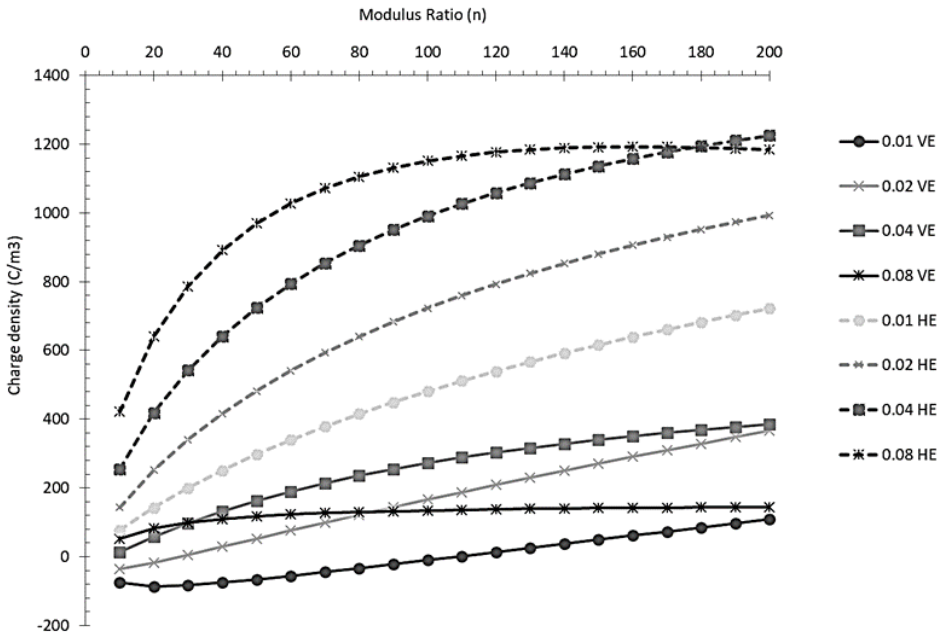

Fig. 4.8 Charge density computed for retaining structure of unit width, piezoelectric strain, modulus ratio, and thickness ratio on the bottom surface of the horizontally and vertically embedded hard *PZT* patch in the confined granular fill

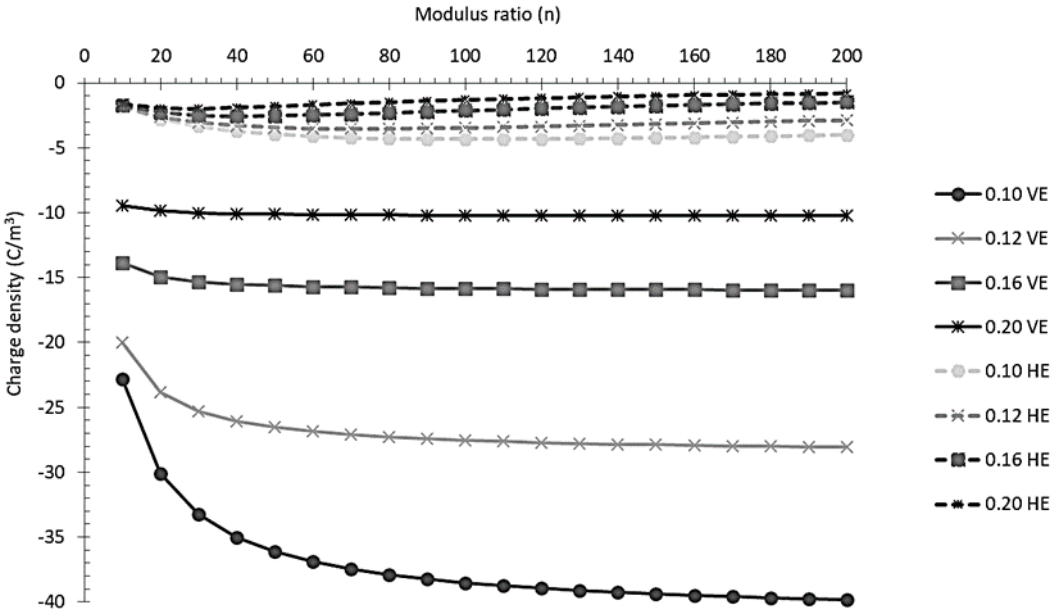

Fig. 4.9 Charge density computed for retaining structure of unit width, piezoelectric strain, modulus ratio, and thickness ratio on the top surface of the horizontally and vertically embedded soft *PZT* patch in the confined granular fill

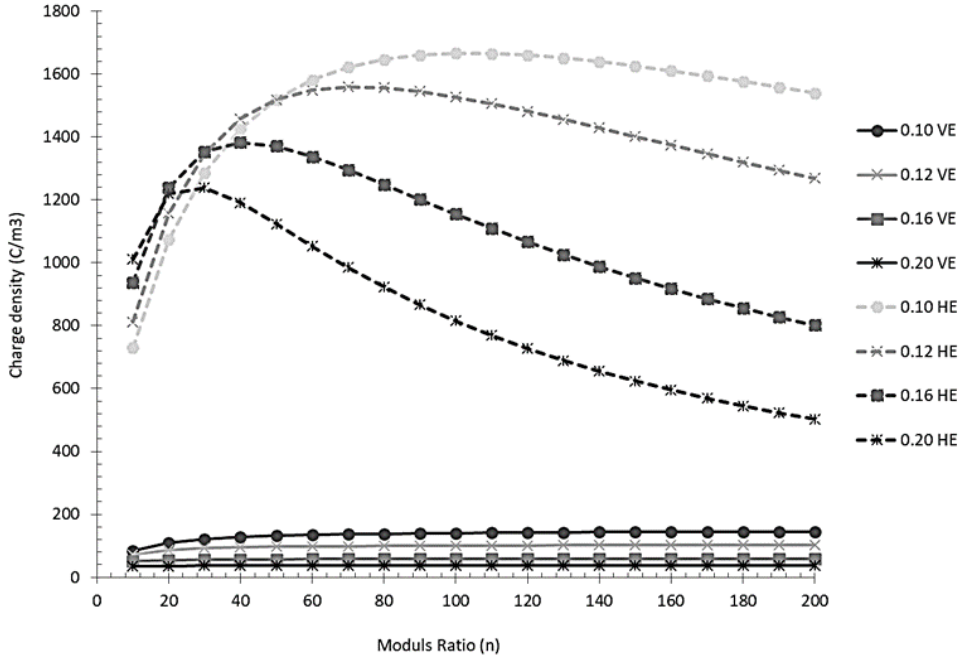

Fig. 4.10 Charge density computed for retaining structure of unit width, piezoelectric strain, modulus ratio, and thickness ratio on the bottom surface of the horizontally and vertically embedded soft *PZT* patch in the confined granular fill

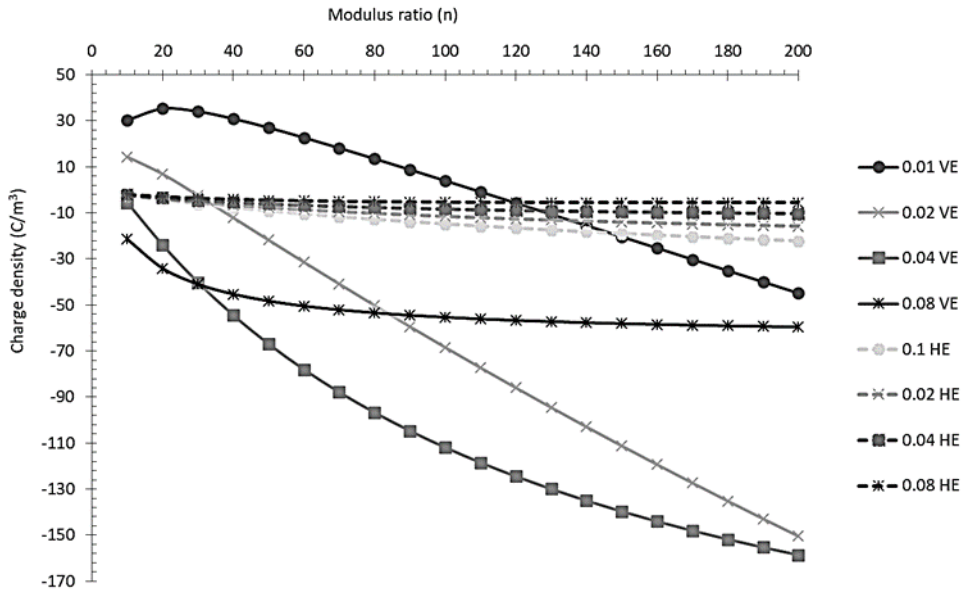

Fig. 4.11 Charge density computed for retaining structure of unit width, piezoelectric strain, modulus ratio, and thickness ratio on the top surface of the horizontally and vertically embedded soft *PZT* patch in the confined granular fill

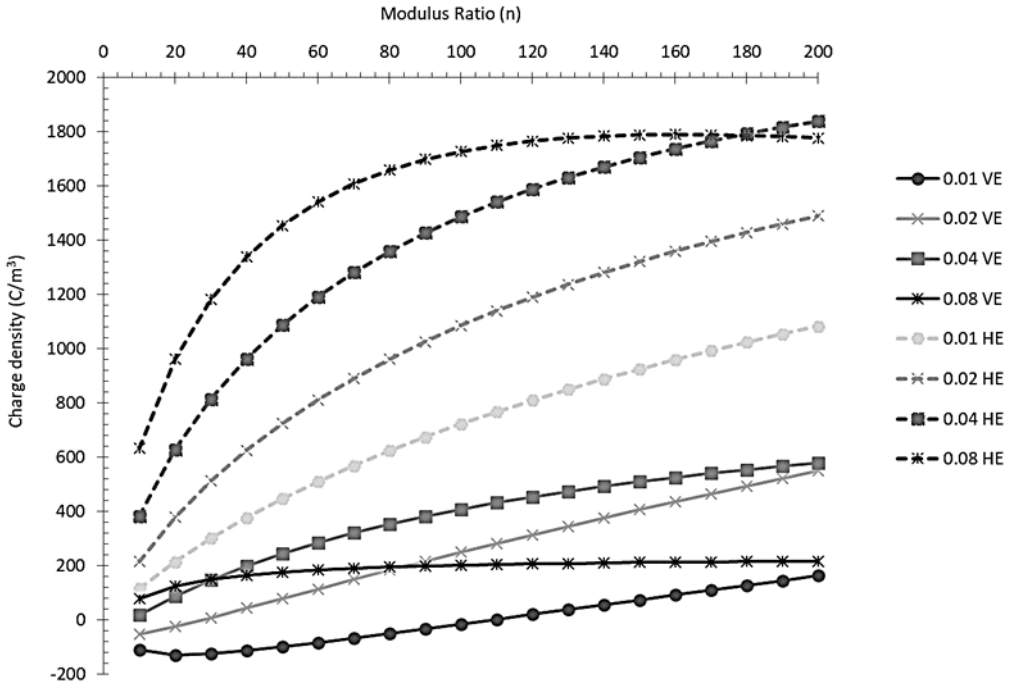

Fig. 4.12 Charge density computed for retaining structure of unit width, piezoelectric strain, modulus ratio, and thickness ratio on the bottom surface of the horizontally and vertically embedded soft *PZT* patch in the confined granular fill

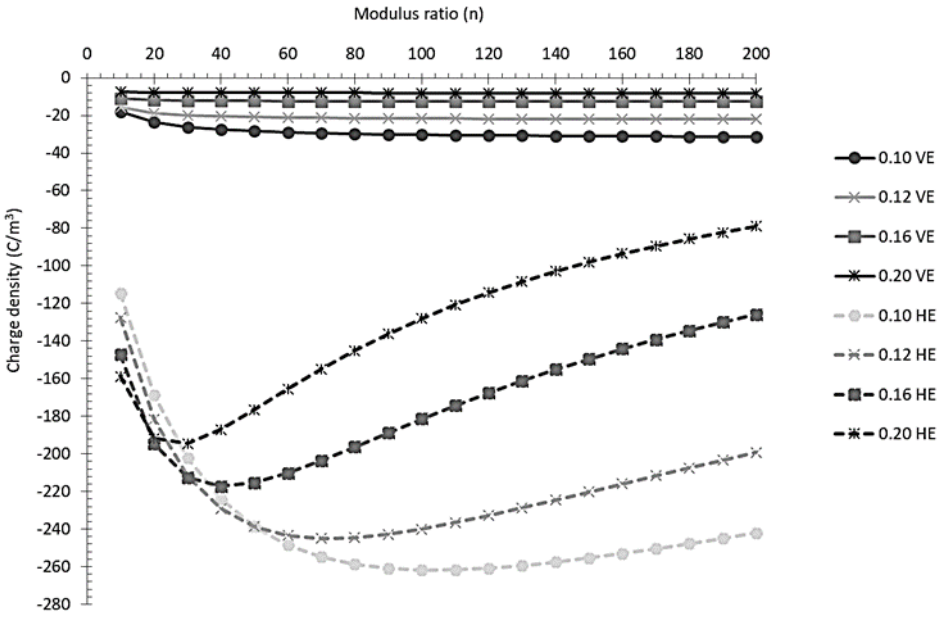

Fig. 4.13 Charge density computed for retaining structure of unit width, piezoelectric strain, modulus ratio, and thickness ratio on the top surface of the horizontally and vertically embedded semi-hard *PZT* patch in the confined granular fill

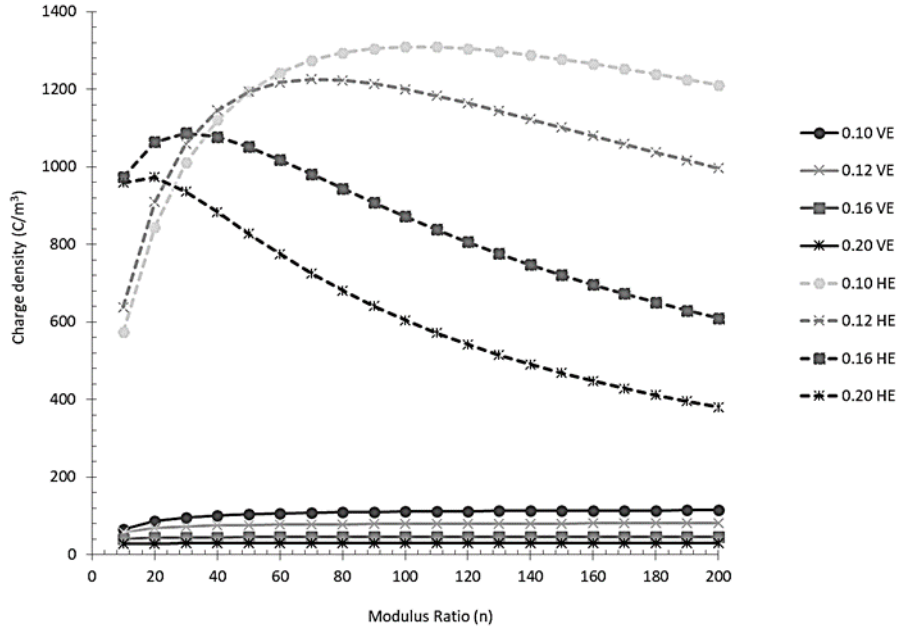

Fig. 4.14 Charge density computed for retaining structure of unit width, piezoelectric strain, modulus ratio, and thickness ratio on the top surface of the horizontally and vertically embedded semi-hard *PZT* patch in the confined granular fill

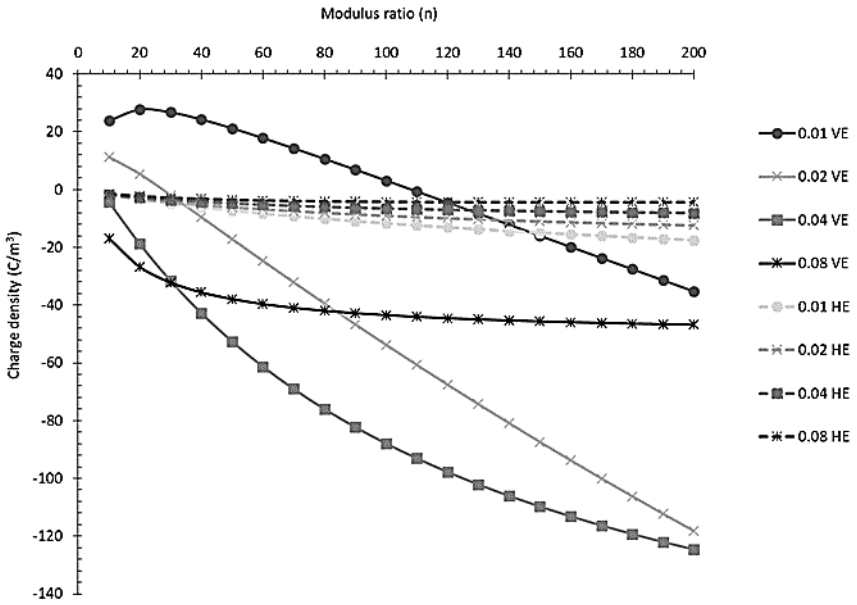

Fig. 4.15 Charge density computed for retaining structure of unit width, piezoelectric strain, modulus ratio, and thickness ratio on the top surface of the horizontally and vertically embedded semi-hard *PZT* patch in the confined granular fill

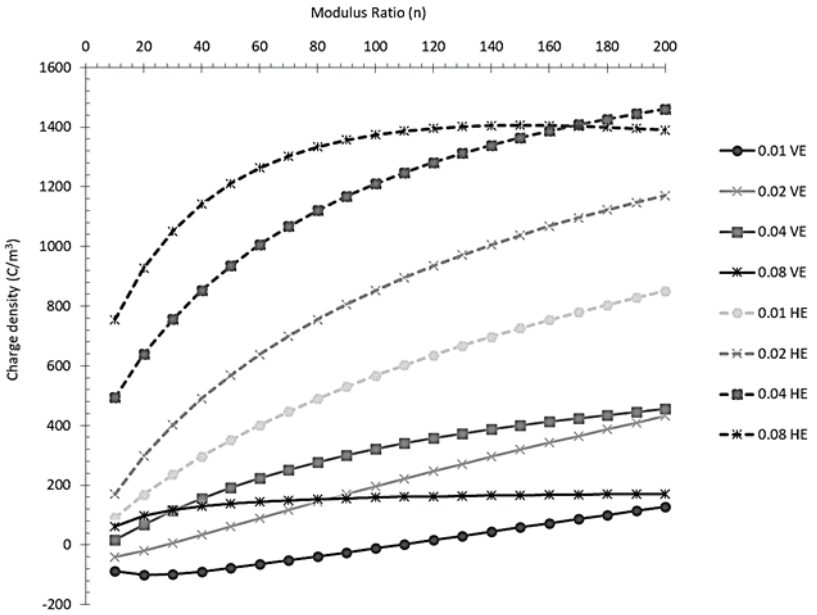

Fig. 4.16 Charge density computed for retaining structure of unit width, piezoelectric strain, modulus ratio, and thickness ratio on the bottom surface of the horizontally and vertically embedded semi-hard *PZT* patch in the confined granular fill

4.7.3 Comparative Analysis of Voltage Output

In this section, the voltage output from different *PZT* patches is analysed by considering the variation of the stress-strain response (Eq. 4.24-4.29). The key parameters influencing voltage output are the polarization, alignment of the *PZT* patch, thickness ratio, and material properties. The polarization of the *PZT* patch depends on the piezoelectric strain and the relative permittivity of the *PZT* material.

The comparison of the voltage output of the hard, semi-hard and soft *PZT* patches is shown in Figs. 4.17-4.18. As the thickness of the retaining wall increases, the voltage output increases up to a critical thickness ratio. A critical thickness ratio is defined as a ratio of the thickness of the granular fill to that of the *PZT* patch at which the maximum energy is harvested.

Table 4.3 Voltage output for various *PZT* patches

Type of the *PZT* patch	Maximum voltage output for horizontally embedded *PZT* patch (Volt)	Maximum voltage output for vertically embedded *PZT* patch (Volt)	Difference (%)
Hard (H)	0.44	0.05	159.18
Semi-hard (SH)	0.56	0.06	161.29
Soft (S)	0.33	0.04	156.75

The semi-hard *PZT* patch shows the highest voltage output due to the highest polarization ratio of 0.114. At the critical thickness ratios of 0.2 and 0.4, the maximum voltage is obtained for horizontally and vertically aligned patches, respectively as shown in Table 4. The maximum voltage output observed for horizontally embedded patches is 0.44, 0.56, and 0.33 volts. Similarly, the voltage output is 0.05, 0.06, and 0.04 volts for vertically embedded hard, semi-hard, and soft *PZT* patches. The variation in output voltage indicates that the interaction between the *PZT* patch and the retaining wall strongly influences the energy output from the confined granular fill.

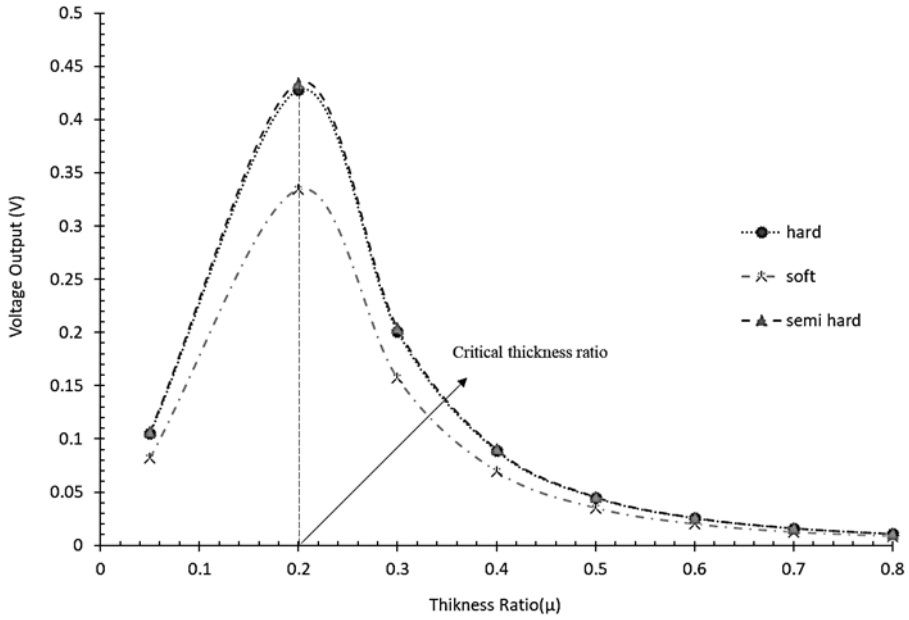

Fig. 4.17 Voltage output computed for the retaining structure, piezoelectric strain constant, polarization ratio (0.112, 0.087 and 0.114) and thickness ratio of horizontally embedded hard, semi-hard and soft *PZT* patch in the confined granular fill

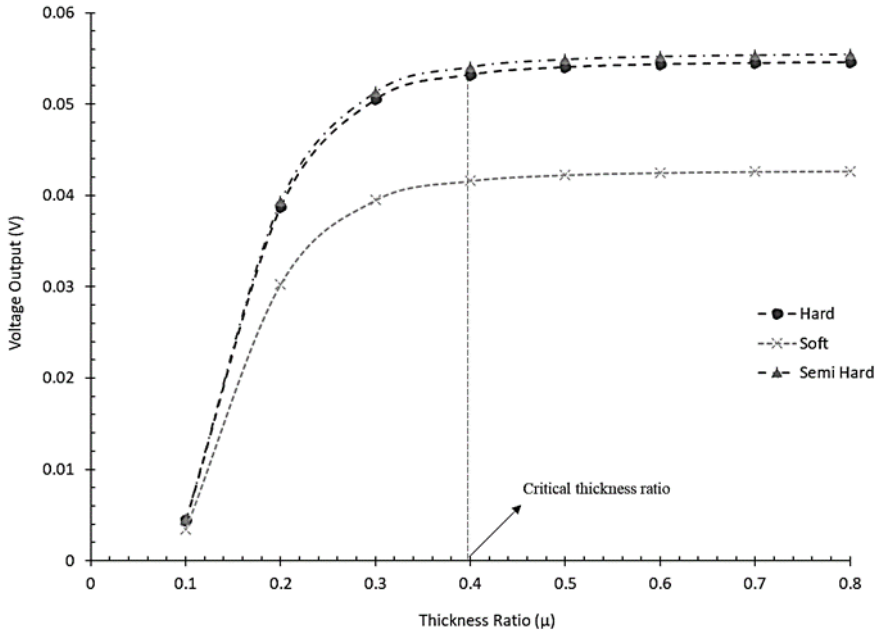

Fig. 4.18 Voltage output computed for the retaining structure, piezoelectric strain constant, polarization ratio (0.112, 0.087 and 0.114) and thickness ratio of vertically embedded hard, semi-hard and soft *PZT* patch in the confined granular fill

4.7.4 Effect of External Resistance on Power Output of the *PZT* Patch

This section shows the effect of external resistance on the voltage and power output of the *PZT* patch as per its alignment in the granular fill. Fig. 19 shows the magnitude of voltage output for the different external resistances. The voltage magnitude increases logarithmically until a peak voltage of 56 mV for the horizontally embedded *PZT* patch and 6μV for the vertically embedded *PZT* patch. The magnitude of the voltage output from experimental data from Wang et al. (2018) and Petroff et al. (2019) is appropriate for MRA and HRA, respectively. Eq. (26) shows a generalized relationship for the output voltage based upon a set of design parameters considered by the present study. An empirical relationship of output voltage for high, medium, and low resistance applications for varying design parameters is expressed as,

$$V = \xi R^{\eta} \tag{4.30}$$

The variables ξ and η depend upon the design parameters namely, polarization, modulus ratio, position of the *PZT* patch, strain, geometrical and engineering properties of the confined granular fill and retaining structure. The response of the *PZT* patch can be optimized by changing the design parameters and mechanical properties. Table 4.4 shows the classification of the application of *PZT* patches based on the voltage output for external resistance. Based on the range of external resistance the applications of *PZT* patches are classified as low resistance, medium resistance and high resistance applications.

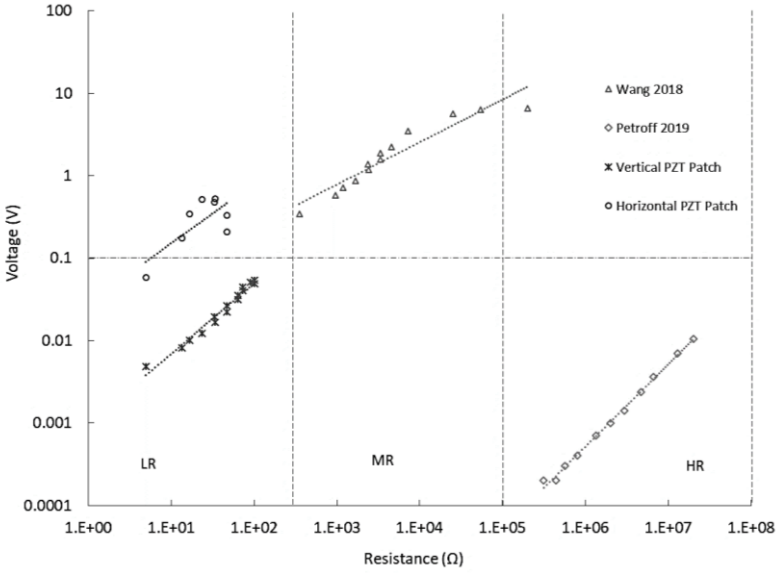

Fig. 4.19 The output voltage for different external resistance for high, medium and low resistance applications

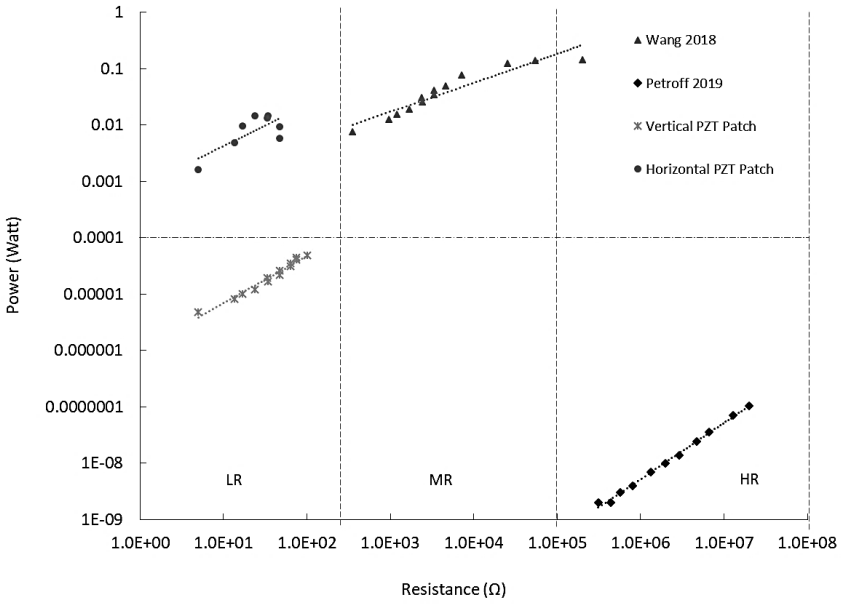

Fig. 4.20 Power output for different external resistance for high, medium and low resistance applications

Table 4.4 Classification of *PZT* applications for output voltage and resistance

Description	ξ	η	Output voltage (Volt)	Resistance (Ω)	Classification
A flexible piezoelectric energy harvester [a]	5E-10	0.996	10^{-4} – 10^{-1}	10^{8} -10^{5}	High resistance applications (HRA)
A two-degree freedom system with the piezoelectric element [b]	0.0224	0.514	10^{-1} – 10^{1}	10^{5}-10^{2}	Medium resistance applications (MRA)
Horizontally embedded *PZT* patch [c]	0.001	0.8561	10^{-1} – 1	10^{2}-1	Low resistance applications (LRA)
Vertically embedded *PZT* patch [d]	0.0282	0.7274	10^{-3} – 10^{-1}	10^{2}-1	Low resistance applications (LRA)

[a] Petroff et al. (2019), [b] Wang et al. (2018), [c, d] Present study

Fig. 4.19 illustrates the magnitude of the power of the present work and experiment results from the literature are plotted with high medium and low resistance applications. The higher power output is observed for the horizontally embedded *PZT* patch for the same range of external resistance. The alignment of the *PZT* patch significantly affects the voltage and power output due to the vertical and lateral vibrations due to dynamic loads.

The comparison of the voltage output of the hard, semi-hard and soft *PZT* patches is shown in Figs. 4.19-4.20. As the thickness of the wall retaining granular fill increases, the voltage output increases up to a critical thickness ratio. A critical thickness ratio is defined as the ratio of the thickness of the granular fill to that of the *PZT* patch at which the maximum energy is harvested.

Chapter 5

Effect of Confined Granular Fill on Efficiency of *PZT* Patches

This chapter is based on the article published in Applied Sciences as listed in section 1.8. The details are presented here with some changes in the layout to maintain consistency in the presentation throughout the thesis.

5.1 Introduction

The advances in smart infrastructure and the rise in demand for energy have led to generating energy sources utilizing mechanical vibrations. Substantial research has been embarked upon to elucidate the influence of the configuration of piezoelectric energy harvester (*PEH*) on its efficiency of energy conversion (Roundy et al. 2003; Kim et al. 2004; Jung et al. 2011; Wang et al. 2015; Zhang et al. 2019). Kim et al. (2004) analyzed the Cymbal *PEH,* which can generate power (1.2 mW) at 20 Hz frequency for each passing vehicle. Subsequently, per vehicular movement on asphalt pavement, the electrical voltage and energy were generated (order of 97 V and 0.06 J, respectively).

This section explores an experimental analysis of the influence of the abutting material's properties and the excitation frequency on the voltage output of *PZT* patches. Some experiments have been conducted on confined granular fill at varying depths to analyze the effect of embedment depths. This paper shows the effect of both vertical and transverse mechanical vibrations of varied excitation frequencies. The dynamic response of experimental data is analysed using fast Fourier transformation (*FFT*) in the frequency domain. The system's natural frequency is investigated experimentally, and the peak pick method from the frequency response (*FRF)* function of the system. An analysis of the influence of excitation frequency, embedment depth and displacement on voltage output is presented based on experimental data. Further, static cone penetration tests have been carried out to monitor the effect of confinement

under various excitation frequencies. This effort emphasizes the utility of *PZT* patches in granular fills with vibration and their uses in piezoelectric energy harvesting from the ambient vibration from civil structures.

5.2 Properties of Granular Fill and *PZT* Patches

The granular material used in the present work is classified as poorly graded sand using the particle-size analysis per the Indian Standard Soil Classification system (IS: 2720). The grain size distribution curve of the granular soil is shown in Fig. 5.1.

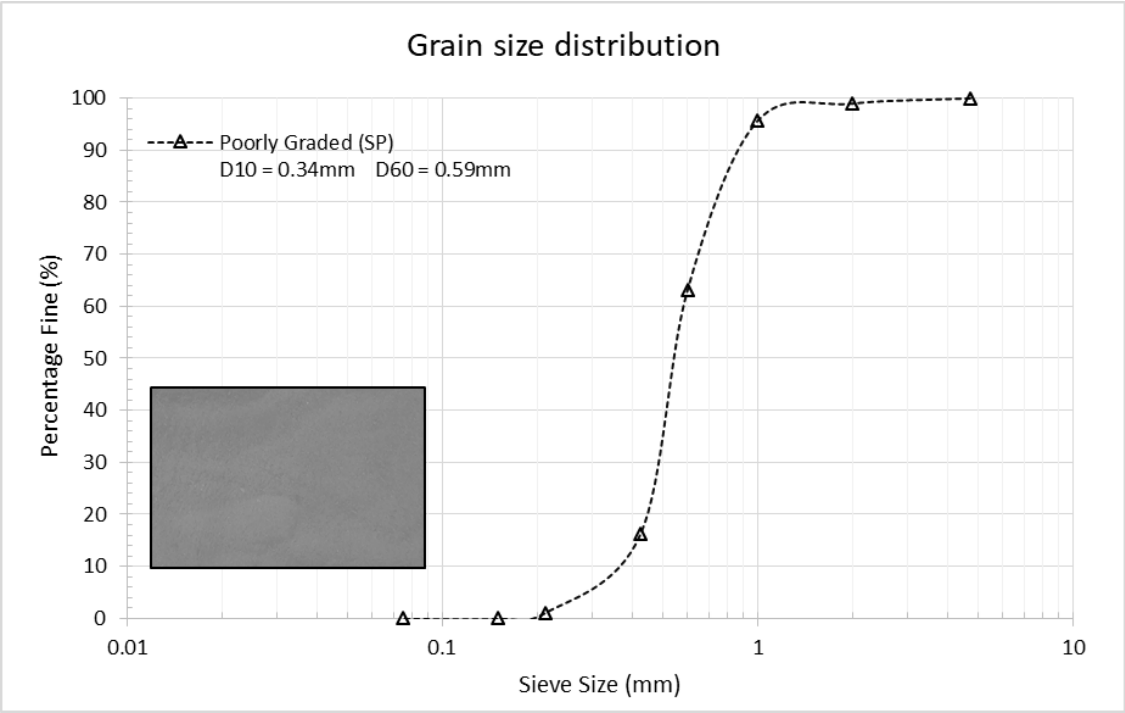

Fig. 5.1 Particle size distribution of granular material used in the present study

Table 5.1 Index properties of the confined granular materials

Maximum dry unit weight ($kN.m^{-3}$)	Degree of compaction (%)	Specific gravity	Optimum moisture content (%)	IS classification
18.4	96.7	2.50	14.0	SP

Piezoceramic (*PZT*) materials have been widely applied to convert mechanical energy into electrical energy in engineering applications (Erturk, 2011; Peigney and Siegert, 2013; Xiang et al., 2013; Kumari and Trivedi, 2020). The constitutive equations for electrical displacement and piezoelectric strain in *PZT* materials are shown in Eq. (5.1-5.2).

Table 5.2 Properties of the *PZT* patch

Properties	Symbol	Magnitude
Dielectric constant	$\frac{\varepsilon_{33}^{T}}{\varepsilon_{o}}$	3270
Piezoelectric charge constant (pC N^{-1})	d_{31}	-275
Piezoelectric voltage constant (10^{-3} Vm N^{-1})	g_{31}	-9.5
Young's modulus (GPa) of *PZT*	Y	61
Unit weight (kN m^{-3}) of *PZT*	γ	7.2

The *PZT*-soil coupled system can be modelled as a 1-D system as the constraint along the thickness direction of the *PZT* patch. In the vertical direction, assuming the polarization is along the z-axis. In the transverse direction, the polarization is along the x-axis. The *PZT* material is considered an isotropic material in the x-y plane. Thus, the constitutive equations (Eq. 5.1 & Eq. 5.2) of the *PZT* patch are expressed as,

$$S_{ZP} = S_{33p}^{E} T_{ZP} + d_{33} E_Z \; ; \; S_{xP} = S_{31p}^{E} T_{xP} + d_{31} E_x \tag{5.1}$$

$$D_Z = d_{33} T_{ZP} + \xi_{33}^{T} E_Z \; ; \; D_x = d_{31} T_{xP} + \xi_{31}^{T} E_x \tag{5.2}$$

The stress-strain in soil material along the z and x- directions can be expressed as follows,

$$\varepsilon_{ZS} = S_{33S}^{E} T_{ZS} \; ; \; \varepsilon_{xS} = S_{31S}^{E} T_{xS} \tag{5.3}$$

where, ε_{ZS} and T_{ZS} are the stress and strain vectors of the granular soil along the z-direction, respectively. ε_{xS} and T_{xS} are the stress and strain vectors of the granular soil along the x-direction, respectively. S_{33S}^{E} represents the elastic compliance coefficient of the granular soil.

The geometric relationship equations of the *PZT* patch and granular soil composite system (Zhang, 2020) are expressed as,

$$\varepsilon_{ZS} = \varepsilon_{PS} = \frac{\partial w_{PS}}{\partial Z}\ ;\ \varepsilon_{xS} = \varepsilon_{PS} = \frac{\partial w_{PS}}{\partial X} \qquad (5.4)$$

$$E_Z = -\frac{\partial \phi}{\partial Z} = 0\ ;\quad E_x = -\frac{\partial \phi}{\partial X} = 0 \qquad (5.5)$$

where w_{PS} is the displacement of the *PZT* patch and soil composite in the z direction, and ϕ is the electric potential. In the present study, the external electric field is considered negligible.

5.3 Experimental Set-up for Voltage Output from *PZT* Patches

5.3.1 Model Set-up

In order to study the effect of the exciting frequency and depth of the *PZT* patch on voltage output a laboratory set-up was designed. A steel tank (600x460x400 mm^3)was used. The experimental set-up includes the steel tank, granular material, dynamic shaker, *PZT* patches, piezoelectric accelerometers (sensors), *FFT* analyzer, and an oscilloscope as shown in Fig. 5.2. The vibration tests were performed through a steel plate of size (270x230x10 mm^3). The depth of embedment of *the PZT* patch in the granular fill (*h*) is shown in Fig. 5.2. Compared to the depth of the fill (*H*) depth of the *PZT* patch is presented as depth ratio (h_r) in subsequent text.

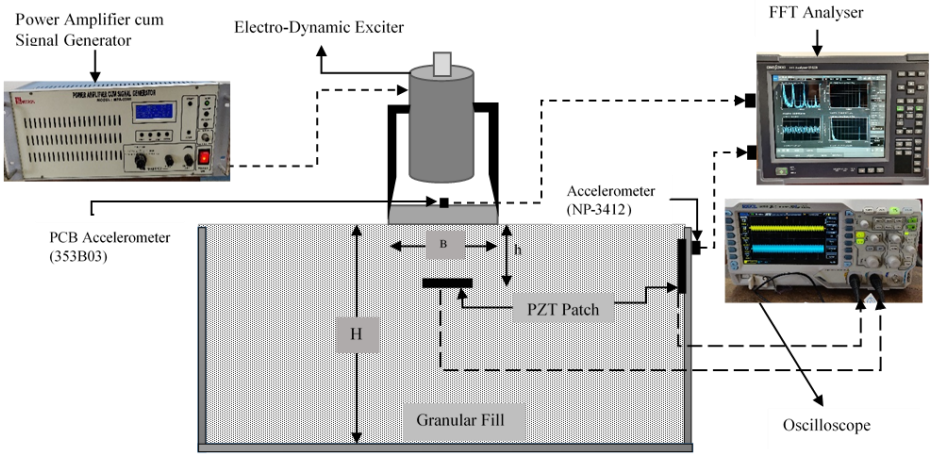

Fig. 5.2 Laboratory experimental set-up for dynamic response and voltage measurement

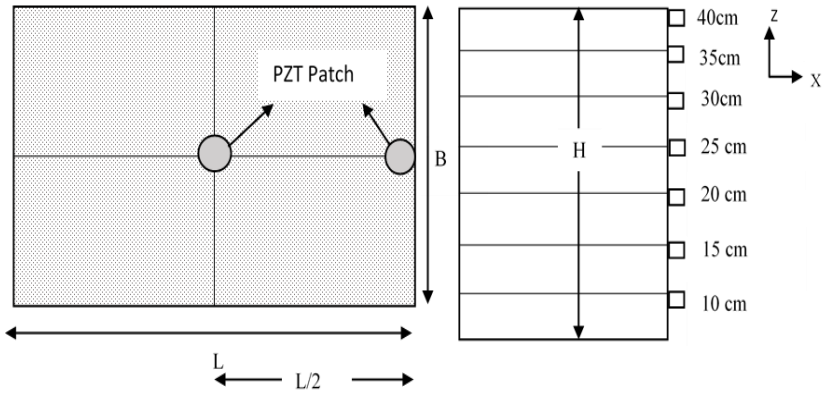

(a)

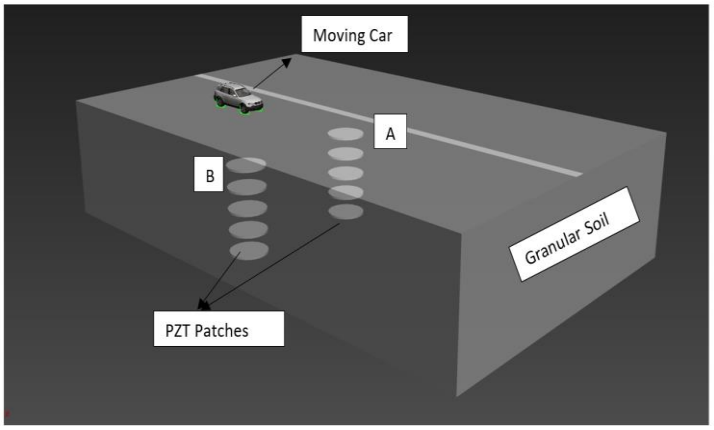

(b)

Fig. 5.3 (a) Layout of the *PZT* patch embedded into the confined granular fill for the vertical and transverse vibrations (b) The optical image of the embedded *PZT* patches in pavement

5.3.2 Electrodynamic Exciter and Instrumentation

An electro-dynamic exciter (MEV-0020) was used to produce vibration. The system generated the vibrations with the drive coil connected rigidly to the moving platform and positioned. When AC flows in the drive coil, it gives rise to a force by converting an electric current into mechanical vibrations that move the platform. It was connected to the power amplifier cum signal generator (MPA-0500) to control the mechanical force. The function of a power amplifier cum signal generator was used to generate and amplify the signal sufficiently to drive the exciter to the desired frequency.

The dynamic response of the confined granular soils has been monitored using two accelerometers, one PCB piezoelectric accelerometer (353B03) with low noise cable (M003) and one accelerometer (NP-3412) with signal cable (S381) (Fig. 2). The PCB (353B03) has a sensitivity of 9.98 mV/g, transverse sensitivity of 0.9%, and resonant frequency of 56.1 kHz. The accelerometer NP- 3331 has a sensitivity of 5.038 mV/g. Both sensors were connected to an *FFT* analyser (CF-9200). The *FFT* analyser has a bandwidth of 0.1- 10^5 Hz and a frequency tolerance of ±0.005%. The PCB accelerometers were attached to the centre of the granular fill to measure the vertical vibration. An accelerometer (NP-3412) was employed on one side of the tank to monitor the horizontal vibration. The data is collected as *FFT* spectrum and *FRF* (frequency response function) of vibration for various exciting frequencies.

To measure the effect of vibration on the voltage output of piezoelectric patches. The positive and negative node of the *PZT* is connected to an oscilloscope (DS1102Z-E) using the probes (PVP 3150). The output data is obtained in the form of voltage vs time.

5.3.3 Digital Static Cone Penetrometer (DSCP)

A digital static cone penetrometer (SCP) test is a low-cost method for measuring the penetration resistance of fine granular materials during site investigation and laboratory

research. The cone tip was hydraulically forced into the soil at a consistent penetration rate during the SCP test. The cone tip resistance and sleeve friction resistance were measured. In this study, a digital SCP was used, which consists of a measuring body with two push handles, a drive rod with a diameter of 16 mm and a length of 498 mm, a 60° cone (area of cone base Ac = 9.97 cm^2) assembled at the bottom of the drive rod, a linear variable displacement transducer (LVDT) with a range of 0–200 mm, a data acquisition system with a USB output slot, and a load cell with a capacity of 300 kg, as shown in Fig. 5.4. It also depicts the layout of the test sections in the soil tank.

The digital SCP is handheld equipment capable of penetrating sub-base and subgrade soils. The push handles are provided at the head assembly of the digital SCP. It penetrates the cone attached to the driving rod into the soil at a constant force given with the help of body weight. During the testing, both the load cell and the LVDT were active. The load cell assists in measuring the applied load, while the LVDT measures the digital SCP penetration. Both provide the electrical signal to the data acquisition system, transforming it from analogue to digital. The digital SCP was positioned vertically on the surface of the granular soil. Jerks were avoided while pushing the handles of the digital SCP since they affect the output data. The load cell and LVDT data were automatically saved in a tabular format with two columns, load and displacement, in the USB output device. When the applied force causes a negligible change in the magnitude of penetration, the device records refusal. It may produce inconsistent readings and damage the cone, driving rod, and load cell.

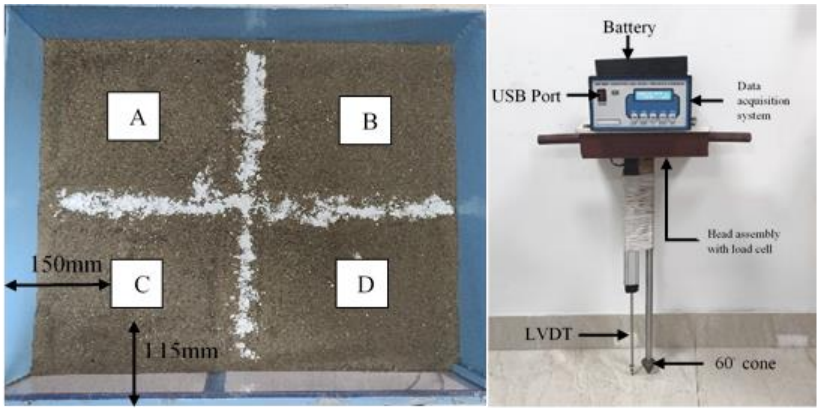

Fig. 5.4 Layout of the test section measurement and testing location of the DSCP test

5.3.4 Model Parameter Estimation

The peak picking modal estimation technique has been utilized in natural frequency analysis. It has been commonly used due to its simplicity. The dynamic response of a system to an external excitation load is described as,

$$M\ddot{x}(t) + C\dot{x}(t) + Kx(t) = F(t) \qquad (5.6)$$

where M, C, and K are matrices of mass, damping, and stiffness of the system. Also, x, ẋ, and ẍ represent the displacement, velocity, and acceleration response of the system, respectively.

The peak picking method is considered for estimating the modal features of a dynamic system based on response data. This approach could characterize ambient vibration excitation as standard white-noise Gaussian distribution. Based on the fact that the frequency response function (FRF) of a system would experience peak values in the frequency domain. In the case of a white noise excitation, the *FRF* of a system at sensor location k, $H_k = (jw)$, is considered equivalent to the Fourier spectrum of the response data gathered by the sensor. This range is derived by converting the measured response to the frequency domain using *FFT*. Therefore, the natural frequency of the system is the dominant frequency of the *FRF* of the system (Zimmerman et al., 2008).

The damping loss factor is analysed using the frequency response function expressed as follows,

$$\left|\frac{x}{F}\right| = \frac{1/k}{\sqrt{1-\left(\frac{\omega^2}{\omega_n^2}\right)^2 + \frac{4\xi^2\omega^2}{\omega_n^2}}} \qquad (5.7)$$

where, ξ is the damping loss factor, the natural frequency of the system $\omega_n = \sqrt{k/m}$, and the spring constant *k*. ω is excitation frequency.

The measurements of modes at resonances are difficult for a lightly damped system. Simultaneously, the response of a heavily damped system is significantly influenced by more than one mode. The mode shapes are determined by the peak picking method using the system's FRFs.

5.4 Discussion on DSCP Results and Voltage Output of *PZT* Patches Using *FFT*

5.4.1 Natural Frequency Analysis

The fast Fourier transformations (*FTT*) are utilized to obtain the damping characteristics and natural frequency of the system in the frequency domain. The piezoelectric accelerometers were attached at various depths (*H*= 20cm, 25cm, 30cm, 35cm, and 40cm) to analyse the dynamic response of confined granular fill. The arrangement of the accelerometer is shown in Fig. 5.3. The confined granular fill was subjected to vibrations of various frequencies (*f*=10-50 Hz). The peak amplitude of the acceleration, velocity, and displacement response at various excitation frequencies is shown in Table 5.3 for both vertical and transverse vibrations.

The peak response (acceleration, velocity, and displacement) of the confined granular fill at the same position varied directly as the excitation frequency. A similar observation was made by

Ding et al., 2018 for the dynamic response of the subgrade at various exciting frequencies. The peak response of the confined granular at the centre point is greater than the point to the right; due to the boundary effect. The geometric law has been followed to understand the relationship between stress, strain, and displacement. The displacement spectrum for various excitation frequencies characterizes the vibrations generated at different depths.

Fig. 5.5 shows the displacement response spectrum of the system at various excitation frequencies (f=10-50Hz) at varying depths of the confined granular fill. This spectrum was obtained using the *FFT* analyser and accelerometers. The purpose of obtaining the system's response spectrum is to analyze the damping loss factor and natural frequency of the system. The displacement has a maximum at the natural frequency for the excitation frequencies of 10-30 Hz. In this case, the peak is at 31 Hz. For high frequencies, the peak displacement tends towards 40Hz. The confined system will behave at high frequencies as a rigid body, so the mass follows the upper layer motion. Fig. 5.5 (E) depicted that the peak displacement of the vibration is obtained at the 40cm thickness. Whereas for low frequencies (10-30 Hz), the maximum displacement obtained towards 30cm. The displacement response also represents the intensity of the vibration at a deeper depth to understand the effect of vibration on the *PZT* patches embedded at various thicknesses of the granular fill.

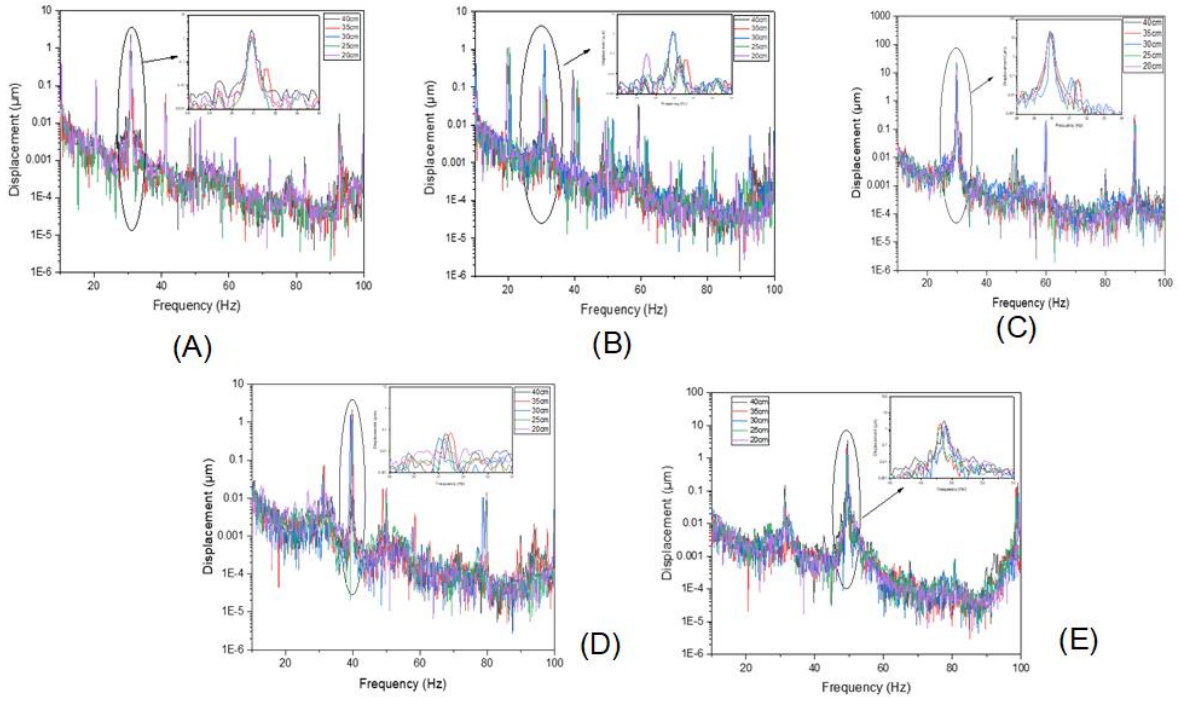

Fig. 5.5 Influence of depth of granular fill (20-40cm) on the displacement spectrum at an excitation frequency of (A) 10Hz (B) 20Hz (C) 30Hz (D) 40Hz (E) 50Hz

The natural frequency and damping loss factor have been analysed using the peak pick modal parameter method from the frequency response function (*FRF*) of experimental data.

Table 5.3 Damping loss factor and natural frequency of the confined granular fill

Excitation frequency (Hz)	10	20	30	40	50
Natural frequency (Hz)	31	31	30	32	49
Damping loss factor (ξ)	0.121	0.127	0.132	0.176	0.122

5.4.2 Cone Resistance of Confined Granular Fill

Fig. 5.6 (a) presents the cone resistance of filled granular soil subjected with and without external dynamic vibrations. Digital SCP tests were performed at locations 'A', 'B,' 'C,' and 'D' in the test section. Singh et al. (2020) performed a digital SCP test to estimate the load displacement of fine-grained soils. Digital SCP results are not identical at all the testing

locations. However, they follow a similar pattern for each test section at different excitation frequencies. The cone resistance can be utilized to determine the stress at a penetration depth. The results clearly show that after 10-20Hz frequency vibration, granular soil has greater resistance against applied load than before vibration. After 30Hz frequency vibration, the cone resistance decreased up to 22% due to a change in the relative density of the granular fill. The relative density and overburden pressure control the cone resistance of the granular fill (Trivedi and Singh, 2004). Fig. 5.6(b) presents the cone resistance of the granular fill after 40-50 Hz excitation frequency.

Table 5.4 Fitting parameters α and β for the confined granular fill at varying excitation frequency

Exciting Frequency (Hz)	α	β	R^2
10	-3E-05	0.1157	0.9976
20	-3E-05	0.1035	0.9988
30	-7E-05	0.1539	0.9978
40	-6E-05	0.1439	0.9946
50	-8E-05	0.1432	0.9814

It is observed that the cone resistance value increases after excitation frequency above the natural frequency. The overlapping at shallow depth signifies an unstructured response at low overburden pressure. The relationship between the cone resistance and penetration depth at varying excitation frequencies followed an empirical law as,

$$D_P = \alpha q_c^2 + \beta q_c \qquad (5.8)$$

where α and β are fitting parameters that vary with an excitation frequency of vibration (Table 5.4) with a satisfactory value of the coefficient of regression (R^2). The cone resistance q_c and depth of penetration D_p are expressed in kPa and mm, respectively.

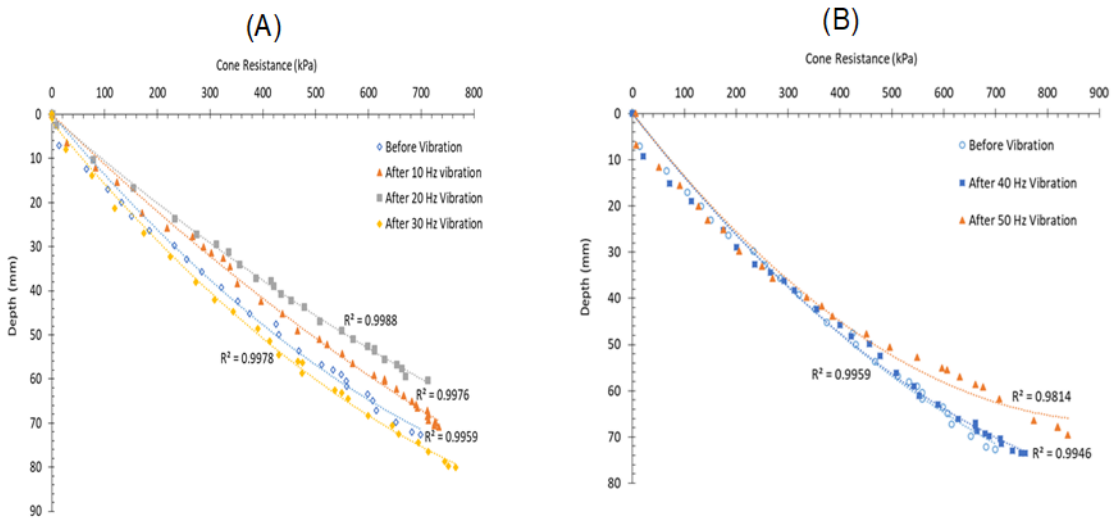

Fig. 5.6 Cone resistance obtained from digital SCP data for confined granular fill with and without excitation frequency of (A) 10-30 Hz (B) 40-50 Hz

5.4.3 Analysis of Output Voltage

Fig. 5.7 plots the variation of the voltage output of the *PZT* patch for the excitation frequency at different embedment depths of *PZT* in the vertical direction (f=10-50 Hz, H=40cm, h_r=0.5-1). The variation in maximum output voltage at varied excitation frequencies is due to the displacement of granular soil. Compared with the other excitation frequency, it is found that maximum voltage output in the vertical direction was obtained for the depth ratio of 0.5 at resonance. Thus, a greater output voltage is obtained if the *PZT* patch is arranged at an appropriate depth from the surface of the granular soil. In other words, the *PZT* patch cannot be placed at a greater depth ratio and shallow depth in granular soils, as this reduces the voltage output efficiency. The efficiency of voltage output for the *PZT* patch embedded in a vertical direction at various excitation is shown in Table 5.5. The efficiency of the voltage output at varied excitation frequencies is analysed using the formula

$$\left[\eta = \left(V_{f_1} - V_{f_2}\right) \Big/ \left(V_{f_1}\right)\right] \qquad (5.9)$$

where, V_{f_1} is the voltage output of *PZT* patch at 10Hz frequency and V_{f_2} is the voltage output of the *PZT* patch at various frequencies (20-50Hz).

For the same excitation frequency, when the depth ratio (ratio of embedded depth to the height of the granular fill) was increased from 0.5 to 1, the maximum voltage decreased and again increased to the depth ratio of 1.

Table 5.5 Voltage output efficiency of *PZT*-patch embedded in poorly graded soil for various excitation frequencies

Depth ratio (hr)	Input Excitation Frequency (Hz)	Voltage output in vertical direction (V_v)	Efficiency (%)	Voltage output in the transverse direction (V_t)	Efficiency (%)
0.5	10	2.6		2.3	
	20	1.2	54	2.2	4.3
	30	1.7	35	2.4	4.3
	40	1.4	46	1.9	17.4
	50	2.1	19	2.2	4.3
0.6	10	2		2.4	
	20	1.1	45	1	58
	30	1.3	35	2.6	8
	40	1.3	35	0.9	63
	50	1.5	25	1.7	29
0.7	10	2.4		1.9	
	20	1.3	46	1.2	37
	30	1.1	54	1.5	21
	40	1.5	38	1.6	16
	50	1.7	29	1	47
0.8	10	1.6		2.4	
	20	1.5	6	2.8	17
	30	1.4	13	2.2	8
	40	2.3	44	2.3	4
	50	2.2	47	2	17
1	10	3.2		2.2	
	20	2.3	28	2.5	14
	30	2.1	34	2	9
	40	2.1	34	2.1	5
	50	3.0	6	1.9	14

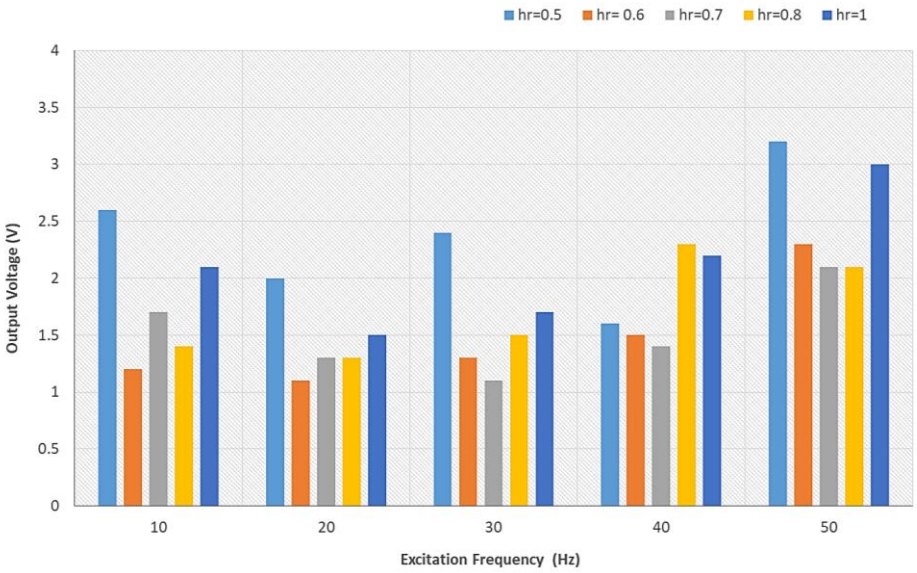

Fig. 5.7 Output voltage for *PZT* patches embedded at varying depths in the vertical direction

Fig. 5.8 shows the voltage output variation of the *PZT* patch for the excitation frequency at different embedment depths in the transverse direction (f=10-50 Hz, H=40cm, h_r=0.5-1). This attempt was made to analyse the effect of vibration on the *PZT* patch embedded at a distance in a lateral direction from the centreline. Table 5.5 shows the voltage output efficiency of *PZT* patches at various exciting frequencies embedded in a lateral direction. It can be observed from Fig. 8 that the output voltage was minimum at 30Hz excitation frequency and maximum at higher frequencies for a depth ratio of 0.6. Thus, the maximum voltage output is obtained at more than 30 Hz excitation frequency in the transverse direction. The variation in the output voltage at varied excitation frequencies is due to the confinement of the granular fill. Hence, the distance from the centreline of the load influences the efficiency of the *PZT* patch embedded in confined granular fill. A similar result was found by Ding et al. 2018.

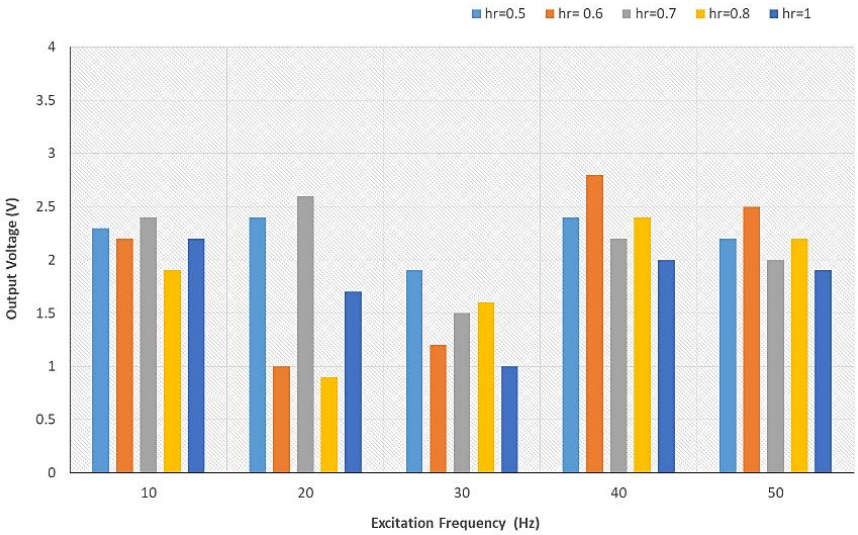

Fig. 5.8 Output voltage for *PZT* patches embedded at varying depths in the transverse direction

Thus a greater output voltage is obtained if the *PZT* patch is arranged at an appropriate depth from the surface of the granular soil. In other words, the *PZT* patch cannot be placed at a greater depth and at the surface of granular soils due to reduced voltage output.

Chapter 6

Investigation of Strain Sensitivity and Energy Output of *PZT* Patches

This chapter is prepared to investigate and evaluate strain sensitivity and energy output of PZT patches embedded in confined granular fills. It is proposed to be submitted to a reputed journal for publication.

6.1 Introduction

Piezoelectric materials have become increasingly popular due to their unique ability to convert mechanical energy into electrical energy and vice versa. This phenomenon, known as the piezoelectric effect, has led to various applications such as energy harvesting, structural health monitoring, and vibration control.

The strain sensitivity and energy output significantly impact the performance of the *PZT* patches. The strain sensitivity is the relationship of strain as a function of frequency at varied depths of embedment of *PZT* patches. The power and energy output is presented as a function of depth ratio at varied frequencies. On the other hand, the energy output represents the amount of electrical power that can be harvested from the *PZT* patch under different embedment depths and excitation frequencies. Therefore, the characterization of these properties is crucial for designing and optimising *PZT*-based devices.

This section investigates the strain sensitivity, power and energy output of PZT patches under the vibration of various excitation frequencies. The experimental methodology incorporated *PZT* patches embedded in confined granular fill medium at varying depths. The voltage output of the *PZT* patches was captured through experimental means, facilitating the evaluation of both strain sensitivity and energy output. The response of the system to vertical mechanical vibrations was thoroughly examined.

6.2 Material Properties

The granular material used in the present section is classified as poorly graded sand using the particle size analysis as per the soil classification system (IS:2720). The grain size distribution curve of the granular soil is shown in Fig. 5.1. The engineering properties of the granular soil are also determined in the laboratory and given in Table 5.1. The properties of *PZT* patches used in the experimental study are given in Table 5.2.

6.3 Experimental Set-up

A laboratory set-up was designed to investigate the effect of the exciting frequency and embedment depth of the *PZT* patch on strain sensitivity and energy output. The experimental setup includes the steel tank, granular material, dynamic shaker, *PZT* patches, piezoelectric accelerometer, *FFT* analyzer, and oscilloscope. The *PZT* patches are embedded in a steel tank (600x460x400 mm^3). The vibration tests were performed through a steel plate of size (270x230x10 mm^3). The depth of embedment of the *PZT* patch in the granular fill (h) as compared to the depth of the fill (H) is presented as depth ratio (h_r) as shown in Fig. 5.2.

The dynamic response of the confined granular soil was monitored using two accelerometers. Both sensors were connected to an *FFT* analyzer with a bandwidth of 0.1- 10^5 Hz and a frequency tolerance of ±0.005%. An accelerometer was attached to the center of the granular fill to measure the vertical vibration, yet another accelerometer was employed on one side of the tank to monitor the horizontal vibration. To measure the effect of vibration on the voltage output of the *PZT* patches, the positive and negative node of the *PZT* was connected to an oscilloscope to capture voltage output.

The strain sensitivity and energy output of the *PZT* patches were determined by analysing the data obtained from the laboratory set-up. The voltage output of the *PZT* patch is directly proportional to the strain generated on the *PZT* patch. The strain sensitivity and energy output

are calculated by measuring the voltage output under varied excitation frequencies and embedment depths.

6.4 Result and Discussion

6.4.1 Effect of Excitation Frequency on Strain Sensitivity

The strain sensitivity and energy output of *PZT* patches were found to be highly dependent on the frequency of excitation. The strain sensitivity in a *PZT* patch is analysed using voltage output at various embedment depths. The voltage output of the *PZT* patch increased as the frequency of excitation was increased from 10-80 Hz (Fig. 5.7). The highest voltage output was observed at 60 Hz, which was 7.5 mV. Similarly, it is observed that strain sensitivity is maximum for a thickness ratio of 0.5 at an excitation frequency of 60 Hz.

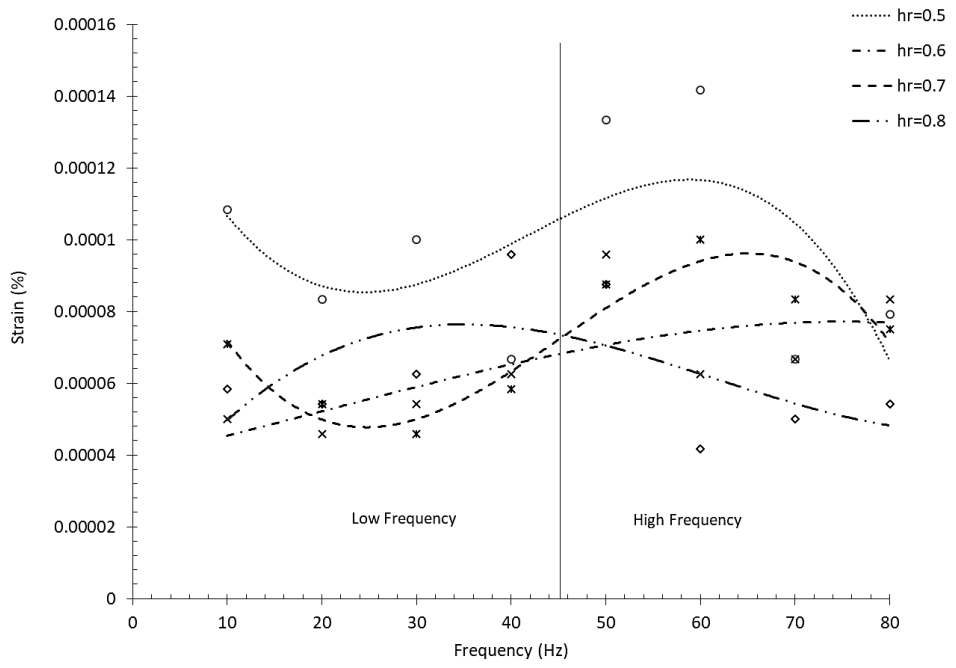

Fig. 6.1 The strain in embedded *PZT* patch at varied excitation frequencies with different depth ratios (h_r)

It is observed that the strain values tend to increase as the excitation frequency increases, reaching a peak value and then decreasing again. This behavior can be attributed to the resonant

frequency of the *PZT* patch. As the excitation frequency approaches the resonant frequency, the strain increase due to the increased energy transfer to the *PZT* patch. However, as the excitation frequency moves away from the resonant frequency, the strain values decrease due to reduced energy transfer.

Therefore, it is important to select an excitation frequency close to the resonant frequency of the *PZT* patch to achieve maximum strain. Additionally, the resonant frequency of the *PZT* patch can be influenced by its size and material properties of confined granular fill. At a fixed excitation frequency, the maximum strain is observed at the depth ratio 0.5. However, the strain decreases for higher depth ratios (0.8-1.0).

6.4.2 Effect of Embeddment Depth on Strain Sensitivity

It is observed from Fig. 6.2 that as the embedment depth of the PZT patch increases, the strain values initially decrease. However, they reach a minimum point at a certain depth and then begin to increase again. The relationship between depth ratio and *PZT* output at varying excitation frequencies followed an empirical law as,

$$S_f = \alpha h_r^2 - \beta h_r + \gamma \qquad (6.1)$$

where α, β and γ are the fitting parameters that vary with varying excitation frequencies with various depth ratios. S_f is strain at varied excitation frequencies. h_r is depth ratio. The quadratic relationship between the strain and embedment depth shows that a small change in depth can lead to a significant change in strain. However, as the embedment depth increases, the negative linear term begins to dominate, causing the strain value to decrease. This implies that beyond a certain depth, further increasing the embedment depth leads to a reduction in strain. This can be due to the difference in the mass and confinement of granular fill above the *PZT* patch at each depth ratio.

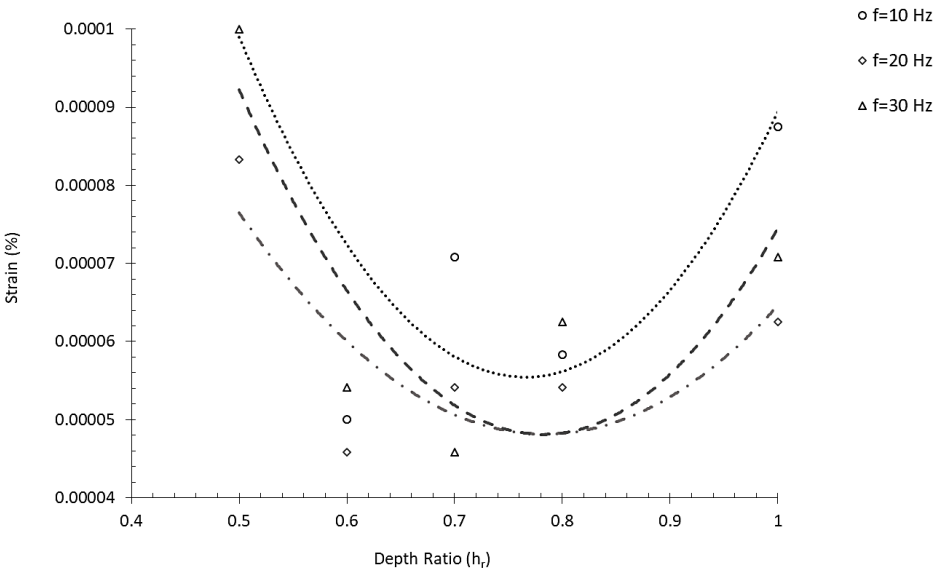

Fig. 6.2 The strain with depth ratio at excitation frequencies ranging from 10 to 30 Hz

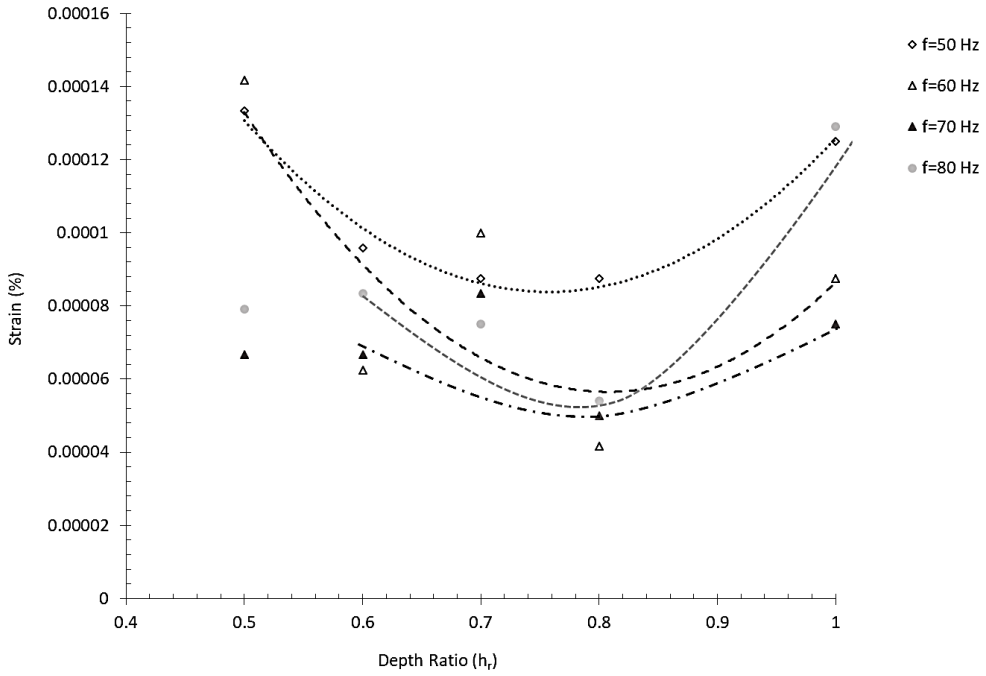

Fig. 6.3 The strain with depth ratio at excitation frequencies ranging from 50 to 80 Hz

6.4.3 Effect of Excitation Frequency on Power and Energy Output

Fig. 6.3 shows the power and energy output of *PZT* patches embedded at various depth ratios in confined granular fill. It is observed that depth ratio and excitation frequency significantly influence the power and energy output of *PZT* patches.

In terms of excitation frequency, it has been observed that the power output increases with an increase in frequency up to a certain point, after which it starts to decrease. At a depth ratio of 0.5, the power output increases from 1 to 8.49 Watts at an excitation frequency in the range of 10-50 Hz. For excitation frequency of more than 50 Hz, the power output decreases to 4.79. It indicates that the energy transfer or consumption rate is relatively slow during embedded *PZT* patches at a low frequency range.

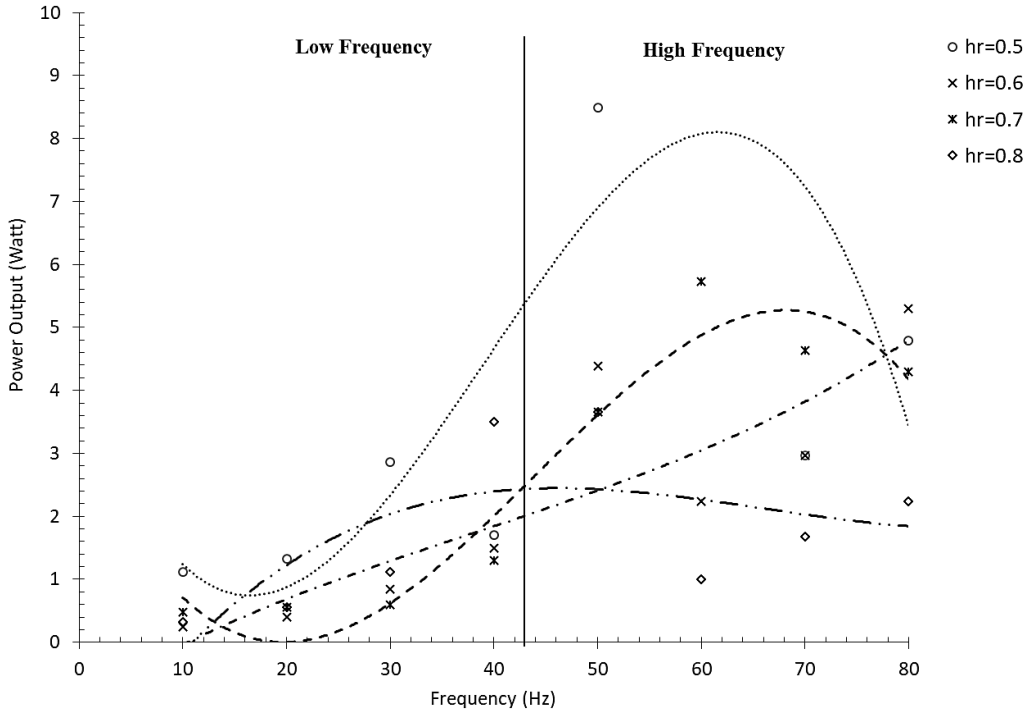

Fig. 6.4 The power output from *PZT* patch at varied excitation frequencies with different depth ratios (h_r)

The results indicate that the energy output of the *PZT* patch is highly dependent on the excitation frequency and depth ratio, as shown in Fig. 6.5. At low excitation frequencies (10-

40 Hz), the energy output is highest for the depth ratio of 0.5, with decreasing energy output as the depth ratio increases. It shows that despite the low rate of energy transmission (low power output), the total amount of energy transferred over the duration is high. The observed phenomenon of low power output and higher energy output from the *PZT* patch within the excitation frequency range of 10 to 40 Hz can be attributed to the properties of the *PZT* patch and confined granular fill. The *PZT* patch exhibits enhanced energy storage capacity or efficiency at frequencies within this range. Consequently, despite the relatively low power output, the *PZT* patch can deliver a higher total energy output.

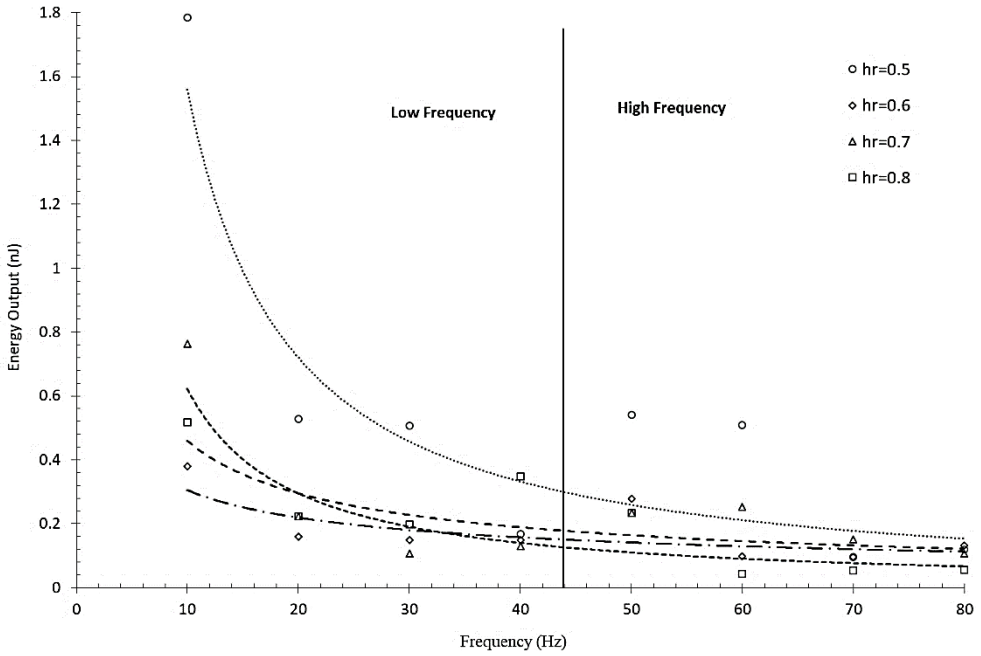

Fig. 6.5 The energy output from *PZT* patch at varied excitation frequencies with different depth ratios (h_r)

6.4.4 Effect of Embedment Depth on Power and Energy Output

This section represents the power (Watt) and energy output (nJ) from a *PZT* patch embedded in confined granular fill at different depth ratios. The depth ratio refers to the ratio of the depth of the *PZT* patch in the confined granular fill to the depth of the fill.

As the depth ratio (h_r) increases, the energy output decreases for low excitation frequencies (Fig. 6.6). The energy output is observed in the range of 0.1 to 1.8 nJ for depth ratios 0.5 to 1. As discussed in the previous section, the energy output is low at varied embedment depths for high frequencies.

Fig. 6.7 shows that the energy output is in the range of 0.1 to 0.6 nJ. This is because the *PZT* patch experiences greater confinement and the surrounding granular fill impedes its ability to vibrate, decreasing energy output. Additionally, the density of granular fill and particle size distribution affects the energy output pattern.

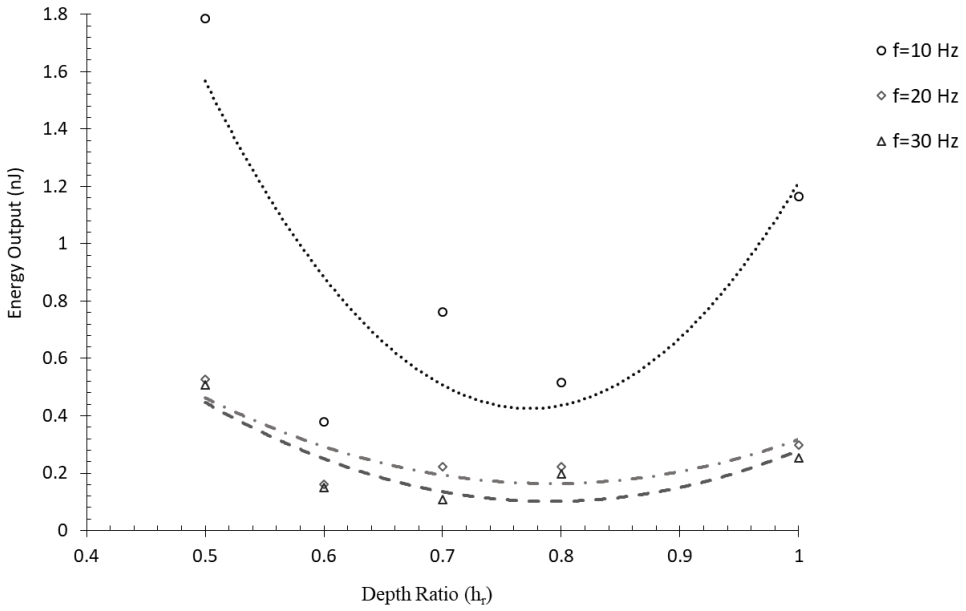

Fig. 6.6 The energy output variation with depth ratio at excitation frequency ranging from 10 to 30 Hz

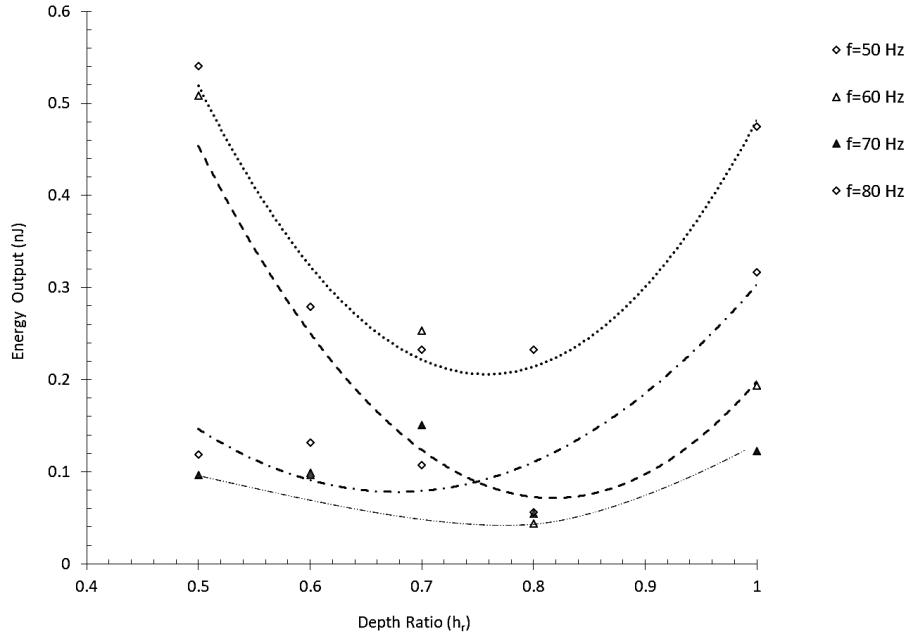

Fig. 6.7 The energy output with depth ratio at excitation frequencies ranging from 50 to 80 Hz

Fig. 6.8 shows the power output variation of the *PZT* patch at varied embedment depths. At depth ratios of 0.5-1, the power output is 0.5-14 watts.

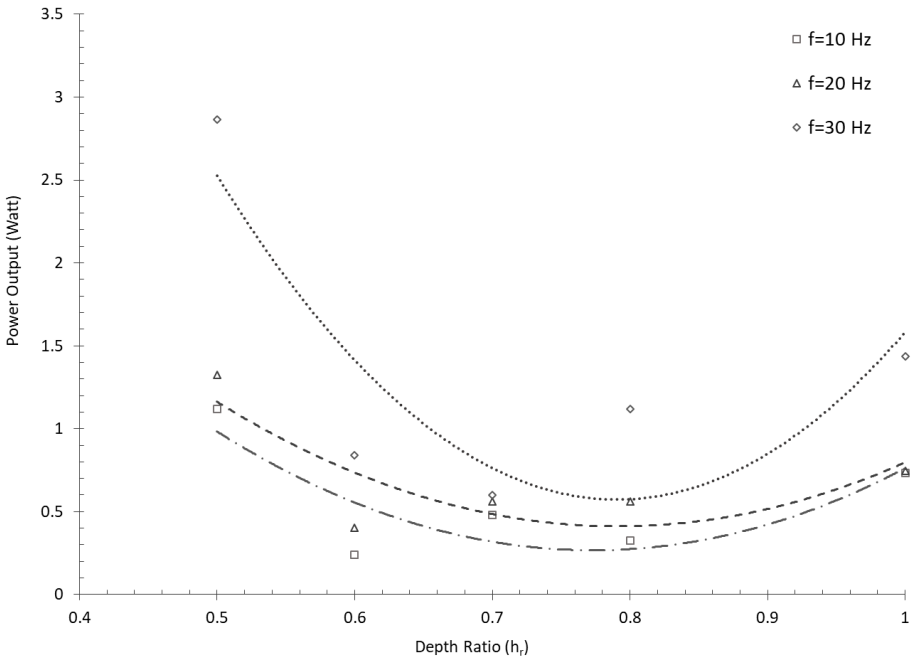

Fig. 6.8 The power output with depth ratio at excitation frequencies ranging from 10 to 30 Hz

The observed trend of power output with depth ratio can be attributed to the strain sensitivity of the *PZT* patch. As the strain reduces with depth, the power output reduces correspondingly.

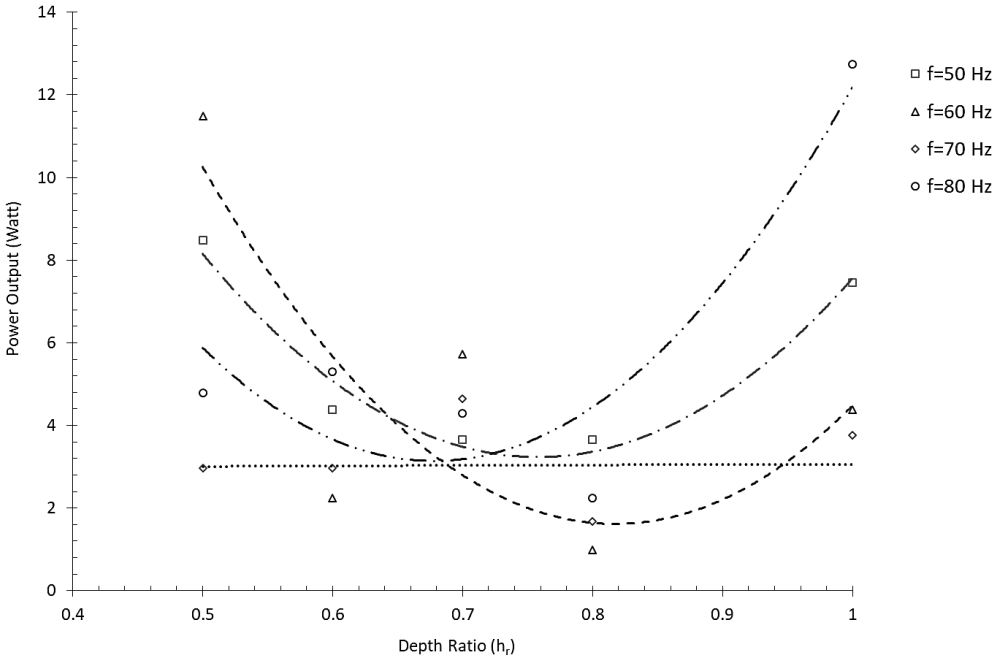

Fig. 6.9 The power output with depth ratio at excitation frequencies ranging from 50 to 80 Hz

The piezoelectric effect can explain the relationship between voltage, strain sensitivity, energy, and power output. When mechanical vibrations are applied to the *PZT* patch, it causes a deformation, generating a voltage across the patch. This voltage is proportional to the applied frequency and the deformation, which is related to the strain and energy output in the *PZT* patch.

The observed data of strain, energy and power output of a *PZT* patch embedded in confined granular fill can be explained in terms of depth ratio and excitation frequency (Eq. 6.2-6.4). The relationship between the excitation frequency and *PZT* output at varying depth ratios followed an empirical law as,

$$S_{hr} = \alpha_1 f^2 + \beta_1 f + \gamma_1 \qquad (6.2)$$

$$E_{hr} = \alpha_2 f^{\beta_2} \qquad (6.3)$$

$$P_{hr} = \alpha_3 f^2 + \beta_3 f + \gamma_3 \qquad (6.4)$$

where α, β and γ are the fitting parameters that vary with varying depth ratios at various excitation frequencies. f is the excitation frequency in Hz. The strain S_{h_r} is expressed in percentage. The energy E_{h_r} and power output P_{h_r} are expressed in nJ and Watt, respectively.

Table 6.1 Fitting parameters α, β and γ for strain, energy and power output at varying depth ratios.

Depth Ratio (h_r)	Strain Output (S_{hr})			Energy Output (E_{hr})		Power Output (P_{hr})		
	α_1	β_1	γ_1	α_2	β_2	α_3	β_3	γ_3
0.5	$-2x10^{-08}$	$1x10^{-06}$	$8x10^{-05}$	20.3	-1.115	-0.0029	0.338	-3.539
0.6	$-6x10^{-09}$	$1x10^{-06}$	$4x10^{-05}$	0.919	-0.479	0.0002	0.0469	-0.416
0.7	$-5x10^{-10}$	$5x10^{-07}$	$5x10^{-05}$	2.012	-0.641	-0.0003	0.1047	-1.275
0.8	$-2x10^{-08}$	$2x10^{-06}$	$4x10^{-05}$	7.409	-1.076	-0.0013	0.1399	-1.205

Eq. 6.2 illustrates that strain is influenced by excitation frequency through both quadratic and linear terms. Eq. 6.3 indicates that energy output decreases with increasing excitation frequency, following an inverse power relationship. Eq.6.4 demonstrates that power output is affected by excitation frequency with a quadratic and linear dependence. The constant terms α, β and γ in each equation contribute to the baseline and are presented in Table 6.1. These equations allow for a quantitative understanding of how strain, energy, and power output of embedded *PZT* patches are interconnected and influenced by excitation frequency and confined granular fills. Understanding these relationships allows for a comprehensive analysis of the behavior and performance of the *PZT* patch embedded in the confined granular fill, considering the impact of the excitation frequency and depth ratio on strain, energy, and power output.

Chapter 7

Conclusions and Future Recommendations

This chapter presents the conclusions of the research work focused on the dynamic response analysis of confined granular fill with PZT patches. Finally, it makes some recommendations for future research based on the experience from this research.

7.1 Conclusions

This research focused on the dynamic response analysis of confined granular fill with *PZT* patches. The investigation aimed to understand the behavior of embedded *PZT* patches under dynamic loading conditions due to ambient mechanical vibrations of geo-structures. Dynamic loading, characterized by the application of different excitation frequencies, was utilized to induce stress and strain within the *PZT* patches and the wall retaining granular fill. The dynamic response analysis involved studying the changes in stress and strain exhibited by these components in response to varying excitation frequencies. By analyzing the dynamic response characteristics, including stress and strain distribution, this study provided valuable insights into the dynamic behavior of the confined granular fill and *PZT* patches. The findings of this research enhance the knowledge and offer practical implications for optimizing the performance of *PZT* patches in a wide range of applications within geo-structures.

A quantitative estimate of piezoelectric voltage output depends upon the stress-strain response of confined granular fill, retaining structure and *PZT* patches. The dynamic loads affect the stress distribution in the confined granular fill and PZT patch. The confined granular fill with a set of *PZT* patches has been considered to evaluate charge density and voltage output. The effect of the modulus ratio, alignment of the *PZT* patch, and thickness ratio have been investigated.

The coupling of geo-structures and *PZT* patch is significantly affected by fundamental frequency, the contact mechanism of loading, the geometry and material characteristics of the geo-structure, moving load frequency, and dynamic response. The embedment of the *PZT* in geo-material affects polarization and voltage output.

It provides a framework for evaluating power outputs from confined granular fill and improving the conversion efficiency from the strain fluctuations, polarization per unit permittivity and geometric properties, which play a significant role in the health monitoring and behaviour of geo-structures. The observed voltage output is found appropriate for wide-ranging applications. It is proposed to be up-scaled using multiple patches embedded throughout the confined granular fill subjected to continuous dynamic loads.

Experimental investigation shows the effect of the confined granular soil on the efficiency of the *PZT* patches under various exciting frequencies. The dynamic response of experimental data has been analysed using *FFT*. The peak pick method has been used to analyse the natural frequency of the system. An analysis of the influence of excitation frequency and embedment depth on the voltage output of *PZT* patches. Further, static cone penetration tests have been carried out to monitor the effect of confinement under various excitation frequencies.

The significant findings, conclusions, and suggestions from this study are summarised below:

- The stress-strain plots are obtained for varying thickness ratios of the *PZT* patch and wall retaining granular fill. Average stress in the *PZT* layer increases when the modulus ratio increases. The strain in the *PZT* patch is proportional to the strain in the wall retaining granular fill. These findings suggest that the choice of backfill material for the wall retaining granular fill can significantly impact
- The properties of granular material, geometrical dimensions of the confined granular fill and the properties of the *PZT* patch significantly influence the stress-strain

behaviour, which influences the voltage output from the *PZT* patch. The maximum voltage output was obtained for the thickness ratio of 0.2–0.6. The voltage output for the horizontally and vertically embedded *PZT* patches is obtained in the range of 0.01–0.5 V and 0.001–0.06 V, respectively.

- The natural frequency and damping loss factor of the dynamically loaded confined granular fill influence the voltage output of the *PZT* patch. The natural frequency of the soil–wall system has been found to decrease with the increasing thickness ratio. At a maximum natural frequency (49 Hz), the output voltage was obtained in the range of 2.0-3.2 V. For the maximum damping loss factor (0.176), the output voltage was obtained in the range of 1.5-3.0 V.
- The experimental results indicate that voltage output from the *PZT* patch depends on the excitation frequency and placement of the *PZT* patch. The position of embedment of the *PZT* patch in the confined granular fill affects the voltage output efficiency. For the same embedment depth, the peak voltage output in the vertical direction is observed at 50 Hz, while the transverse direction is obtained at 10 Hz. To get the maximum efficiency of the *PZT* patch as an energy harvester, it should be centrally embedded for vertical vibrations.
- The voltage output from vertically and horizontally embedded *PZT* patches (1.3-2.3 V and 0.8-2.4 V) was obtained for the range of cone resistance 456-571 kPa. The cone resistance indicates the confinement and compaction level of the granular fill. It suggests that as the granular fill becomes denser and exhibits higher cone resistance, the voltage output from vertically and horizontally embedded *PZT* patches increases. This correlation between cone resistance and voltage output highlights the significance of granular fill compaction in optimizing the efficiency of the *PZT* patch.
- The cone resistance (up to 900 kPa) at various penetration depths indicates that voltage

output increased proportionally with the cone resistance at varied excitation frequencies. For varied excitation frequencies (f=40-50 Hz), the voltage output increases in the range of 22-45%. The densification of fill and consequent increase in the cone resistance has a significant impact on improving the efficiency of the *PZT* patch.

- The strain values in the *PZT* patch increase with increased excitation frequency. The strain values vary with different depth ratios, with increased strain values observed at lower depth ratios (0.5 to 0.7) and decreased strain values observed at higher depth ratios (0.8 to 1.0). The strain sensitivity of the *PZT* patch can be maximized by operating at higher excitation frequencies and embedding the patch in deeper granular fill. This can lead to an increase in the energy output of the *PZT* patch and can thus improve the overall efficiency of the energy harvesting system.
- The depth ratio and excitation frequency significantly affect the power output from *PZT* patches embedded in confined granular fill. At depth ratios of 0.5-1, the power output is 0.5-14 watts. The study highlights the importance of optimizing the depth ratio and excitation frequency to maximize power generation from *PZT* patches in practical applications.

7.2 Future Recommendations

Future recommendations of this study include further investigation of the effects of the water table, soil strata, piezoelectric properties, temperature, pavement material, vehicle speed and type of moving loads on the voltage output, strain sensitivity and energy output of *PZT* patches. Additionally, the performance of *PZT* patches can be further optimized by designing the shape and size of the patches. Furthermore, the integration of *PZT* patches with energy harvesting technologies can be considered to improve the overall energy output. An investigation may be required to fully understand the complex relationship between the excitation frequency, depth

of granular fill, and strain sensitivity of *PZT* patches. Nevertheless, the results of this study shall provide valuable insights into the behavior of *PZT* patches in confined granular fill and shall be useful to the design of energy harvesting systems.

REFERENCES

1. Ahmad, S., Abdul Mujeebu, M., & Farooqi, M. A. (2019). Energy harvesting from pavements and roadways: A comprehensive review of technologies, materials, and challenges. International Journal of Energy Research, 43(6), 1974-2015.
2. Ai, D., Zhu, H., Luo, H., & Yang, J. (2014). An effective electromechanical impedance technique for steel structural health monitoring. Construction and Building Materials, 73, 97-104.
3. Ali, S., Friswell, M., & Adhikari, S. (2011). Analysis of energy harvesters for highway bridges. Journal of Intelligent Material Systems and Structures, 22(16), 1929-1938.
4. Amini, Y., Heshmati, M., Fatehi, P., & Habibi, S. E. (2017). Energy harvesting from vibrations of a functionally graded beam due to moving loads and moving masses. Journal of Engineering Mechanics, 143(9), 04017063.
5. Anton, S. R., & Sodano, H. A. (2007). A review of power harvesting using piezoelectric materials (2003–2006). Smart materials and Structures, 16(3).
6. Ashebo, D. B., Tan, C. A., Wang, J., & Li, G. (2008). Feasibility of energy harvesting for powering wireless sensors in transportation infrastructure applications. Paper presented at the Nondestructive Characterization for Composite Materials, Aerospace Engineering, Civil Infrastructure, and Homeland Security.
7. Bahador, S. D., & Yaowen, Y. (2010). Monitoring hydration of concrete with piezoelectric transducers. In 35th Conference on Our World in Concrete & Structures, Singapore.
8. Banerjee, S., & Cook-Chennault, K. A. (2014). Influence of aluminium inclusions on dielectric properties of three-phase *PZT*–cement–aluminium composites. Advances in Cement Research, 26(2), 63-76.

9. Bathurst, R. J., & Hatami, K. (1998). Seismic response analysis of a geosynthetic reinforced soil retaining wall. Geosynthetics International, 5(1-2), 127-166.
10. Beeby, S. P., Torah, R. N., Tudor, M. J., Glynne-Jones, P., O'donnell, T., Saha, C. R., & Roy, S. (2007). A micro electromagnetic generator for vibration energy harvesting. Journal of Micromechanics and Microengineering. 17(7), 1257.
11. Beeby, S. P., Tudor, M. J., White, & N. M. (2006). Energy harvesting vibration sources for microsystems applications. Measurement Science and Technology, 17(12), R175.
12. Bhalla, S., & Soh, C. K. (2004). Structural health monitoring by piezo-impedance transducers. I: Modeling. Journal of Aerospace Engineering, 17(4), 154-165.
13. Bonello, P., & Rafique, S. (2011). Modeling and analysis of piezoelectric energy harvesting beams using the dynamic stiffness and analytical modal analysis methods. Journal of Vibration and Acoustics, 133(1).
14. Cahill, P., Mathewson, A., & Pakrashi, V. (2018). Experimental Validation of Piezoelectric Energy-Harvesting Device for Built Infrastructure Applications. Journal of Bridge Engineering, 23(8).
15. Cahill, P., Mathewson, A., & Pakrashi, V. (2018). Experimental validation of piezoelectric energy-harvesting device for built infrastructure applications. Journal of Bridge Engineering, 23(8), 04018056.
16. Cahill, P., Nuallain, N. A. N., Jackson, N., Mathewson, A., Karoumi, R., & Pakrashi, V. (2014). Energy harvesting from train-induced response in bridges. Journal of Bridge Engineering, 19(9), 04014034.
17. Chaipanich, A. (2007). Dielectric and piezoelectric properties of *PZT*–silica fume cement composites. Current Applied Physics, 7(5), 532-536.

18. Chaipanich, A., & Jaitanong, N. (2008). Effect of poling time on piezoelectric properties of 0-3 *PZT*-portland cement composites. Ferroelectric Letters, 35(3-4), 73-78.
19. Chen, F., Balieu, R., Córdoba, E. & Kringos, N. (2019). Towards an understanding of the structural performance of future electrified roads: a finite element simulation study. International Journal of Pavement Engineering, 20(2), 204-215.
20. Chen, F., Taylor, N., Balieu, R., & Kringos, N. (2017). Dynamic application of the Inductive Power Transfer (IPT) systems in an electrified road: Dielectric power loss due to pavement materials. Construction and Building Materials 147, 9-16.
21. Chen, Y., & Xue, X. J. S. (2018). Advances in the structural health monitoring of bridges using piezoelectric transducers. Sensors, 18(12), 4312.
22. Chen, Y., Zhang, H., Zhang, Y., Li, C., Yang, Q., Zheng, H., & Lü, C. (2016). Mechanical energy harvesting from road pavements under vehicular load using embedded piezoelectric elements. Journal of Applied Mechanics, 83(8).
23. Chopra, I. (2002). Review of state of art of smart structures and integrated systems. AIAA Journal, 40(11), 2145-2187.
24. Cunefare, K. A., Skow, E. A., Erturk, A., Savor, J., Verma, N., & Cacan, M. R. (2013). Energy harvesting from hydraulic pressure fluctuations. Smart Materials and Structures, 22(2), 025036.
25. Cveticanin, L., Zukovic, M., & Cveticanin, D. (2017). Non-ideal source and energy harvesting. Acta Mechanica, 228(10), 3369-3379.
26. Divsholi, B. S., & Yang, Y. (2010). Monitoring hydration of concrete with piezoelectric transducers. In Proceedings of the 35th Conference on Our World in Concrete & Structures.

27. Dong, B., & Li, Z. (2005). Cement-based piezoelectric ceramic smart composites. Composites Science Technology, 65(9), 1363-1371.
28. Duarte, F., Ferreira, A., & Fael, P. (2018). Road Pavement Energy–Harvesting Device to Convert Vehicles' Mechanical Energy into Electrical Energy. Journal of Energy Engineering, 144(2).
29. DuToit, N. E., & Wardle, B. L. (2007). Experimental verification of models for microfabricated piezoelectric vibration energy harvesters. AIAA journal, 45(5), 1126-1137.
30. Dwivedi, A., Banerjee, A., & Bhattacharya, B. (2020). Simultaneous energy harvesting and vibration attenuation in piezo-embedded negative stiffness metamaterial. Journal of Intelligent Material Systems and Structures, 31(8), 1076-1090.
31. Elvin, N. G., Lajnef, N., & Elvin, A. A. (2006). Feasibility of structural monitoring with vibration powered sensors. Smart Materials and Structures, 15(4), 977-986.
32. Erturk, A. (2011). Piezoelectric energy harvesting for civil infrastructure system applications: Moving loads and surface strain fluctuations. Journal of Intelligent Material systems and structures, 22(17), 1959-1973.
33. Erturk, A. (2011). Piezoelectric energy harvesting for civil infrastructure system applications: Moving loads and surface strain fluctuations. Journal of Intelligent Material Systems and Structures, 22(17), 1959-1973.
34. Erturk, A., & Inman, D. J. (2008). On Mechanical Modeling of Cantilevered Piezoelectric Vibration Energy Harvesters. Journal of Intelligent Material Systems and Structures, 19(11), 1311-1325.
35. Erturk, A., & Inman, D. J. (2009). An experimentally validated bimorph cantilever model for piezoelectric energy harvesting from base excitations. Smart Materials and Structures, 18(2), 025009.

36. Galchev, T., McCullagh, J., Peterson, R., & Najafi, K. (2011). Harvesting traffic-induced vibrations for structural health monitoring of bridges. Journal of Micromechanics Microengineering, 21(10), 104005.
37. Gammaitoni, L., Neri, I., & Vocca, H. (2009). Nonlinear oscillators for vibration energy harvesting. Applied Physics Letters, 94(16), 164102.
38. García-Olivares, A., Solé, J., & Osychenko, O. (2018). Transportation in a 100% renewable energy system. Energy Conversion and Management, 158, 266-285.
39. Ghafari, E., Yuan, Y., Wu, C., Nantung, T., & Lu, N. (2018). Evaluation the compressive strength of the cement paste blended with supplementary cementitious materials using a piezoelectric-based sensor. Construction and Building Materials, 171, 504-510.
40. Glynne-Jones, P., Tudor, M. J., Beeby, S. P., & White, N. M. (2004). An electromagnetic, vibration-powered generator for intelligent sensor systems. Sensors and Actuators A: Physical. 110(1-3), 344-349.
41. Gong, H., Li, Z., Zhang, Y., & Fan, R. (2009). Piezoelectric and dielectric behavior of 0-3 cement-based composites mixed with carbon black. Journal of the European Ceramic Society, 29(10), 2013-2019.
42. Gong, H., Zhang, Y., Quan, J., & Che, S. (2011). Preparation and properties of cement based piezoelectric composites modified by CNTs. Current Applied Physics, 11(3), 653-656.
43. Green, P. L., Papatheou, E., & Sims, N. D. (2013). Energy harvesting from human motion and bridge vibrations: An evaluation of current nonlinear energy harvesting solutions. Journal of Intelligent Material Systems and Structures, 24(12), 1494-1505.

44. Gu, H., Song, G., Dhonde, H., Mo, Y., & Yan, S. (2006). Concrete early-age strength monitoring using embedded piezoelectric transducers. Smart Materials and Structures, 15(6), 1837.
45. Guo, L., & Lu, Q. (2017). Modeling a new energy harvesting pavement system with experimental verification. Applied Energy 208, 1071-1082.
46. Guo, L., & Lu, Q. (2017). Potentials of piezoelectric and thermoelectric technologies for harvesting energy from pavements. Renew Sustainable Energy Reviews 72, 761-773.
47. Hill, D., Agrawal, A., & Tong, N. (2013). Assessment of Piezoelectric Materials for Roadway Energy Harvesting, Report prepared by DNV KEMA Energy and Sustainability Inc. for the California Energy Commission. Publication Number: CSC-500-2013-007.
48. IEEE (The Institute of Electrical and Electronics Engineering) (1988). Standard on piezoelectricity. ANSI/IEEE Std. 176-1987. New York.
49. Islam, R. A., & Priya, S. (2006). Realization of high-energy density polycrystalline piezoelectric ceramics. Applied Physics Letter 88(3), 032903.
50. Jamshidi, R., Towhata, I., Ghiassian, H., & Tabarsa, A. R. (2010). Experimental evaluation of dynamic deformation characteristics of sheet pile retaining walls with fiber reinforced backfill. Soil Dynamics and Earthquake Engineering, 30(6), 438-446.
51. Jaitanong, N., Yimnirun, R., Zeng, H., Li, G., Yin, Q., & Chaipanich, A. (2014). Piezoelectric properties of cement based/PVDF/*PZT* composites. Materials Letters, 130, 146-149.
52. Jasim, A. F., Wang, H., Yesner, G., Safari, A., & Szary, P. (2019). Performance analysis of piezoelectric energy harvesting in pavement: laboratory testing and field simulation. Transportation Research Record, 2673(3), 115-124.

53. Jasim, A., Wang, H., Yesner, G., Safari, A., & Maher, A. (2017). Optimized design of layered bridge transducer for piezoelectric energy harvesting from roadway. Energy, 141, 1133-1145.
54. Jiang, X., Li, Y., Li, J., Wang, J., & Yao, J. (2014). Piezoelectric energy harvesting from traffic-induced pavement vibrations. Journal of Renewable Sustainable Energy, 6(4), 043110.
55. Jiang, Z., Cai, J., & Moses, P. S. (2020). Smoothing control of solar photovoltaic generation using building thermal loads. Applied Energy. 277, 115523.
56. Jing-Song, S., Xiao-Ming, H., & Gong-Yun, L. (2007). Dynamic response analysis of pavement structure under moving load. Journal of Highway Transportation Research and Development, 1(130).
57. Jung, H. J., Kim, I. H., & Jang, S. J. (2011). An energy harvesting system using the wind-induced vibration of a stay cable for powering a wireless sensor node. Smart Materials and Structures, 20(7), 075001.
58. Karimi, M., Karimi, A., Tikani, R., & Ziaei-Rad, S. (2016). Experimental and theoretical investigations on piezoelectric-based energy harvesting from bridge vibrations under travelling vehicles. International Journal of Mechanical Sciences, 119, 1-11.
59. Kerboua, M., Benguediab, M., Megnounif, A., Benrahou, K. H., & Kaoulala, F. (2014). Semi active control of civil structures, analytical and numerical studies. Physics Procedia, 55, 301-306.
60. Khiem, N. T., Hai, T. T., & Huong, L. Q. (2020). Effect of piezoelectric patch on natural frequencies of Timoshenko beam made of functionally graded material. Materials Research Express, 7(5), 055704.

61. Kim, H. W., Batra, A., Priya, S., Uchino, K., Markley, D., Newnham, R. E., & Hofmann, H. F. (2004). Energy harvesting using a piezoelectric "cymbal" transducer in dynamic environment. Japanese Journal of Applied Physics, 43(9R), 6178.
62. Kim, S. W., Jeon, B. G., Kim, N. S., Park, J. C. (2013). Vision-based monitoring system for evaluating cable tensile forces on a cable-stayed bridge. Structural Health Monitoring 12(5-6), 440-456.
63. Kim, S.H., Ahn, J.H., Chung, H.M., & Kang, H.W. (2011). Analysis of piezoelectric effects on various loading conditions for energy harvesting in a bridge system. Sensors and Actuators A: Physical, 167(2), 468-483.
64. Kumari, N., & Trivedi, A. (2020). Semi-active Control Strategy for Horizontal Dynamic Loading on Wall Retaining Granular Fills. In Sustainable Civil Engineering Practices, (71-79). Springer, Singapore.
65. Kumari, N., & Trivedi, A. (2018). Application of Semi-Active Control Strategy for The Wall Retaining Granular Fills. Proceeding of China-Europe Conference on Geotechnical Engineering, SSGG, Springer, 978-982.
66. Kumari, N., & Trivedi, A. (2020). Vibration Control of Flexible Retention Systems. Advances in Computer Methods and Geomechanics, Lecture Notes in Civil Engineering, Springer, Singapore, 2(56), 529-539.
67. Kumari, N., & Trivedi, A. (2022). A Review on Modelling and Techniques Used for Piezoelectric Power Generation from Vibration of Geo-Structures. E-Prime-Advances in Electrical Engineering, Electronics and Energy, 100076 (2022).
68. Kumari, N., & Trivedi, A. (2022). Factors Influencing Piezoelectric Response of Horizontally and Vertically Embedded *PZT* Patch in Confined Granular Fills. Advances in Material Science and Engineering.

69. Kumari, N., & Trivedi, A. (2022). The Effect of Confined Granular Soil on Embedded *PZT* Patches Using FFT and Digital Static Cone Penetrometer (DSCP). Applied Sciences, 12, 9711
70. Lam, K. H., & Chan, H. (2005). Piezoelectric cement-based 1-3 composites. Applied Physics A, 81(7), 1451-1454.
71. Li, H., Tian, C., & Deng, Z. D. (2014). Applied Physics Reviews. Applied Physics Letter, 113904, 104.
72. Li, L., Xu, J., Liu, J., & Gao, F. (2018). Recent progress on piezoelectric energy harvesting: structures and materials. Advanced Composite Materials, 1(3), 478-505.
73. Li, X., Strezov, V. (2014). Modelling piezoelectric energy harvesting potential in an educational building. . Energy Conversion and Management 85, 435-442.
74. Li, Z., Gong, H., & Zhang, Y. (2009). Fabrication and piezoelectricity of 0–3 cement based composite with nano-*PZT* powder. Current Applied Physics, 9(3), 588-591.
75. Li, Z., Huang, S., Qin, L., & Cheng, X. (2007). An investigation on 1–3 cement based piezoelectric composites. Smart Materials and Structures, 16(4), 999.
76. Li, Z., Zhang, D., & Wu, K. (2002). Cement-based 0-3 piezoelectric composites. Journal of the American Ceramic Society, 85(2), 305-313.
77. Liu, P., Zhao, Q., Yang, H., Wang, D., Oeser, M., Wang, L., Tan, Y. (2019). Numerical study on influence of piezoelectric energy harvester on asphalt pavement structural responses. Journal of Materials in Civil Engineering. 31, 04019008.
78. Lv, J.-f., Yang, K., Sun, L., Chen, W.-h., & Tan, Y.-q. (2015). Finite element analysis of piezoelectric stack transducer embedded in asphalt pavement. Paper presented at the Symposium on Piezoelectricity, Acoustic Waves, and Device Applications (SPAWDA).

79. Lynch, J. P. (2007). An overview of wireless structural health monitoring for civil structures. Philosophical Transactions of the Royal Society A: Mathematical, Physical Engineering Sciences, 365(1851), 345-372.
80. Mann, B., & Owens, B. (2010). Investigations of a nonlinear energy harvester with a bistable potential well. Journal of Sound and Vibration, 329(9), 1215-1226.
81. Mateu, L., & Moll, F. (2005). Review of energy harvesting techniques and applications for microelectronics. In VLSI Circuits and Systems II (5837), 359-374. International Society for Optics and Photonics.
82. Meitzler, A., Tiersten, H., Warner, A., Berlincourt, D., Couqin, G., & Welsh III, F. (1988). IEEE Standard on Piezoelectricity. IEEE Ultrasonics, Ferroelectrics, and Frequency Control Society. 176-1987
83. Moure, A., Rodríguez, M. I., Rueda, S. H., Gonzalo, A., Rubio-Marcos, F., Cuadros, & D. U., Fernández, J. (2016). Feasible integration in asphalt of piezoelectric cymbals for vibration energy harvesting. Energy Conversion and Management, 112, 246-253.
84. Murray, R., & Rastegar, J. (2009). Novel two-stage piezoelectric-based ocean wave energy harvesters for moored or unmoored buoys. In Active and Passive Smart Structures and Integrated Systems. International Society for Optical Engineering. 7288, 72880E.
85. Negi, P., Chhabra, R., Kaur, N., & Bhalla, S. (2019). Health monitoring of reinforced concrete structures under impact using multiple piezo-based configurations. Construction and Building Materials, 222, 371-389.
86. Newnham, R. E., & Ruschau, G. R. (1993). Electromechanical properties of smart materials. Journal of Intelligent Material Systems and Structures, 4(3), 289-294.

87. Nordmann, T., Froelich, A., Goetzberger, A., Kleiss, G., Hille, G., Reise, C., Castello, & S. (2020). The potential of PV noise barrier technology in Europe. In Sixteenth European Photovoltaic Solar Energy Conference, Routledge. 2912-2916.
88. Paradiso, J. A., & Starner, T. (2005). Energy scavenging for mobile and wireless electronics. IEEE Pervasive computing, 4(1), 18-27.
89. Park, G., Rosing, T., Todd, M. D., Farrar, C. R., & Hodgkiss, W. (2008). Energy harvesting for structural health monitoring sensor networks. Journal of Infrastructure Systems 14(1), 64-79.
90. Patzák, B. (2012). OOFEM—an object-oriented simulation tool for advanced modeling of materials and structures. Acta Polytechnica, 52(6).
91. Peigney, M., & Siegert, D. (2013). Piezoelectric energy harvesting from traffic-induced bridge vibrations. Smart Materials and Structures, 22(9), 095019.
92. Petroff, C. A., Bina, T. F., & Hutchison, G. R. (2019). Highly tunable molecularly doped flexible poly (dimethylsiloxane) foam piezoelectric energy harvesters. ACS Applied Energy Materials, 2(9), 6484-6489.
93. Physik Instrumente (PI) GmbH, Co. KG. CAT 125E R3 Piezoelectric Ceramic Products (2011).
94. Qi, K.-q., Xiang, Y., Fang, C., Zhang, Y., & Yu, C.-s. (2015). Analysis of the displacement amplification ratio of bridge-type mechanism. Mechanism Machine Theory, 87, 45-56.
95. Ren, X. (2004). Large electric-field-induced strain in ferroelectric crystals by point-defect-mediated reversible domain switching. Nature Material, 3(2), 91.
96. Rezaei-Hosseinabadi, N., Tabesh, A., Dehghani, R., Aghili, A. (2014). An efficient piezoelectric windmill topology for energy harvesting from low-speed air flows. IEEE Industrial Electronics Magazine, 62(6), 3576-3583.

97. Rhimi, M., & Lajnef, N. (2012). Tunable Energy Harvesting from Ambient Vibrations in Civil Structures. Journal of Energy Engineering, 138(4), 185-193.

98. Rianyoi, R., Potong, R., Ngamjarurojana, A., & Chaipanich, A. (2016). Microstructure and electrical properties of 0-3 connectivity barium titanate− Portland cement composite with 40% barium titanate content. Ferroelectrics Letters Section, 43(1-3), 59-64.

99. Rong, H., & Zhifei, S. (2011). Exact analysis of 0-3 cement-based piezoelectric composites. Journal of Intelligent Material Systems and Structures, 22(3), 221-229.

100. Roshani H., Jagtap P., Dessouky S., Montoya A., & Papagiannakis AT. (2017). Theoretical and experimental evaluation of two roadway piezoelectric-based energy-harvesting prototypes. Journal of Materials in Civil Engineering. 30(2), 04017264.

101. Roshani, H., & Dessouky, S. (2015). Feasibility study to harvest electric power from highway pavements using laboratory investigation. Department of Civil and Environmental Engineering University of Texas at San Antonio.

102. Roshani, H., Dessouky, S., & Papagiannakis, A. (2017). Experimental Investigation of Energy Harvesting Prototypes for Asphalt Roadways. In Airfield and Highway Pavements 2017 (10-19).

103. Roshani, H., Dessouky, S., Montoya, A., & Papagiannakis, A. (2016). Energy harvesting from asphalt pavement roadways vehicle-induced stresses: A feasibility study. Applied Energy, 182, 210-218.

104. Roshani, H., Jagtap, P., Dessouky, S., Montoya, A., & Papagiannakis, A. (2018). Theoretical and experimental evaluation of two roadway piezoelectric-based energy harvesting prototypes. Journal of Materials in Civil Engineering, 30(2), 04017264.

105. Roundy, S., Wright, P. K., & Rabaey, J. (2003). A study of low level vibrations as a power source for wireless sensor nodes. Computer communications, 26(11), 1131-1144.

106. Sasaki, K., Osaki, Y., Okazaki, J., Hosaka, H., & Itao, K. (2005). Vibration-based automatic power-generation system. Microsystem Technologies, 11(8), 965-969.

107. Shanker, R., Bhalla, S., Gupta, A., & Praveen Kumar, M. (2011). Dual use of *PZT* patches as sensors in global dynamic and local electromechanical impedance techniques for structural health monitoring. Journal of Intelligent Material Systems and Structures, 22(16), 1841-1856.

108. Shen, B., Yang, X., & Li, Z. (2006). A cement-based piezoelectric sensor for civil engineering structure. Materials and Structures, 39(1), 37-42.

109. Shi, Z., & Wang, J. (2013). Dynamic analysis of 2-2 cement–based piezoelectric transducers. Journal of Intelligent Material Systems and Structures, 24(1), 99-107.

110. Singh, B., Varandani, D., & Mehta, B. R. (2013). Effect of conductive atomic force microscope tip loading force on tip-sample interface electronic characteristics: Unipolar to bipolar resistive switching transition. Applied Physics Letters, 103(5), 051604.

111. Singh, V., Meena, D., Sharma, H., Trivedi, A., & Singh, B. (2022). Investigating the role of chalcogen atom in the piezoelectric performance of PVDF/TMDCs based flexible nanogenerator. Energy & Environmental Science, 239, 122125.

112. Singh, V., Meena, D., Sharma, H., Trivedi, A., & Singh, B. (2022). Investigating the role of chalcogen atom in the piezoelectric performance of PVDF/TMDCs based flexible nanogenerator. *Energy*. 239, 122125.

113. Sodano, H. A., Inman, D. J., Park, & G. (2004). A review of power harvesting from vibration using piezoelectric materials. Shock and Vibration, 36(3), 197-206.

114. Soh, C. K., Tseng, K. K. H., Bhalla, S., & Gupta, A. (2000). Performance of smart piezoceramic patches in health monitoring of a RC bridge. Smart Materials and Structures, 9(4), 533-542.

115. Song, Y. (2019a). Finite-element implementation of piezoelectric energy harvesting system from vibrations of Railway Bridge. Journal of Energy Engineering, 145(2), 04018076.

116. Sousa, V. C., De M Anicézio, M., De Marqui Jr, C., & Erturk, A. (2011). Enhanced aeroelastic energy harvesting by exploiting combined nonlinearities: theory and experiment. Smart Material and Structures, 20(9), 094007.

117. Sun, C. H., Shang, G. Q., Zhang, Y. K., & Du, J. H. (2013). Designing piezoelectric harvesting unit from road vibration. Paper presented at the advanced materials research.

118. Sun, M., Li, Z., & Song, X. (2004). Piezoelectric effect of hardened cement paste. Cement and Concrete Composites, 26(6), 717-720.

119. Tawie, R., & Lee, H.-K. (2010). Monitoring the strength development in concrete by EMI sensing technique. Construction and Building Materials, 24(9), 1746-1753.

120. Tianchen, Y., Jian, Y., Ruigang, S., & Xiaowei, L. (2014). Vibration energy harvesting system for railroad safety based on running vehicles. Smart Materials and Structures, 23(12), 125046.

121. Trivedi, A., & Singh, S. (2004). Cone Resistance of Compacted Ash Fill. Journal of Testing and Evaluation, 32(6), 429-437.

122. Varadha, E., & Rajakumar, S. (2018). Performance improvement of piezoelectric materials in energy harvesting in recent days-a review. Journal of Vibroengineering, 20(7).

123.Wang, C., Zhao, J., Li, Q., & Li, Y. (2018). Optimization design and experimental investigation of piezoelectric energy harvesting devices for pavement. Applied Energy, 229, 18-30.

124.Wang, D. W., Mo, J. L., Wang, X. F., Ouyang, H., & Zhou, Z. R. (2018). Experimental and numerical investigations of the piezoelectric energy harvesting via friction-induced vibration. Energy Conversion and Management, 171, 1134-1149.

125.Wang, F., Wang, H., Song, Y., & Sun, H. (2012). High piezoelectricity 0–3 cement-based piezoelectric composites. Materials Letters, 76, 208-210.

126.Wang, H., Jasim, A., Chen, X. (2018). Energy harvesting technologies in roadway and bridge for different applications–A comprehensive review. Applied Energy. 212, 1083-1094.

127.Wang, J., Shi, Z., Xiang, H., & Song, G. (2015). Modeling on energy harvesting from a railway system using piezoelectric transducers. Smart Materials and Structures, 24(10), 105017.

128.Wei, C., & Jing, X. (2017). A comprehensive review on vibration energy harvesting: Modelling and realization. Renewable Sustainable Energy Reviews, 74, 1-18.

129.Wen, S., & Chung, D. (2002). Cement-based materials for stress sensing by dielectric measurement. Cement and Concrete Research, 32(9), 1429-1433.

130.Williams, C., & Yates, R. B. (1996). Analysis of a micro-electric generator for microsystems. Sensors and Actuators A: Physical, 52(1-3), 8-11.

131.Wischke, M., Masur, M., Kröner, M., & Woias, P. (2011). Vibration harvesting in traffic tunnels to power wireless sensor nodes. Smart Materials and Structures, 20(8), 085014.

132. Xiang, H. J., Wang, J. J., Shi, Z. F., & Zhang, Z. W. (2013). Theoretical analysis of piezoelectric energy harvesting from traffic induced deformation of pavements. Smart Materials and Structures, 22(9), 095024.

133. Xiao, J., Sun, S., Zhang, X., Zhang, D., Wei, K., & Wang, Y. (2021). Macro and meso dynamic response of granular materials in ballastless track subgrade for high-speed railway. International Journal of Transportation Science and Technology, 10(4), 313-328.

134. Xie, X. D., Wang, Q., & Wang, S. J. (2015). Energy harvesting from high-rise buildings by a piezoelectric harvester device. Energy. 93, 1345-1352.

135. Xu, B., Zhang, T., Song, G., & Gu, H. (2013). Active interface debonding detection of a concrete-filled steel tube with piezoelectric technologies using wavelet packet analysis. Mechanical Systems and Signal Processing, 36(1), 7-17.

136. Xu, D., Banerjee, S., Wang, Y., Huang, S., & Cheng, X. (2015). Temperature and loading effects of embedded smart piezoelectric sensor for health monitoring of concrete structures. Construction and Building Materials, 76, 187-193.

137. Xu, X., Cao, D., Yang, H., & He, M. (2018). Application of piezoelectric transducer in energy harvesting in pavement. International Journal of Pavement Research and Technology, 11(4), 388-395.

138. Yang H., Zhao Q., Guo X., Zhang W., Liu P., Wang L. (2020). Numerical Analysis of Signal Response Characteristic of Piezoelectric Energy Harvesters Embedded in Pavement. Materials. 13(12), 2770.

139. Yang, J. W., Zhu, H. P., Yu, J., & Wang, D. S. (2013). Experimental study on monitoring steel beam local corrosion based on EMI technique. Paper presented at the Applied Mechanics and Materials.

140. Yang, Y., Shen, Q., Jin, J., Wang, Y., Qian, W., Yuan, D. (2014). Rotational piezoelectric wind energy harvesting using impact-induced resonance. Applied Physics Letter 105(5), 053901.

141. Yao, J. T. (1972). Concept of structural control. Journal of the Structural Division, 98(7), 1567-1574.

142. Yu, Z., Zhou, A., & Lau, D. (2016). Mesoscopic packing of disk-like building blocks in calcium silicate hydrate. Scientific Reports, 6(1), 1-8.

143. Zahedi, A. (2006). Solar photovoltaic (PV) energy; latest developments in the building integrated and hybrid PV systems. Renewable Energy, 31(5), 711-718.

144. Zhang, G., Gao, S., & Liu, H. (2016). A utility piezoelectric energy harvester with low frequency and high-output voltage: Theoretical model, experimental verification and energy storage. AIP Advances 6(9), 095208.

145. Zhang, Y., Cai, C., & Zhang, W. (2014). Experimental study of a multi-impact energy harvester under low frequency excitations. Smart Materials and Structures, 23(5), 055002.

146. Zhang, Y., Cai, S. C., & Deng, L. (2014). Piezoelectric-based energy harvesting in bridge systems. Journal of Intelligent Material Systems and Structures, 25(12), 1414-1428.

147. Zhang, Z., Tang, L., & Xiang, H. (2019). Piezoelectric energy harvesting from bridge vibrations using different models for moving vehicles. Journal of Aerospace Engineering, 32(2), 04018141.

148. Zhang, Z., Xiang, H., & Shi, Z. (2016). Modeling on piezoelectric energy harvesting from pavements under traffic loads. Journal of Intelligent Material Systems and Structures, 27(4), 567-578.

149. Zhang, Z., Xiang, H., Shi, Z., & Zhan, J. (2018). Experimental investigation on piezoelectric energy harvesting from vehicle-bridge coupling vibration. Energy Conversion and Management, 163, 169-179.

150. Zhao, H., Ling, J., & Yu, J. (2012). A comparative analysis of piezoelectric transducers for harvesting energy from asphalt pavement. Journal of the Ceramic Society of Japan, 120(1404), 317-323.

151. Zhao, H., Yu, J., & Ling, J. (2010). Finite element analysis of Cymbal piezoelectric transducers for harvesting energy from asphalt pavement. Journal of the Ceramic Society of Japan, 118(1382), 909-915.

152. Zhao, J., & Wang, H. (2020). Mechanistic modeling and economic analysis of piezoelectric energy harvesting potential in airport pavements. Transportation Research Record, 2674(11), 64-75.

153. Zhao, S., & Erturk, A. (2014). Deterministic and band-limited stochastic energy harvesting from uniaxial excitation of a multilayer piezoelectric stack. Sensors and Actuators A: Physical, 214, 58-65.

154. Zimmerman, A. T., Shiraishi, M., Swartz, R. A., & Lynch, J. P. (2008). Automated modal parameter estimation by parallel processing within wireless monitoring systems. Journal of Infrastructure Systems, 14(1), 102-113.

155. Zorlu, Ö., Topal, E. T., Külah, H. (2010). A vibration-based electromagnetic energy harvester using mechanical frequency up-conversion method. IEEE Sensors Journal 11(2), 481-488.